STELLINGEN

behorende bij het proefschrift

NUMERICAL ANALYSIS OF SOIL-STRUCURE INTERACTION

H. van Langen, Delft, 1991

1. De door Walsh gepubliceerde formule voor de elasticiteitsmodulus van gesteente met initiële microscheuren, E_{eff}, te weten

$$E_{eff} = E \,/\, (1 + \frac{4\pi}{15}\, \alpha c^3 v^{-1})$$

met E = modulus voor intact gesteente, 2c = gemiddelde scheurlengte, v^{-1} = scheurdichtheid, $\alpha = 5$ voor open scheuren en $\alpha = (2+3\mu^2+2\mu^4)/(1+\mu^2)^{1.5} - 2\mu$ voor schuivende scheuren met wrijvingscoëfficiënt μ, is fout. Een gecorrigeerde afleiding levert voor open scheuren $\alpha = 10$ en voor schuivende scheuren $\alpha = 2 - (2\mu^5+5\mu^3+3\mu)/(1+\mu^2)^{2.5}$.

J.B. Walsh, 'The effect of cracks on the uniaxial elastic compression of rocks', *J. Geophys. Res.*, **70**, (2), 399-411 (1965)

2. De eindige-elementenmethode verdient een bredere acceptatie onder geotechnisch ingenieurs, aangezien de resultaten, zelfs in die gevallen waar grondgegevens beperkt zijn, inzicht verschaffen in het gedrag van grond.

3. Splitsing van de materiële afgeleide van de Cauchy spanningstensor in een constitutief en een convectief deel, leidt tot een eenvoudige interpretatie van enkele objectieve spanningstensoren.

Dit proefschrift, hoofdstuk 1.

4. Meten is weten, maar simuleren is leren.

5. De in een cap-plasticiteitsmodel gebruikte elastische dwarscontractiecoëfficiënt, ν_e, is groter dan de initiële coëfficiënt, ν_i, welke het model voorspelt bij de simulatie van een gedraineerde triaxiaalproef op een normaal geconsolideerd monster. Kiest men $\nu_e = 0$ dan volgt dus $\nu_i < 0$, hetgeen niet wenselijk is.

6. De kleur van een creditcard dreigt een indicator voor maatschappelijke status te worden.

7. Het stelsel consistentievergelijkingen voor de triaxiaalribben in singuliere vloeioppervlakken kan in het geval van isotroop materiaalgedrag ontkoppeld worden, waardoor het oplossen van deze vergelijkingen eenvoudiger wordt.

Dit proefschrift, hoofdstuk 5.

8. De opvatting dat een eindige-elementenprogramma met interactieve invoer een verhoogde kans op verkeerde antwoorden geeft, is onjuist. Een dergelijke optie ontlast immers de gebruiker, waardoor deze zijn aandacht meer kan richten op de fysische interpretatie van in- en uitvoergegevens.

9. Voor de nauwkeurige analyse van constructies op slappe grond is het noodzakelijk effecten van grote deformaties in de beschouwing te betrekken.

10. De huiskat is nummer één op het gebied van vandalisme; de mens is een goede tweede.

11. De levensmiddelentechnologie heeft ons leven verrijkt met vetarme frites-saus en suikervrije kauwgom. Het wachten is nu nog op alcoholvrije jenever.

Numerical Analysis of Soil-Structure Interaction

NUMERICAL ANALYSIS OF SOIL-STRUCTURE INTERACTION

PROEFSCHRIFT

ter verkrijging van de graad van doctor aan
de Technische Universiteit Delft, op gezag van
de Rector Magnificus, prof. drs. P.A. Schenck,
in het openbaar te verdedigen ten overstaan van een
commissie aangewezen door het College van Dekanen
op dinsdag 12 maart 1991 te 16.00 uur

door

Harry van Langen

geboren te Schiedam
civiel ingenieur

Dit proefschrift is goedgekeurd door de promotor: prof.dr.ir. A. Verruijt

Toegevoegd promotor: dr.ir. P.A. Vermeer

To Miranda

ACKNOWLEDGEMENTS

The research for this thesis was carried out at the Geotechnical Laboratory of the Faculty of Civil Engineering of Delft University of Technology, under the supervision of Dr. P.A. Vermeer. All finite element procedures described in this study were implemented in the PLAXIS finite element code.

I gratefully acknowledge the continued support of my colleagues in the PLAXIS development team. I am also much indebted to Mr. J. van Leeuwen for preparing the figures in this report and to Mrs. J. Holmer for the graphic design of the cover.

H. van Langen

CONTENTS

1. INTRODUCTION

The finite element analysis of deformation and failure of soil bodies has been the subject of many studies in the past and much progress has indeed been made since the first publications appeared. However, the application of the method in day to day engineering practice has advanced at a much slower rate. This is partly due to the fact that considerable skill and experience is needed to control the non-linear finite element computation, especially when highly frictional soil is being considered. In addition, finite element results can be rather disappointing in the sense that they may display non-physical phenomena like stress oscillations and spurious deformations. Instead of concentrating on solving these basic problems, most finite element research is aimed at spanning the frontiers of application. As a result, the gap between research and engineering practice tends to widen instead of narrow. To prevent this from happening more attention needs to be paid to the design of robust finite element procedures. The finite element method deserves wider acceptance as it can help provide a clearer understanding of soil behaviour, even in cases where soil data are limited, and can thus assist in making decisions on safe and economic design.

The aim of this study is to improve some existing procedures for the finite element analysis of soil deformation and collapse. Special attention is paid to problems of soil-structure interaction. Here emphasis is put on the behaviour of soil rather than on that of structures. This seems to be justifiable if static interaction of stiff structures and soft soil is considered. In such a case non-linear response will exclusively stem from soil deformation. In addition, the quality of results depends to a high extent on the proper modelling of soil flow along structures and not on the modelling of the structure itself. An exception is made when geotextile reinforcement is considered. In that case the structural element, i.e. the geotextile, is highly flexible.

The contents of this thesis are arranged as follows. Chapter 2 discusses the equation of continued equilibrium, which serves as a starting point for the finite element formulation of large deformation elastoplasticity. Special

attention is devoted to the interpretation of some objective stress rate tensors. All constitutive models in this thesis are based on the theory of plasticity. For this reason, chapter 2 also gives the structure of elastoplastic constitutive models.

In Chapter 3 the solution of non-linear finite element equations is addressed. The choice of suitable step sizes in the incremental-iterative procedure proves to be difficult, especially when highly frictional soil is considered. As a result, it is difficult to obtain the complete load-displacement path of a soil body up to and beyond limit points. To correct this situation, an automatic load stepping procedure is developed. Its application is demonstrated by considering several problems of soil-structure interaction. In addition, a discussion is given of error estimates and convergence criteria. It is pointed out that traditional criteria, like the out-of-balance error, may yield inaccurate results.

The application of interface elements to problems of soil-structure interaction is discussed in Chapter 4. Interface elements are applied at the contact between soil and structures, where the soil is intensely distorted. After a straightforward formulation of an interface element, its numerical spatial integration is addressed. The quality of computed contact pressures is very much dependent on the type of integration scheme applied. This phenomenon is discussed in depth. After this, a novel use of interface elements is presented, namely the treatment of singular plasticity points. Such points are encountered in most problems of soil-structure interaction. Some example problems are solved to demonstrate the influence of singular plasticity points.

Chapter 5 discusses soil deformation in the pre-failure range. The well-known Mohr-Coulomb plasticity model is enhanced by introducing a yield cap. This model is special in the sense that it is able to simulate realistic states of stress in one-dimensional compression. In contrast to existing yield caps, we apply the Mohr-Coulomb concept of an angular yield surface and not the Drucker-Prager concept of a circular yield surface. This discussion also covers the treatment of ridges in singular yield surfaces. It is shown that the classical treatment can be simplified by exploiting symmetries in the yield surfaces. A large scale model test on a circular footing is simulated to demonstrate the model's capability.

Finally, Chapter 6 touches on large deformation effects in the analysis of soil deformation. After validation of the updated Lagrangian technique, as developed in Chapter 2, this technique is used in the analysis of a circular footing test. Experimental results appear to fit well. Differences between small and large deformation computations become apparent.

Another application is the analysis of reinforced soils. For this purpose a special large deformation membrane element is developed. An important application can be found in the analysis of reinforced roads and embankments. In this study we consider the test embankments in Almere, the Netherlands. Both a reinforced and a non-reinforced embankment are analyzed.

In this study only rectangular Cartesian coordinates are considered. Index notation is employed in the formulation of basic equations for the problem of large elastoplastic deformation, whereas vector notation is used in the discussion of finite element equations. One exception to this rule is found in Chapter 2, where the formal derivation of finite element equations is performed using index notation. The summation convention applies to repeated lower indices only in chapter 2. In imitation of Fung[6], a comma preceding a lower index implies differentiation with respect to a spatial coordinate and a superimposed dot denotes the material rate of change. A single underscore is used to identify a vector, whilst a double underscore is used for matrices. This report does not contain a list of symbols. Instead, all symbols are defined when they first appear.

2. FORMULATION OF BASIC EQUATIONS

In this chapter the basic equations for the problem of large elastoplastic deformation and its finite element discretization will be derived. The equation of continued equilibrium prescribes the way in which stress and strain change without violating equilibrium. Secondly a formal framework is developed for large deformation elastoplastic constitutive relations. All specialized models in subsequent chapters should adhere to this. Finally the finite element discretization of the governing equations is discussed.

2.1 Virtual work equation

Let us consider the equilibrium of two bodies sharing a common contact surface as indicated in Figure (2.1). The bodies are labelled with index a and index b respectively. Equilibrium requires the residual r_i to vanish for all material points in the interior of the bodies[1,2,3]

$$r_i^a \equiv \sigma_{ji,j}^a + \gamma_i^a = 0 \qquad ; \qquad r_i^b \equiv \sigma_{ji,j}^b + \gamma_i^b = 0 \tag{2.1}$$

where σ_{ji} is the Cauchy stress tensor and γ_i is a body force. Note that the current configuration is taken as a reference configuration. The virtual work equation can be obtained by restating equation (2.1) in its weak form[4]

$$\delta W \equiv \int_{V_a} r_i^a \delta u_i \, dV + \int_{V_b} r_i^b \delta u_i \, dV = 0 \tag{2.2}$$

where δu_i is a small displacement variation.

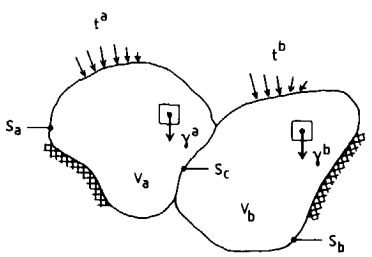

Figure 2.1. Equilibrium of two contacting bodies.

Inserting definitions (2.1), applying Gauss's divergence theorem and Cauchy's formula, $\sigma_{ji} n_j = t_i$, transforms equation (2.2) into the well-known form[5,6]

$$-\int_V \sigma_{ji}\delta u_{i,j}dV + \int_V \gamma_i \delta u_i dV + \int_{Sa} t_i^a \delta u_i dS + \int_{Sb} t_i^b \delta u_i dS = 0 \qquad (2.3)$$

Here the volume V extends over both bodies. The surfaces of the respective bodies are denoted by S_a and S_b and t_i is the associated traction. If we split the surface into an external part, S_e, and a common contact, S_c, the surface terms in equation (2.3), δW_s, can be written as

$$\delta W_s = \int_{Se} t_i \delta u_i dS + \int_{Sca} t_i^a \delta u_i dS + \int_{Scb} t_i^b \delta u_i dS \qquad (2.4)$$

Newton's principle of action and reaction, namely

$$t_i^a = -t_i^b = \tau_i \qquad (2.5)$$

yields after insertion in identity (2.4)

$$\delta W_s = \int_{Se} t_i \delta u_i dS + \int_{Sca} \tau_i \delta u_i dS - \int_{Scb} \tau_i \delta u_i dS \qquad (2.6)$$

The virtual work equation in its final form reads

$$-\delta W_\sigma - \delta W_c + \delta W_\gamma + \delta W_t = 0 \qquad (2.7)$$

where

$$\delta W_\sigma \equiv \int_V \sigma_{ji}\delta u_{i,j}dV$$

$$\delta W_c \equiv \int_{Scb} \tau_i \delta u_i dS - \int_{Sca} \tau_i \delta u_i dS$$

$$\delta W_\gamma \equiv \int_V \gamma_i \delta u_i dV$$

$$\delta W_t \equiv \int_{Se} t_i \delta u_i dS$$

2.2 Equation of continued equilibrium

Changes of stress and deformation should be such that equation (2.7) is valid at all times. This condition is met when

$$(\delta W)^{\cdot} = 0 \tag{2.8}$$

in which a dot denotes the material rate of change[1,2]

$$\dot{F} \equiv \partial F/\partial t + \dot{u}_k F_{,k} \tag{2.9}$$

Differentiation and rearrangement of this formula yields the following useful identity

$$(F_{,j})^{\cdot} = \dot{F}_{,j} - \dot{u}_{k,j} F_{,k} \tag{2.10}$$

which will be needed in the remainder of this chapter. The material rates of change of volume and surface integrals are given by

$$\left[\int_V F \, dV \right]^{\cdot} = \int_V \left[\dot{F} + F \, \dot{\varepsilon}_{kk} \right] dV \tag{2.11}$$

$$\left[\int_S F \, dS \right]^{\cdot} = \int_S \left[\dot{F} + F \, (\dot{\varepsilon}_{kk} - n_k n_l \dot{\varepsilon}_{kl}) \right] dS \tag{2.12}$$

in which $\dot{\varepsilon}_{kl}$ represents the strain rate tensor and n_k is the normal to the surface element dS. Detailed derivations can be found in the literature[1,2].

Condition (2.8) can now be elaborated with the aid of the above formulae. For the first term we find

$$\delta \dot{W}_{\sigma} = \int_V (\dot{\sigma}_{ji} \delta u_{i,j} + \sigma_{ji} (\delta u_{i,j})^{\cdot} + \sigma_{ji} \delta u_{i,j} \dot{u}_{k,k}) \, dV \tag{2.13}$$

With the aid of equation (2.10) the material rate of change of the virtual displacement gradient can be split into two parts

$$(\delta u_{i,j})^{\cdot} = \delta \dot{u}_{i,j} - \dot{u}_{k,j} \delta u_{i,k} = -\dot{u}_{k,j} \delta u_{i,k} \tag{2.14}$$

the first of which is zero, for δu_i is kept constant with regard to the moving material during operation (2.8).

Substitution of this result in equation (2.13) yields

$$\delta\dot{W}_{\sigma} = \int_V (\dot{\sigma}_{ji} - \sigma_{ki}\dot{u}_{j,k} + \sigma_{ji}\dot{u}_{k,k})\delta u_{i,j}\,dV \tag{2.15}$$

The term in brackets in this equation can be identified as the material rate of change of the first Piola-Kirchoff stress tensor[1,2]

$$\dot{\Sigma}_{ji} = \dot{\sigma}_{ji} - \sigma_{ki}\dot{u}_{j,k} + \sigma_{ji}\dot{u}_{k,k} \tag{2.16}$$

Consequently, equation (2.15) can be simplified to the expression

$$\delta\dot{W}_{\sigma} = \int_V \dot{\Sigma}_{ji}\delta u_{i,j}\,dV \tag{2.17}$$

Upon differentiation the interface term δW_c in the virtual work equation yields

$$\delta\dot{W}_c = \int_{Sc} [\dot{\tau}_i \delta\Delta u_i + \tau_i (J_b \delta u_i - J_a \delta u_i)]\,dS \tag{2.18}$$

Here J determines the stretch of a surface element $(dS)^{\cdot} = JdS$ and $\delta\Delta u_i$ is the virtual relative displacement $\delta\Delta u_i = \delta u_i^b - \delta u_i^a$

The material rates of change of the load terms in equation (2.7) follow directly from differentiation according to equations (2.11) and (2.12)

$$\delta\dot{W}_{\gamma} = \int_V (\dot{\gamma}_i + \gamma_i \dot{u}_{k,k})\,\delta u_i\,dV \tag{2.19}$$

$$\delta\dot{W}_t = \int_S (\dot{t}_i + t_i J)\,\delta u_i\,dS \tag{2.20}$$

In this study, only dead loading will be considered. Consequently, the load γ_i is a load per unit of mass

$$\gamma_i = \gamma\,\rho\,g_i \quad ; \quad \dot{\gamma}_i = \dot{\gamma}\,\rho\,g_i + \gamma\,\dot{\rho}\,g_i \tag{2.21}$$

Here γ is a load intensity and ρ is the density of the material. From continuity it follows that

$$\dot{\rho} = -\dot{u}_{k,k}\rho \tag{2.22}$$

Substitution of this result in equation (2.19) yields for dead loading

$$\delta\dot{W}_{\gamma} = \int_V \dot{\gamma}\ \rho\ g_i \delta u_i dV \tag{2.23}$$

We will also assume that the traction is derived from a co-stretching load, which implies that

$$\delta\dot{W}_{t} = \int_S \dot{t}\rho_s n_i \delta u_i dS \tag{2.24}$$

Here, ρ_s is defined by the expression $\dot{\rho}_s = -J\ \rho_s$, t is a load intensity and n_i determines the direction of the traction.

The condition for continued equilibrium is now found by inserting the material rates of change (2.15-2.24) into equation (2.8)

$$-\int_V \dot{\Sigma}_{ji} \delta u_{i,j} dV - \int_S I_c dS + \int_V \dot{\gamma}\rho g_i \delta u_i dV + \int_S \dot{t}\rho_s n_i \delta u_i dS = 0 \tag{2.25}$$

where

$$I_c = \dot{\tau}_i \delta\Delta u_i + \tau_i (J_b \delta u_i - J_a \delta u_i)$$

In reference (7), Van der Lugt arrives at a slightly different expression for the interface term I_c, namely

$$I_c = \dot{\tau}_i \delta\Delta u_i + \tau_i J_r \delta\Delta u_i$$

where $J_r = \frac{1}{2}(J_a + J_b)$ is the stretch of a common reference surface. Note that this expression coincides with definition (2.18) when both contacting surfaces deform at the same rate, i.e. $J_a = J_b$. However, in general, expression (2.25) is more accurate as it does not disregard differences in stretch. Boulon[8] enhances the equation of continued equilibrium by taking possible separation of the contacting surfaces into account.

To complete relation (2.25), increments of stress should be related to increments of strain by means of a constitutive equation.

2.3 Objective stress rate tensors

Constitutive equations relate measures of strain to objective measures of stress. Such stress measures ensure for instance that rigid body motions do not influence the stress state of the material. Several definitions of stress rate can be found in the literature, references (1,2,6,9,10). Three of those definitions will be discussed here, namely the ones by Jaumann, Hill and Truesdell respectively.

To arrive at a definition for an objective stress rate we should realize that the material rate of change of Cauchy stress is caused not only by elastic deformation, but also by convection of the Cauchy stress which was already present before the change took place

$$\dot{\sigma}_{ij} = \overset{\circ}{\sigma}_{ij} + \overset{\vee}{\sigma}_{ij} \tag{2.26}$$

The first term, $\overset{\circ}{\sigma}_{ij}$, will be called the constitutive rate of Cauchy stress and the second term, $\overset{\vee}{\sigma}_{ij}$, the convective rate of Cauchy stress. These names are not usual in the literature, but help provide a clearer understanding of the present line of reasoning. The definitions of objective stress rate now follow from the interpretation of the convective stress rate.

Suppose a material element is loaded by the forces df_i^0 on a surface element dA_i^0, Figure (2.2). The corresponding Cauchy stress σ_{ij} follows from Cauchy's formula[1,2]

$$\sigma_{ij} dA_i^0 = df_j^0 \tag{2.27}$$

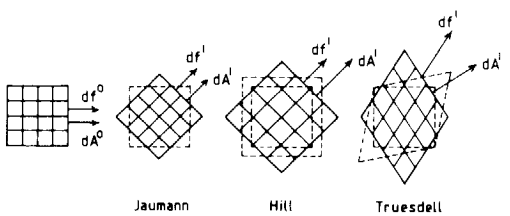

Figure 2.2. Interpretation of the convective rate of Cauchy stress.

During a deformation, the forces on a surface element follow the moving body. The force keeps the direction of the line element with which it was aligned in the configuration at $t=t_0$. The surface element rotates and stretches. To obtain the convective change of Cauchy stress, the components of both the force and the surface vectors in the current configuration at $t=t_1$ should be expressed relative to a fixed frame of reference. In appendix A it is derived that these components are given by

$$\begin{aligned} df_i^1 &= C_{ij}\, df_j^0 = C_{ij}\, \sigma_{kj}\, dA_k^0 \\ dA_i^1 &= \rho_0/\rho_1\; C_{ji}^{-1}\, dA_j^0 \end{aligned} \tag{2.28}$$

Here C_{ij} is the deformation gradient and ρ_0/ρ_1 is the ratio of subsequent densities. The convective change of Cauchy stress relates the deformed surface to the force on it in the following way

$$(\sigma_{ij} + \overset{\vee}{\sigma}_{ij}\, dt)\; dA_i^1 = df_j^1 \tag{2.29}$$

This stress can be related to the stress in the configuration at $t=t_0$ by combining equations (2.28) and (2.29)

$$(\sigma_{ij} + \overset{\vee}{\sigma}_{ij}\, dt) = \rho_1/\rho_0\; C_{ik} C_{jl}\; \sigma_{kl} \tag{2.30}$$

In appendix A it is shown that matrix C_{ij} and the ratio of subsequent densities can be related to the deformation of the material point being considered

$$\rho_1/\rho_0 = (1 - \dot{\varepsilon}_{kk}\, dt) \qquad ; \qquad C_{ij} = (\delta_{ij} + (\dot{\varepsilon}_{ij} - \Omega_{ij})\, dt) \tag{2.31}$$

where the strain rate tensor $\dot{\varepsilon}_{ij}$ and the spin tensor Ω_{ij} are defined by[6]

$$\begin{aligned} \dot{\varepsilon}_{ij} &= \tfrac{1}{2}\,(\dot{u}_{i,j} + \dot{u}_{j,i}) \\ \Omega_{ij} &= \tfrac{1}{2}\,(\dot{u}_{j,i} - \dot{u}_{i,j}) \end{aligned} \tag{2.32}$$

Jaumann rate of stress :

The Jaumann definition of stress rate considers only convective changes due to rotation. Consequently, terms due to deformation should be deleted from

expression (2.31)

$$\rho_1/\rho_0 = 1 \qquad ; \qquad C_{ij} = (\delta_{ij} - \Omega_{ij}dt) \tag{2.33}$$

The convective rate of stress follows from the combination of this and equation (2.30).

$$\overset{\smile}{\sigma}{}^{J}_{ij} = \sigma_{ik}\Omega_{kj} + \sigma_{jk}\Omega_{ki} \tag{2.34}$$

The Jaumann rate of Cauchy stress is defined as the corresponding constitutive stress rate which is found by rearranging definition (2.26)

$$\overset{\circ}{\sigma}{}^{J}_{ij} = \dot{\sigma}_{ij} - \overset{\smile}{\sigma}{}^{J}_{ij} \tag{2.35}$$

Substituting the convective change of stress yields the well-known definition of the Jaumann stress rate[1,6,9]

$$\overset{\circ}{\sigma}{}^{J}_{ij} = \dot{\sigma}_{ij} - \sigma_{ik}\Omega_{kj} - \sigma_{jk}\Omega_{ki} \tag{2.36}$$

Hill rate of stress:

When dilation is taken into account, but directional changes of the force and surface vectors are based on rigid rotation only, it is found that

$$\rho_1/\rho_0 = (1 - \dot{\varepsilon}_{kk}dt) \quad ; \quad C_{ij} = (\delta_{ij} - \Omega_{ij}dt) \tag{2.37}$$

From these expressions and equation (2.30) the convective change of Cauchy stress is obtained

$$\overset{\smile}{\sigma}{}^{H}_{ij} = -\dot{\varepsilon}_{kk}\sigma_{ij} + \sigma_{ik}\Omega_{kj} + \sigma_{jk}\Omega_{ki} = -\dot{\varepsilon}_{kk}\sigma_{ij} + \overset{\smile}{\sigma}{}^{J}_{ij} \tag{2.38}$$

which results in the following constitutive stress rate

$$\overset{\circ}{\sigma}{}^{H}_{ij} = \overset{\circ}{\sigma}{}^{J}_{ij} + \dot{\varepsilon}_{kk}\sigma_{ij} \tag{2.39}$$

This definition will conveniently be called the Hill rate of stress. Other names encountered in the literature are co-rotational rate of Kirchoff stress[10] and Biezeno-Hencky stress rate[9].

Truesdell rate of stress:

Finally, all deformation effects are taken into account in the Truesdell[1,9] stress rate definition

$$\rho_1/\rho_0 = (1 - \dot{\varepsilon}_{kk}dt) \quad ; \quad C_{ij} = (\delta_{ij} + (\dot{\varepsilon}_{ij} - \Omega_{ij})dt) \tag{2.40}$$

which yields the following convective change of Cauchy stress

$$\begin{aligned} \check{\sigma}^T_{ij} &= -\dot{\varepsilon}_{kk}\sigma_{ij} + \sigma_{ik}\Omega_{kj} + \sigma_{jk}\Omega_{ki} + \sigma_{ik}\dot{\varepsilon}_{kj} + \sigma_{jk}\dot{\varepsilon}_{ki} \\ &= -\dot{\varepsilon}_{kk}\sigma_{ij} + \sigma_{ik}\dot{\varepsilon}_{kj} + \sigma_{jk}\dot{\varepsilon}_{ki} + \check{\sigma}^J_{ij} \end{aligned} \tag{2.41}$$

and the Truesdell definition of the constitutive stress rate

$$\overset{\circ}{\sigma}^T_{ij} = \overset{\circ}{\sigma}^J_{ij} + \dot{\varepsilon}_{kk}\sigma_{ij} - \sigma_{ik}\dot{\varepsilon}_{kj} - \sigma_{jk}\dot{\varepsilon}_{ki} \tag{2.42}$$

The definition by Truesdell will not be used here because it is very involved and displays a non-physical characteristic when used in Hooke's law for increments of stress and strain. In addition, Hill's definition has the advantage that it symmetrizes the finite element equations[10,11,7]. Therefore, the constitutive equations will be developed on the basis of the Hill rate of Cauchy stress.

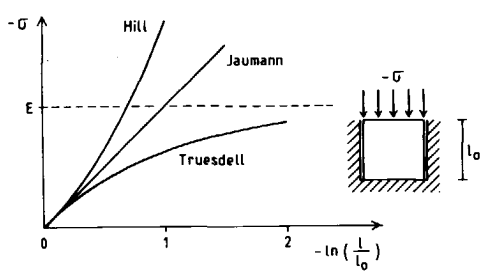

Figure 2.3 Result of oedometer test for three stress rate definitions

Figure (2.3) shows the result for the simulation of a compression test. The curve which follows from Truesdell's definition of stress rate is described by

the expression

$$\sigma = E\ (e^{\varepsilon} - 1) \tag{2.43}$$

Here, E is Young's modulus, whilst ε is the logarithmic strain which follows from integration of the strain rate. Note that Poisson's ratio was chosen as equal to zero. It appears that the stiffness decreases when the density increases, whereas the opposite would be expected from a physical point of view. However, the curve based on Hill's stress rate definition agrees well with the above expectation. Now the stress-strain relation is given by

$$\sigma = E\ (1 - e^{-\varepsilon}) \tag{2.44}$$

Hence, Hooke's law for increments of stress and strain can best be based on Hill's rate of stress. The performance of a model based on Truesdell's definition can only be improved by adopting an incremental non-linear elastic law.

2.4 Objective rates of surface traction

The formulation of a constitutive relation for the interface at the contact between bodies requires the definition of an objective measure for the traction. This measure can be developed along the same lines as the objective stress rate tensor. Like in equation (2.26), we can distinguish between a constitutive change, $\overset{\circ}{t}_i$, and a convective change, $\overset{\vee}{t}_i$, of the surface traction

$$\dot{t}_i = \overset{\circ}{t}_i + \overset{\vee}{t}_i \tag{2.45}$$

By definition, the traction t_i relates the surface element to the force on it

$$t_i dA^0 = df_i^0 \tag{2.46}$$

During deformation, the components of the force change according to equation (2.28) when related to a fixed frame of reference. In addition, the surface element stretches

$$dA^1 = (1 + Jdt)\ dA^0 \tag{2.47}$$

Here J denotes the surface stretch. The convective change of the traction relates the surface to the force on it, namely

$$(t_i + \check{t}_i dt)\ dA^1 = df_i^1 \tag{2.48}$$

Substitution from equation (2.28), (2.46) and (2.47) yields after some rearrangement

$$\check{t}_i = t_k \Omega^r_{ki} - t_i J^r + t_k \dot{\varepsilon}^r_{ki} \tag{2.49}$$

Here a superscript r denotes that the deformation should be derived from the movement of the contact surface.

When only rigid rotation is considered in the development of equation (2.49), the Jaumann rate of traction is obtained

Jaumann: $$\overset{\circ}{t}{}^J_i = \dot{t}_i - t_k \Omega^r_{ki} \tag{2.50}$$

According to Hill directional changes are derived from rigid rotation. In addition, the stretch of the surface is taken into account

Hill: $$\overset{\circ}{t}{}^H_i = \overset{\circ}{t}{}^J_i + t_i J^r \tag{2.51}$$

Finally, all deformation effects are taken into account in the Truesdell definition of an objective traction rate

Truesdell: $$\overset{\circ}{t}{}^T_i = \overset{\circ}{t}{}^J_i + t_i J^r - t_k \dot{\varepsilon}^r_{ki} \tag{2.52}$$

For the evaluation of equation (2.49), the deformation of the contact surface is needed. As observed earlier, however, both contacting surfaces may deform independently. Consequently, we need a reference plane from which the deformation is derived. This plane can be defined by its deformation

$$\dot{u}^r_i = \frac{1}{2} (\dot{u}^a_i + \dot{u}^b_i) \tag{2.53}$$

Note that when both planes deform at the same rate, the correct deformation is obtained. With this definition, the stretch and the spin tensor in equation (2.49) can be written as

$$J^r = \frac{1}{2} (J^a + J^b) \quad ; \quad \Omega^r_{ij} = \frac{1}{2} (\Omega^a_{ij} + \Omega^b_{ij}) \tag{2.54}$$

2.5 Structure of elastoplastic constitutive equations

A suitable measure of strain is the strain rate tensor $\dot{\varepsilon}_{ij}$, which is the symmetric part of the velocity gradient tensor

$$\dot{\varepsilon}_{ij} = \frac{1}{2}(\dot{u}_{i,j} + \dot{u}_{j,i}) \tag{2.55}$$

All constitutive relations in this study will be based on the theory of plasticity[3,5]. Consequently, the strain rate tensor can be split into an elastic part and a plastic part

$$\dot{\varepsilon}_{ij} = \dot{\varepsilon}^{e}_{ij} + \dot{\varepsilon}^{p}_{ij} \tag{2.56}$$

of which the first part induces changes of objective stress. Here the singular surface plasticity theory of Koiter[5] in its generalization by Mandel[12] is followed. In this theory, the plastic strain rate is split into separate contributions

$$\dot{\varepsilon}^{p}_{ij} = \sum_{k} \dot{\varepsilon}^{pk}_{ij} \tag{2.57}$$

A strain rate component $\dot{\varepsilon}^{pk}_{ij}$ adheres to the conditions

$$\begin{aligned} &\dot{\varepsilon}^{pk}_{ij} = 0 \text{ when } f_k < 0 \text{ or when } f_k = 0 \text{ and } \dot{f}_k < 0 \\ &\dot{\varepsilon}^{pk}_{ij} \neq 0 \text{ when } f_k = 0 \text{ and } \dot{f}_k = 0 \text{ with } \dot{\lambda}_k > 0 \end{aligned} \tag{2.58}$$

where f_k is a yield function and λ_k is a positive multiplier which relates the strain rate to a plastic potential function $g_k = g_k(\sigma_{ij})$

$$\dot{\varepsilon}^{p}_{ij} = \dot{\lambda}_k \frac{\partial g_k}{\partial \sigma_{ij}} \tag{2.59}$$

Mandel adopts the concept of strain hardening by assuming f_k to be a function of the stress state and of the multipliers λ_m

$$f_k = f_k(\sigma_{ij}, \lambda_m) \tag{2.60}$$

As a result, the multipliers can be solved from the consistency conditions

$$\dot{f}_k = \frac{\partial f_k}{\partial \sigma_{ij}} \overset{\circ}{\sigma}_{ij} + \frac{\partial f_k}{\partial \lambda_m} \dot{\lambda}_m = 0 \tag{2.61}$$

For isotropic response, the relation between the objective stress rate and the elastic part of the strain rate tensor becomes[1,2,3,5,6]

$$\overset{\circ}{\sigma}_{ij} = D^{e}_{ijkl}\,\dot{\varepsilon}^{e}_{kl} \tag{2.62}$$

where

$$D^{e}_{ijkl} = \lambda\,\delta_{ij}\delta_{kl} + \mu\,(\delta_{ik}\delta_{jl} + \delta_{il}\delta_{jk}) \tag{2.63}$$

The parameters λ and μ are Lamé's constants and δ_{ij} represents the Kronecker delta. Some researchers[11] argue that this definition of elastic response is only valid for small elastic deformation. For large elastic deformation, a closed cycle of load application and removal yields energy dissipation in some cases. However, this restriction is not very severe in the case of soil mechanics, where large deformation is mainly caused by plastic strain.

Combination of equations (2.56) and (2.59-2.62) yields after some elaboration

$$B_{km}\,\dot{\lambda}_{m} = \frac{\partial f_{k}}{\partial \sigma_{ij}}\; D^{e}_{ijpq}\;\dot{\varepsilon}_{pq} \tag{2.64}$$

where

$$B_{km} = \frac{\partial f_{k}}{\partial \sigma_{ij}}\; D^{e}_{ijpq}\;\frac{\partial g_{m}}{\partial \sigma_{pq}} - \frac{\partial f_{k}}{\partial \lambda_{m}} \tag{2.65}$$

Equation (2.64) represents a system of linear equations for the unknown multipliers $\dot{\lambda}_{m}$, which upon solution yields

$$\dot{\lambda}_{m} = B^{-1}_{mk}\;\frac{\partial f_{k}}{\partial \sigma_{ij}}\; D^{e}_{ijpq}\;\dot{\varepsilon}_{pq} \tag{2.66}$$

where by definition

$$B^{-1}_{ij}\,B_{jk} = \delta_{ik} \tag{2.67}$$

Combination of equations (2.56), (2.59), (2.62) and (2.66) leads to the formal expression for the constitutive relation,

$$\overset{\circ}{\sigma}_{ij} = D^{ep}_{ijkl}\,\dot{\varepsilon}_{kl} \tag{2.68}$$

where

$$D^{ep}_{ijkl} = D^{e}_{ijkl} - D^{e}_{ijrs}\;\frac{\partial g_{m}}{\partial \sigma_{rs}}\;B^{-1}_{mn}\;\frac{\partial f_{n}}{\partial \sigma_{pq}}\;D^{e}_{pqkl} \tag{2.69}$$

Equation (2.68) serves as a basis for more detailed descriptions of material behaviour.

The constitutive relation for the contact between bodies will be developed in complete analogy to the relation for the continuum. In this case, the relative velocity of the contacting surfaces can serve as a measure of deformation[7]

$$\Delta\dot{u}_i = \dot{u}_i^b - \dot{u}_i^a \tag{2.70}$$

Again this deformation is split into a reversible part and an irreversible part

$$\Delta\dot{u}_i = \Delta\dot{u}_i^e + \Delta\dot{u}_i^p \tag{2.71}$$

The irreversible, or plastic, part of this expression is derived from a plastic potential function $g = g(t_i)$, which is now a function of the surface traction t_i

$$\Delta\dot{u}_i^p = \dot{\lambda}\,\frac{\partial g}{\partial t_i} \tag{2.72}$$

A yield function $f(t_i)$ is introduced to distinguish between elastic and elastoplastic response.

A simple linear relationship is chosen to relate an objective rate of surface traction to the elastic part of relative velocity

$$\overset{\circ}{t}_j = D^e_{jk}\,\Delta\dot{u}_k^e \tag{2.73}$$

The complete constitutive relation for the contact behaviour is obtained by combining equations (2.71–2.73)

$$\overset{\circ}{t}_j = D^{ep}_{jk}\,\Delta\dot{u}_k \tag{2.74}$$

2.6 Governing equations

To obtain the governing equation for the problem of large elastoplastic deformation, the equation of continued equilibrium should be supplemented with the constitutive relationships of the previous section.

In equation (2.25), the first two terms give the virtual work done by internal stress. The material rate of change of the first Piola-Kirchoff stress tensor, equation (2.16), relates to the Hill rate of Cauchy stress, equation (2.39), in the following way

$$\dot{\Sigma}_{ji} = \overset{\circ H}{\sigma}_{ji} - \sigma_{ki}\dot{u}_{j,k} + \sigma_{ik}\Omega_{kj} + \sigma_{jk}\Omega_{ki} \tag{2.75}$$

Consequently, the first term of equation (2.25) can be written in the form

$$\delta\dot{W}_{\sigma} = \int_V (\overset{\circ H}{\sigma}_{ji} - \sigma_{ki}\dot{u}_{j,k} + \sigma_{ik}\Omega_{kj} + \sigma_{jk}\Omega_{ki})\,\delta u_{i,j}\,dV \tag{2.76}$$

To arrive at a more suitable expression for use in the finite element formulation, we rewrite equation (2.76), namely

$$\delta\dot{W}_{\sigma} = \delta\dot{W}^{H}_{\sigma} + \delta\dot{W}^{G}_{\sigma} \tag{2.77}$$

where

$$\delta\dot{W}^{H}_{\sigma} = \int_V \overset{\circ H}{\sigma}_{ji}\delta\varepsilon_{ij}\,dV$$

$$\delta\dot{W}^{G}_{\sigma} = \int_V \left[-\sigma_{ki}\dot{u}_{j,k}(2\delta\varepsilon_{ij} - \delta u_{j,i}) + (\sigma_{ik}\Omega_{kj} + \sigma_{jk}\Omega_{ki})\,\delta u_{i,j}\right] dV$$

in which $\delta\varepsilon_{ij}$ is the symmetric part of the virtual displacement gradient. The geometric term $\delta\dot{W}^{G}_{\sigma}$ can be rearranged to give[10]

$$\delta\dot{W}^{G}_{\sigma} = \int_V \left[\sigma_{ki}\dot{u}_{j,k}\delta u_{j,i} - 2\,\sigma_{ki}\dot{\varepsilon}_{jk}\delta\varepsilon_{ij}\right] dV \tag{2.78}$$

The interface contribution to the virtual work equation (2.25) can also be split into a material part and a geometrical part by introducing the Hill rate of traction from equation (2.51)

$$\delta\dot{W}_{c} = \delta\dot{W}^{H}_{c} + \delta\dot{W}^{G}_{c} \tag{2.79}$$

where

$$\delta\dot{W}^{H}_{c} = \int_{Sc} \overset{\circ H}{\tau}_{i}\,\delta\Delta u_{i}\,dS$$

$$\delta \dot{W}_c^G = \int_{Sc} (\tau_k \Omega_{ki}^r \delta \Delta u_i + \tau_i \Delta J \ \delta u_i^r) \ dS$$

Here we introduce the difference in stretch ΔJ and the virtual displacement of the reference surface δu_i^r

$$\Delta J = J_b - J_a \qquad ; \qquad \delta u_i^r = \frac{1}{2} (\delta u_i^a + \delta u_i^b) \tag{2.80}$$

2.7 Finite element discretization

The governing equation for the problem of large elastoplastic deformation will be discretized in the sense of the displacement based finite element method. Terms in the resulting stiffness equations, relating nodal displacements to nodal forces, will be identified. A distinction is made between terms which are needed in a conventional small deformation analysis and a large deformation analysis respectively. For small deformation, the concepts which lead to a finite element stiffness equation are discussed in several text books[13,14,15]. For a large deformation analysis, however, the formulation is not unambiguous and hence several approaches and notational conventions exist[10,11,14]. Here, index notation is used for the formulation of finite element equations, because it clearly shows their structure. Moreover, it dispenses with the need to introduce additional symbolic notations. However, as the equation of continued equilibrium in its final, discretized, form is a common matrix equation, a transition to matrix and vector notation will be made at the end of this section.

The velocity field $\dot{u}_i$ is interpolated from finite element nodal displacements with the aid of shape functions N_{ij}. The virtual displacements are also restricted to the set of those functions

$$\dot{u}_i = N_{ij} \dot{a}_j \qquad ; \qquad \delta u_i = N_{ij} \delta a_j \tag{2.81}$$

Here $\dot{a}_j$ and δa_j are the nodal velocities and nodal virtual displacements respectively. The index j ranges over all nodal degrees of freedom. From this, expressions for the velocity gradient $\dot{u}_{i,k}$, the strain rate tensor $\dot{\varepsilon}_{ik}$ and the

spin tensor Ω_{ik} can be obtained

$$\begin{aligned} \dot{u}_{i,k} &= N_{ij,k}\dot{a}_j &&= L_{ijk}\dot{a}_j \\ \dot{\varepsilon}_{ik} &= \frac{1}{2}(L_{ijk} + L_{kji})\,\dot{a}_j &&= B_{ijk}\dot{a}_j \\ \Omega_{ik} &= \frac{1}{2}(L_{kji} - L_{ijk})\,\dot{a}_j &&= C_{ijk}\dot{a}_j \end{aligned} \qquad (2.82)$$

Equivalently, the expression for the virtual displacement gradient, $\delta u_{i,j}$ and its symmetrical part $\delta\varepsilon_{ij}$ are found with

$$\delta u_{i,k} = L_{ijk}\delta a_j \quad ; \quad \delta\varepsilon_{ik} = B_{ijk}\delta a_j \qquad (2.83)$$

Expressions (2.81-2.83) can be used to discretize the equation of continued equilibrium

$$-\delta\dot{W}_\sigma - \delta\dot{W}_c + \delta\dot{W}_\gamma + \delta\dot{W}_t = 0 \qquad (2.84)$$

The first term of this equation was specified in expression (2.77). Upon substitution of results (2.81-2.83), the material part of this term yields

$$\delta\dot{W}^H_\sigma = \int_V \overset{\circ H}{\sigma}_{ij}\delta\varepsilon_{ij}\,dV = \delta a_q \left[\int_V B_{iqj}\overset{\circ H}{\sigma}_{ij}\,dV\right] \qquad (2.85)$$

Further differentiation in a material linear part and a material non-linear part is possible when equations (2.62) and (2.68) are employed

$$\delta\dot{W}^H_\sigma = \delta a_q K^e_{qp}\dot{a}_p - \delta a_q K^p_{qp}\dot{a}_p \qquad (2.86)$$

where

$$K^e_{qp} = \int_V B_{iqj}D^e_{ijkl}B_{kpl}\,dV$$

$$K^p_{qp} = \int_V B_{iqj}(D^e_{ijkl} - D^{ep}_{ijkl})B_{kpl}\,dV$$

Note that, due to definition (2.82), B_{ijk} is symmetric with respect to the first and the last index, $B_{ijk} = B_{kji}$. Consequently, both matrices are symmetric, at least when considering isotropic behaviour and plastic flow derived from an associated flow rule. For non-associated plasticity, the second matrix becomes non-symmetric.

Up to this point, the formulation has been classical and could have been developed equally well in standard vector and matrix notation. However, the

treatment of the geometric part of the stress term in equation (2.84) would require the introduction of special symbolic notations[10,11]. But no such need arises when index notation is used. Discretization of equation (2.78) yields the desired expression for this part, namely

$$\delta \dot{W}^{G}_{\sigma} = \delta a_{q} K^{G}_{qp} \dot{a}_{p} \tag{2.87}$$

where

$$K^{G}_{qp} = \int_{V} (L_{jpk} \sigma_{kl} L_{jqi} - 2\, B_{jpk} \sigma_{kl} B_{iqj})\, dV$$

Again, this matrix is symmetric.

For the interface contribution to the virtual work equation, new shape functions need to be introduced. The velocity of the reference surface $\dot{u}^{r}_{i}$, equation (2.53), and its virtual displacement δu^{r}_{i} are interpolated from nodal displacements with the shape function N^{r}_{ij}.

$$\dot{u}^{r}_{i} = N^{r}_{ij} \dot{a}_{j} \qquad ; \qquad \delta u^{r}_{i} = N^{r}_{ij} \delta a_{j} \tag{2.88}$$

The virtual slip is derived from the shape functions ΔN_{ij}

$$\delta \Delta u_{i} = \Delta N_{ij} \delta a_{j} \tag{2.89}$$

Consequently, the spin tensor for the reference surface, Ω^{r}_{ij}, can be expressed as

$$\Omega^{r}_{ik} = \frac{1}{2} (N^{r}_{kj,i} - N^{r}_{ij,k})\, \dot{a}_{j} = C^{r}_{ijk} \dot{a}_{j} \tag{2.90}$$

Equation (2.79) for the geometric part of the interface contribution to the virtual work expression contains the difference in stretch of both surfaces

$$\Delta J = \Delta \dot{\varepsilon}_{kk} - n_{k} n_{l} \Delta \dot{\varepsilon}_{kl} \tag{2.91}$$

where $\Delta \dot{\varepsilon}_{kl} = \dot{\varepsilon}^{b}_{kl} - \dot{\varepsilon}^{a}_{kl}$. The difference in strain rate is interpolated over nodal values with the shape functions of expression (2.89)

$$\Delta \dot{\varepsilon}_{ik} = \frac{1}{2} (\Delta N_{ij,k} + \Delta N_{kj,i})\, \dot{a}_{j} = \Delta B_{ijk} \dot{a}_{j} \tag{2.92}$$

The second term of the equation of continued equilibrium can be discretized with expressions (2.88) and (2.89). For the material part of this term,

equation (2.79), substitution yields

$$\delta\dot{W}_c^H = \int_{S_c} \overset{\circ H}{\tau}_i \, \delta\Delta u_i \, dS = \delta a_q \left[\int_{S_c} \Delta N_{iq} \overset{\circ H}{\tau}_i dS \right] \tag{2.93}$$

Equations (2.73) and (2.74) are used to split this result in a material linear part and a material non-linear part

$$\delta\dot{W}_c^H = \delta a_q \, K^e_{qp} \, \dot{a}_p - \delta a_q \, K^p_{qp} \, \dot{a}_p \tag{2.94}$$

where

$$K^e_{qp} = \int_{S_c} \Delta N_{iq} D^e_{ij} \Delta N_{jp} dS$$

$$K^p_{qp} = \int_{S_c} \Delta N_{iq} (D^e_{ij} - D^{ep}_{ij}) \, \Delta N_{jp} dS$$

Both matrices are symmetric when $D^e_{ij} = D^e_{ji}$ and when associated flow is considered, i.e. when $D^{ep}_{ij} = D^{ep}_{ji}$. The geometric part of the interface term follows from substitution of equations (2.88) and (2.89) in the definition of this term (2.79)

$$\delta\dot{W}_c^G = \delta a_q \, K^G_{qp} \, \dot{a}_p \tag{2.95}$$

where

$$K^G_{qp} = \int_{S_c} \left[C^r_{jpi} \tau_j \Delta N_{iq} + (\Delta B_{kpk} - n_k n_l \Delta B_{kpl}) \, \tau_i N^r_{iq} \right] dS$$

This matrix is non-symmetric irrespective of the constitutive relation used.

The load terms in equation (2.84) do not differ from the usual small deformation expressions when only dead loading is considered

$$\delta\dot{W}_\gamma = \int_V \dot{\gamma}\rho g_i \, \delta u_i dV = \delta a_q \left[\int_V N_{iq} \dot{\gamma}\rho g_i dV \right] = \delta a_q \, \dot{f}^\gamma_q \tag{2.96}$$

$$\delta\dot{W}_t = \int_S \dot{t}\rho_s n_i \, \delta u_i dS = \delta a_q \left[\int_S N_{iq} \dot{t}\rho_s n_i dS \right] = \delta a_q \, \dot{f}^t_q \tag{2.97}$$

The equation of continued equilibrium in its discretized form is obtained when each term in equation (2.84) is replaced by its finite element counterpart. For notational convenience, matrix and vector notation is used

$$-\delta\underline{a}^T(\underline{\underline{K}}^e - \underline{\underline{K}}^p + \underline{\underline{K}}^G) \, \dot{\underline{a}} + \delta\underline{a}^T(\dot{\underline{f}}^\gamma + \dot{\underline{f}}^t) = \underline{0} \tag{2.98}$$

Here the interface contribution has been included in the terms for the

continuum. The above expression should be zero for every virtual displacement within the set of shape functions; i.e. for every $\delta\underline{a}$. Consequently, continued equilibrium requires

$$\underline{\underline{K}}_T \dot{\underline{a}} = \dot{\underline{f}}^{\gamma} + \dot{\underline{f}}^{t} \tag{2.99}$$

where

$$\underline{\underline{K}}_T = \underline{\underline{K}}^{e} - \underline{\underline{K}}^{P} + \underline{\underline{K}}^{G}$$

Here $\underline{\underline{K}}_T$ is the tangent stiffness matrix. Matrix $\underline{\underline{K}}^{G}$ is usually disregarded in a small deformation analysis, except when studying phenomena like buckling. All effects of non-linearity are incorporated in the plastic reduction matrix $\underline{\underline{K}}^{P}$.

APPENDIX A

In this appendix a derivation is given of equations (2.28) and (2.31), which are needed for the development of the objective stress rates in section (2.3).

During a deformation from the current configuration at $t=t_0$ to the one at $t=t_1$, Figure (2.4), the components of a surface vector change according to Nanson's formula[2,14]

$$dA_i^1 = \frac{\rho_0}{\rho_1} \frac{\partial x_j^0}{\partial x_i^1} dA_j^0 \tag{A1}$$

As observed in section 2.3, the force on a surface element keeps the direction of the line element with which it was aligned in the configuration at $t=t_0$. This implies that the components of the force change in a similar way as the components of a material line element

$$dx_i^1 = \frac{\partial x_i^1}{\partial x_j^0} dx_j^0 \qquad \text{and} \qquad df_i^1 = \frac{\partial x_i^1}{\partial x_j^0} df_j^0 \tag{A2}$$

If we now introduce the deformation gradient C_{ij}

$$C_{ij} = \frac{\partial x_i^1}{\partial x_j^0} \tag{A3}$$

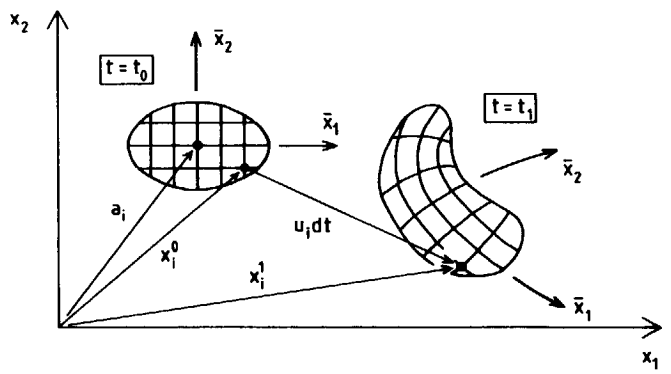

Figure 2.4. Relationship between subsequent configurations of a deforming body.

then, by applying the chain rule for differentiation, it is easily verified that its inverse is given by

$$C^{-1}_{ij} = \frac{\partial x^0_i}{\partial x^1_j} \tag{A4}$$

where we define C^{-1} as

$$C^{-1}_{ij} C_{jk} = \delta_{ik} \tag{A5}$$

When these notations are used in formulae (A1) and (A2), equation (2.28) is obtained.

$$\begin{aligned} df^1_i &= C_{ij}\, df^0_j \\ dA^1_i &= \rho_0/\rho_1\; C^{-1}_{ji}\; dA^0_j \end{aligned} \tag{2.28}$$

The deformation from the configuration at $t=t_0$ to the one at $t=t_1$ is given by

$$x^1_i = x^0_i + \dot{u}_i dt \tag{A6}$$

This result can be used to elaborate the deformation gradient for a small

increment of time dt

$$C_{ij} = \delta_{ij} + \dot{u}_{i,j}dt = \delta_{ij} + (\dot{\varepsilon}_{ij} - \Omega_{ij})dt \tag{A7}$$

The spin tensor Ω_{ij} is defined by

$$\Omega_{ij} = \frac{1}{2}(\dot{u}_{j,i} - \dot{u}_{i,j}) \tag{A8}$$

The ratio of the subsequent densities follows from the equation of continuity

$$\rho_1 = \rho_0 + \dot{\rho}\, dt = \rho_0(1 - \dot{u}_{m,m}dt) \tag{A9}$$

or equivalently

$$\rho_1/\rho_0 = 1 - \dot{u}_{m,m}dt \tag{A10}$$

Thus, all identities of equation (2.31) have been derived.

3. SOLUTION OF NON-LINEAR FINITE ELEMENT EQUATIONS

The incremental equation of continued equilibrium, as developed in the previous section, will have to be integrated numerically. To prevent a drift from the true equilibrium path, some form of equilibrium iteration process should be employed. For the non-associated plasticity problems, as considered in this study, convergence of this process is not guaranteed. A converged solution can only be obtained for relatively small increments of load and displacement. Consequently, tracing of the entire equilibrium path up to and beyond limit points requires an incremental-iterative approach. The choice of step sizes proves to be very critical. Too large step sizes lead to divergence and too small step sizes make the analysis unfeasible. In addition, suitable step sizes may vary considerably during an analysis, especially for frictional material.

In this chapter the convergence properties of the equilibrium iteration scheme are discussed. On the basis of this analysis a procedure is developed for the automatic correction of step sizes. The practical application of this procedure is demonstrated for some problems of soil-structure interaction. Typical differences between analyses for associated and non-associated plasticity problems become evident.

3.1 Equilibrium equations for finite increments

The equation of continued equilibrium gives a relation for infinitesimal changes of loads and displacements. Straightforward application of the resulting finite element equation (2.99) to finite increments implies linearization and will introduce equilibrium errors. Consequently, some iteration process should be used to reduce this error to within pre-defined bounds. In the literature[13-21] on non-linear finite element computations several methods have been introduced. Among the best known are the full and modified Newton-Raphson methods and the initial stiffness method. In addition, several procedures have been developed to enhance their performance. Line searches and overrelaxation can in some cases improve convergence speed considerably. Quasi-Newton procedures, like the BFGS method, present an alternative to the above iteration schemes. They try to combine the speed of

the full Newton method with the economy of the modified methods by choosing a simple update of the iteration matrix.

In this section a general formulation is given of an equilibrium iteration scheme. Its convergence properties are discussed.

3.1.1. Equilibrium iterations

To test equilibrium at the end of a finite increment of load and displacement, the discretized form of equation (2.7) is needed. The introduction of finite element shape functions (2.81), (2.83) and (2.89) into this equation yields

$$\int_V \underline{\underline{B}}^T \underline{\sigma}\, dV + \int_S \Delta\underline{\underline{N}}^T \underline{\tau}\, dS = \int_V \underline{\underline{N}}^T \underline{\gamma}\, dV + \int_S \underline{\underline{N}}^T \underline{t}\, dS \tag{3.1}$$

where the Cauchy stress tensor has been rearranged into a vector. This equation can be simplified by introducing an external load vector $\underline{f}^{ex}$, an internal load vector $\underline{f}^{in}$, and the out-of-balance vector $\underline{r}$

$$\underline{f}^{in} = \int_V \underline{\underline{B}}^T \underline{\sigma}\, dV + \int_S \Delta\underline{\underline{N}}^T \underline{\tau}\, dS \tag{3.2}$$

$$\underline{f}^{ex} = \int_V \underline{\underline{N}}^T \underline{\gamma}\, dV + \int_S \underline{\underline{N}}^T \underline{t}\, dS \tag{3.3}$$

$$\underline{r} = \underline{f}^{ex} - \underline{f}^{in} \tag{3.4}$$

Equation (3.1) is now transformed into the expression $\underline{r} = \underline{0}$, which depends on increments of load and displacement. To arrive at a suitable iteration scheme, we may add an arbitrary force vector, say $\underline{\underline{K}}\Delta\underline{a}$, on both sides of this equilibrium condition

$$\underline{\underline{K}}\, \Delta\underline{a} = \underline{\underline{K}}\, \Delta\underline{a} + \underline{r} \tag{3.5}$$

where $\Delta\underline{a}$ is the increment of nodal displacement. Obviously, this addition will have no influence at all on the solution of the original equation. Equation (3.5) can simply be used as a predictor-corrector scheme

$$\underline{\underline{K}}_{k-1}\, \Delta\underline{a}_k = \underline{\underline{K}}_{k-1}\, \Delta\underline{a}_{k-1} + \underline{r}_{k-1} \tag{3.6}$$

where k denotes the iteration number. This equation embodies a number of

well-known iteration schemes. For example, if matrix $\underline{\underline{K}}$ is taken to be equal to the tangent stiffness matrix at the last iterate, we arrive at the full Newton-Raphson procedure. When matrix $\underline{\underline{K}}$ is kept constant during the iteration process, a modified Newton method is obtained.

3.1.2. Convergence properties of the modified Newton method

The convergence properties of equation (3.6) depend on the choice of matrix $\underline{\underline{K}}$. Those properties will now be examined. The results can be used as a basis for the automatic step size procedure of section 3.3.

The reduction of the out-of-balance vector (3.4) in subsequent iterations determines the convergence properties of the iteration process. An increment of this vector is defined as

$$\dot{\underline{r}} = \dot{\underline{f}}^{ex} - \dot{\underline{f}}^{in} \tag{3.7}$$

Comparison of this to the equation of continued equilibrium (2.99) yields for the increment of internal force

$$\dot{\underline{f}}^{in} = \underline{\underline{K}}_T \, \dot{\underline{a}} \tag{3.8}$$

where $\underline{\underline{K}}_T$ is the tangent stiffness matrix. This relation specifies the change of the internal force vector for an infinitesimal change of displacement. For an analysis of the convergence properties of scheme (3.6) we need a relation between sub-increments of force and displacement, which can be obtained by integration of equation (3.8)

$$\delta \underline{f}_k^{in} = \int_{t_{k-1}}^{t_k} \underline{\underline{K}}_T \, \dot{\underline{a}} \, dt = \underline{\underline{S}}_k \, \delta \underline{a}_k \tag{3.9}$$

where

$$\delta \underline{f}_k^{in} = \underline{f}_k^{in} - \underline{f}_{k-1}^{in} \tag{3.10}$$

$$\delta \underline{a}_k = \Delta \underline{a}_k - \Delta \underline{a}_{k-1} \tag{3.11}$$

are sub-increments of force and displacement respectively. Matrix $\underline{\underline{S}}$ will be called the secant matrix for sub-increments. The existence of such a matrix follows from the mean value theorem for integrals. Near the solution, where

the equilibrium path may be linearized, matrix $\underline{\underline{S}}$ approaches the tangent stiffness matrix, so we have $\underline{\underline{S}}_{\infty} = \underline{\underline{K}}_T$ for a converging solution. Note that we do not use an explicit expression for matrix $\underline{\underline{S}}$ in the remainder of this study.

A sub-increment of the out-of-balance vector is obtained by integrating equation (3.7) and substituting from expression (3.9)

$$\delta \underline{r}_k = \delta \underline{f}_k^{ex} - \underline{\underline{S}}_k \, \delta \underline{a}_k \tag{3.12}$$

The sub-increment of displacement $\delta \underline{a}_k$ results from an equilibrium correction according to equation (3.6). With this equation, vector $\delta \underline{a}_k$ can be expressed in terms of the out-of-balance vector, which on substitution in the above equation yields

$$\delta \underline{r}_k = \delta \underline{f}_k^{ex} - \underline{\underline{S}}_k \, \underline{\underline{K}}^{-1} \underline{r}_{k-1} \tag{3.13}$$

In an iteration scheme without so-called indirect displacement control[18-24] the load level is kept constant within a load step. This implies that in such a case the sub-increment of the external load vanishes. Later on, when indirect displacement control is introduced, it will be shown that in general $\delta \underline{f}^{ex}$ can be expressed in terms of the out-of-balance vector. However, for the time being, only the case in which $\delta \underline{f}^{ex}$ vanishes will be considered. Hence, the vector $\delta \underline{f}^{ex}$ can now be eliminated from equation (3.13). In this way, we obtain a matrix equation with a new matrix $\underline{\underline{A}}$, i.e.

$$\underline{r}_k = \underline{\underline{A}}_k \, \underline{r}_{k-1} \; ; \quad \underline{\underline{A}}_k \equiv (\underline{\underline{I}} - \underline{\underline{S}}_k \, \underline{\underline{K}}^{-1}) \tag{3.14}$$

There is a great similarity between this relation and the iteration scheme used in the so-called power iteration method[25] for determining eigenvalues and eigenvectors of matrix $\underline{\underline{A}}$. Indeed the only difference is that in the power method matrix $\underline{\underline{A}}$ is constant for all iterations, whereas this matrix $\underline{\underline{A}}_k$ changes during the equilibrium iteration process. After some iterations, however, matrix $\underline{\underline{A}}_k$ hardly changes any more, as matrix $\underline{\underline{S}}_k$ approaches the tangent stiffness $\underline{\underline{S}}_{\infty}$. In fact, for large k, equation (3.14) could be seen as the power iteration scheme for determining the largest absolute eigenvalue of matrix $\underline{\underline{A}}_{\infty}$. One useful property of the power method will be stated here without proof. For sufficiently large k values we have:

$$\underline{r}_k \approx \alpha_m \, \underline{r}_{k-1} \tag{3.15}$$

where α_m stands for the largest eigenvalue of matrix $\underline{\underline{A}}_\infty$, in the absolute sense. During the iterative process this largest eigenvalue is estimated by computing the Rayleigh quotient[25]

$$\alpha_m \approx R \equiv \frac{(\underline{r}_{k-1})^T \underline{\underline{A}}_k \underline{r}_{k-1}}{(\underline{r}_{k-1})^T \underline{r}_{k-1}} = \frac{(\underline{r}_{k-1})^T \underline{r}_k}{(\underline{r}_{k-1})^T \underline{r}_{k-1}} \tag{3.16}$$

Note that the Rayleigh quotient tends to give a very good estimate for the maximum eigenvalue. For a symmetric matrix, the computed Rayleigh quotient approximates α_m with an error in the order of ε^2, at least in the case where vector $\underline{r}_{k-1}$ approximates the largest eigenvector with an error in the order of ε. For instance, it gives a better result than the estimate obtained by taking the ratio of the norms of two successive iterates.

Having obtained the above results, the convergence properties of the equilibrium iteration process become evident. Equation (3.15) shows that local convergence is obtained for values in the range between minus one and one, i.e. $\alpha \in (-1,1)$. Unfortunately, a formal proof of local convergence can only be given for the case of small deformation plasticity in which plastic strain is derived from an associated flow rule. In addition, the iteration scheme should be of the initial stiffness type with $\underline{\underline{K}} = \underline{\underline{K}}_e$, the elastic stiffness matrix. In fact, it is proved in reference (26) that this method even involves global convergence, i.e. convergence independent of step size. In section 3.5, where a specialization to small deformation plasticity is made, the proof for local convergence will be given.

3.2 Error estimates and convergence criteria

To determine whether or not the computed state is sufficiently close to a real equilibrium point, some form of convergence criterion should be applied. In the literature, references (19,24,26-29), several such criteria are suggested and discussed. Most of these criteria judge the change of results for subsequent iterations. These criteria can be of a local nature, checking stresses in Gaussian integration points, or of a global nature, checking either on the out-of-balance forces or sub-increments of displacement. In limit load computations quantitative control over the accuracy of computed

forces is of the utmost importance. This suggests that in such a case a criterion on the forces should be used. The same applies for computations of reactional forces on embedded structures and foundations. Here it will be shown that the well-known criterion on the out-of-balance forces may not give correct information on the accuracy of results when displacement control or arc-length methods are used. Consequently, preset convergence tolerances do not reflect the true accuracy of a converged solution in the above situations. In the literature on non-linear finite element computations this seems to have resulted in excessively small values for those tolerances and the adoption of additional criteria without a clear physical interpretation. However, in the author's opinion, this is not a satisfactory approach. Lack of information on the true accuracy may lead either to inaccurate results or to excessive computation. To correct this situation a definition is given of the out-of-solution error estimate which can be used to assess the true accuracy of load-displacement curves.

3.2.1. Out-of-balance error

The criterion on the out-of-balance forces is defined by

$$\varepsilon_k^r \equiv \frac{\| \underline{f}_k^{in} - \underline{f}^{ex} \|}{\| \underline{f}^{ex} \|} < \bar{\varepsilon}^r \tag{3.17}$$

where ε^r is the actual relative error and $\bar{\varepsilon}^r$ is a preset convergence tolerance.

For load-control, surface tractions or body forces are applied and kept constant during the iterative process for a load increment. Hence, the load vector $\underline{f}^{ex}$ in equation (3.17) is known precisely and the internal reaction force, $\underline{f}^{in}$, is no more out-of-balance than the prescribed tolerance. As a result load-displacement curves will show the desired accuracy.

For displacement-control the situation is quite different. Here displacement increments are prescribed along a part of the boundaries. The external load $\underline{f}^{ex}$ comes from the forces at the nodes with prescribed displacements. During the iterative process back calculations are needed to estimate $\underline{f}^{ex}$ for each

iteration. Hence equation (3.17) becomes

$$\varepsilon_k^r \equiv \frac{\| \underline{f}_k^{in} - \underline{f}_k^{ex} \|}{\| \underline{f}_k^{ex} \|} < \bar{\varepsilon}_r \tag{3.18}$$

Because the external forces are not precisely known, the error measure loses its physical meaning. The disadvantage of error measure (3.18) is that it only judges the difference between two inexact vectors, for both $\underline{f}_k^{in}$ and $\underline{f}_k^{ex}$ differ from the true solution $\underline{f}_\infty$. Strictly speaking $\underline{f}_k^{in}$ and $\underline{f}_k^{ex}$ may be close to each other but may still be far from the solution. In such a case inaccurate results are obtained; an illustrative example is given later on.

3.2.2. The out-of-solution error

For (indirect) displacement control, the out-of-balance error (3.18) may deviate significantly from the out-of-solution error for the forces as defined by the equation

$$\varepsilon_k^f \equiv \frac{\| \underline{f}_k^{in} - \underline{f}_\infty^{in} \|}{\| \underline{f}_\infty^{in} \|} \tag{3.19}$$

where $\underline{f}_\infty^{in}$ (= $\underline{f}_\infty^{ex}$) is the real external load as would be obtained in the limit for k to infinity. For this reason error measure (3.19) will be elaborated to obtain an objective error estimate in the case of (indirect) displacement control.

As the final solution is unknown during the iteration process, it should be written in terms of known quantities:

$$\underline{f}_\infty^{in} = \underline{f}_k^{in} + \sum_{n=k+1}^{\infty} \delta \underline{f}_n^{in} \quad ; \quad \delta \underline{f}_n^{in} \equiv \underline{f}_n^{in} - \underline{f}_{n-1}^{in} \tag{3.20}$$

Combination of equations (3.15) and (3.6) shows that

$$\delta \underline{a}_k \cong \alpha_m \, \delta \underline{a}_{k-1} \tag{3.21}$$

at least when the iteration matrix does not change, as in the modified Newton schemes. A similar statement can be made for sub-increments of $\underline{f}^{in}$.

Combination of the above relation and equation (3.9) shows that

$$\delta \underline{f}_k^{in} = \underline{\underline{S}}_k \delta \underline{a}_k \approx \alpha_m \underline{\underline{S}}_k \delta \underline{a}_{k-1} \tag{3.22}$$

Near the solution, where $\underline{\underline{S}}_k \approx \underline{\underline{S}}_{k-1}$, this becomes

$$\delta \underline{f}_k^{in} \approx \alpha_m \delta \underline{f}_{k-1}^{in} \tag{3.23}$$

After inserting this expression into equation (3.20) and elaborating the sum, it is found that

$$\underline{f}_{-\infty}^{in} \approx \underline{f}_k^{in} + \frac{\alpha_m}{1 - \alpha_m} \delta \underline{f}_k^{in} \tag{3.24}$$

Finally we find for the proposed error measure of equation (3.19)

$$\varepsilon_k^f = |\alpha_m| \frac{\| \underline{f}_k^{in} - \underline{f}_{k-1}^{in} \|}{\| \underline{f}_k^{in} - \alpha_m \underline{f}_{k-1}^{in} \|} \tag{3.25}$$

This measure will be referred to as the out-of-solution error. It should be emphasized that this measure is of an approximate nature. Therefore it can only be used in addition to convergence criteria like the out-of-balance criterion.

The accuracy of displacements can be estimated from an out-of-solution error for the displacements. This measure is defined in complete analogy to equation (3.19)

$$\varepsilon_k^a \equiv \frac{\| \underline{a}_k - \underline{a}_{-\infty} \|}{\| \underline{a}_{-\infty} \|} \tag{3.26}$$

Vector $\underline{a}_{-\infty}$ can be written as a sum of sub-increments of displacements, which in turn satisfy equation (3.21) By applying the same reasoning as for the force criterion (3.25), we obtain the following expression for the out-of-solution error for displacements

$$\varepsilon_k^a = |\alpha_m| \frac{\| \underline{a}_k - \underline{a}_{k-1} \|}{\| \underline{a}_k - \alpha_m \underline{a}_{k-1} \|} \tag{3.27}$$

It is interesting to note that Schmidt[27] arrived at an error estimate that shows some similarity to equations (3.25) and (3.27). Schmidt arrived at his result by postulating that his particular iteration process is of the contractive mapping type.

3.3 An automatic step size correction scheme

Models for granular materials show a high level of non-normality in the flow rule when a high friction angle is combined with a low angle of dilation. This non-normality may give rise to a situation in which stress increments perform negative incremental work on strain increments, thus yielding an unstable material response which resembles softening behaviour[22,30,31]. This type of material behaviour may give rise to a non-converging iterative process. Special care should therefore be taken when choosing appropriate step sizes.

Another difficulty encountered for cohesionless soils may occur in the very beginning of loading. Consider for example the indentation of a plate into purely frictional material. In this case significant plastic deformations occur in the very beginning of loading as normal stresses have to develop before the granular material can sustain any shear stress. Such problems can be solved by applying extremely small load increments at the onset of loading. Later on the step size must be increased to avoid an endless computation, whereas finally in near-collapse states, step sizes have to be reduced again for reasons of convergence. In fact, the user of a computer code needs considerable skill and experience to select suitable step sizes for non-associated plasticity problems. For some problems, even an experienced researcher may fail to select suitable step sizes. Hence there is a need for an automatic step size correction scheme.

In this section an automatic step size correction scheme will be developed whose scaling decisions do not depend on extrapolation from one step to the next. It will use only the information gained in the step under analysis.

3.3.1. Review of previous work

In the literature on non-linear finite element calculations, some authors have already focused attention on automating the incremental procedure,

references (17,18,19,23,24,27). Roughly speaking, all existing routines are based on choosing an a priori step size based on numerical information gained in the previous step, or by deriving information from an extrapolation of the load displacement path. For example Crisfield[23] uses a simple extrapolation of the step size by assuming that it is equal to the previous size multiplied by a scaling factor. This scaling factor depends on the ratio between the previous number of iterations and the desired number of iterations:

$$\Delta s_{new} = \left(\frac{n_{des}}{n_{old}} \right)^{\beta} \Delta s_{old} \tag{3.28}$$

where Δs_{new} is the new step size, Δs_{old} is the previous step size, n_{old} is the number of iterations in the previous step, n_{des} is the desired number of iterations and β is an empirical constant.

Bergan et al.[17] introduced two methods based on the extrapolation of the load displacement path. The first method is based on the requirement that the curvature change of the path is equal for all steps. In the second method Bergan et al. compute the difference that exists between two solution estimates obtained from a linear and a parabolic extrapolation respectively. Then a step size is obtained by specifying a tolerated value for this difference. These methods by Crisfield and by Bergan are attractive since they require the input of very few empirical constants.

We studied the applicability of some existing schemes and obtained good results in the case of associated plasticity problems, i.e. for stable material behaviour. For non-associated plasticity, however, the results were no better than with manually selected step sizes. For high degrees of non-normality the schemes may even break down completely. This poor performance of the extrapolation-based methods seems to be due to the non-stable material behaviour. Non-associated plasticity tends to induce spurious perturbations in the numerically integrated load-displacement path. For low degrees of non-normality this is less pronounced, but it does become visible in computational results for high degrees of non-normality. Figure (3.1) shows the computed load-displacement curve for a smooth circular footing on a highly frictional soil. In this example the friction angle is forty degrees, whereas the dilation angle equals zero, yielding in this way a high level of non-normality. The computed load-displacement path is quite ragged.

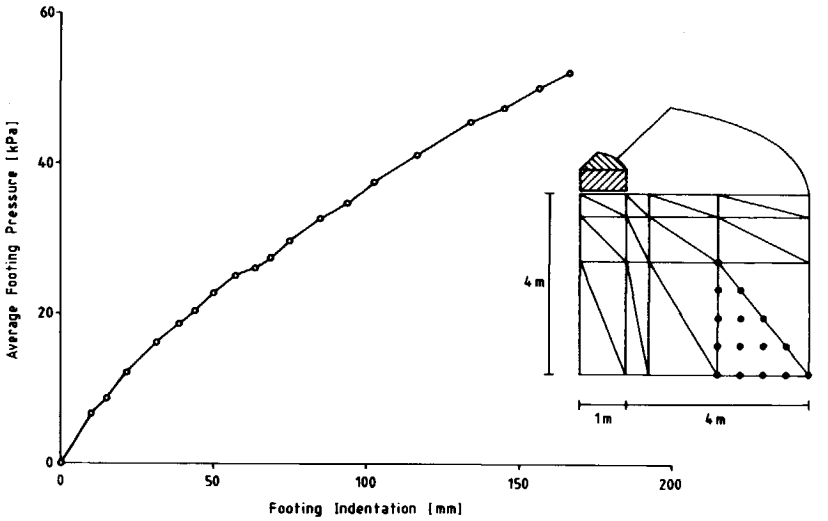

Figure 3.1. Ragged load-displacement curve as obtained for extremely non-associated material behaviour.

3.3.2 A step size correction procedure

So far attention has been paid to solving the equilibrium equations for a single load step. Now attention is focused on tracing the entire equilibrium path and on suitable magnitudes of the load increments. An automatic selection of suitable step sizes is particularly important for non-associated plasticity as the step size is critical with respect to the convergence of the iterative process. Too large steps lead to a non-converging iterative process; too small steps to an uneconomic procedure. The automatic step size correction procedure consists of two elements. First a crude extrapolation of the load-displacement curve from previous loading steps. Second a step size scaling during the iterative process. Scaling is used as soon as the estimated number of iterations is either too small or too large.

A first prediction for the new increments of load multipliers and displacements is obtained by the linear extrapolation:

$$\underset{\sim}{\Delta a}_{0} = \underset{\sim}{\Delta a}_{\text{previous step}} \; ; \; \underset{\sim}{\Delta f}^{ex}_{0} = \underset{\sim}{\Delta f}^{ex}_{\text{previous step}} \tag{3.29}$$

Experience shows that such an extrapolation may improve the convergence speed by a factor of 2 as compared to the situation without extrapolation. An extensive study into the use of higher order extrapolations leads to the conclusion that this would be attractive for problems of associated plasticity. However in non-associated problems, the efficiency was not increased at all when a higher-order extrapolation was adopted.

During the iteration process the number of iterations up to convergence may be estimated. Indeed, it follows from equation (3.15) that two successive errors relate as

$$\varepsilon_{k} \approx |\alpha_{m}| \; \varepsilon_{k-1} \tag{3.30}$$

and consequently

$$\varepsilon_{k+n} \approx |\alpha_{m}|^{n} \; \varepsilon_{k} \tag{3.31}$$

for all possible values of n. If we assume that n is the additional number of iterations up to convergence for $\varepsilon_{k+n} = \bar{\varepsilon}$, where $\bar{\varepsilon}$ is the prescribed convergence tolerance, then it follows from equation (3.31) that

$$n = \frac{\log \bar{\varepsilon} - \log \varepsilon_{k}}{\log |\alpha_{m}|} \tag{3.32}$$

Obviously the total number of iterations within a load step is not n but k+n. If we specify the desired minimum and maximum number of iterations per step, say K_{max} and K_{min} respectively, three different situations may occur

$k+n < K_{min}$	: step size to be scaled up
$K_{min} \leq k+n \leq K_{max}$	: no scaling
$K_{max} < k+n$	: step size to be scaled down

At this moment we are scaling up or down simply by doubling or halving the step size, but obviously more sophisticated scaling rules might be applied. A

new step is started with the step size obtained at the end of the previous step. This is the main difference between this automatic scheme and the ones described in the literature. Most existing procedures use an adaptive step size for the extrapolation and do not adapt during the iteration process. The present method uses a continuous prediction, which eliminates the need to choose a suitable step size before the iteration process is started.

Although the quality of the first step size is not of major importance, owing to the fact that it is continuously adapted, we still have to make a choice. An efficient option is to choose the first step in such a way that only one Gauss point will reach a plastic stress state. In practical calculations this proves to be a successful approach. If the material has already experienced plastic yielding due to previous loading programs this method will fail. In such case some crude estimate made by the user or the program will suffice.

3.4 Indirect displacement control

For collapse load computations either direct or indirect displacement control[18-24] is needed to enable limit points to be traced. Indirect displacement control is obtained by means of arc-length methods. In such methods the load level may vary during the iteration process. In this way an increment of load can become zero or even negative when a limit point is passed. For the determination of the load level a so-called constraint equation is introduced.

In this section, the equilibrium iteration equation will be formulated for indirect displacement control. It is shown that the results of the previous sections remain valid.

For proportional loading, the external load becomes

$$\underline{f}^{ex} = \mu \, \underline{f} \tag{3.33}$$

where μ is a load multiplier and $\underline{f}$ is a vector for the direction of loading. A load increment is obtained by incrementing the multiplier μ. In the case of a variable load level, the sub-increment of displacement follows from

equilibrium scheme (3.6) and the above definition of external load

$$\delta \underline{a}_{k+1} = \underline{\underline{K}}_k^{-1}(\mu_k \underline{f} - \underline{f}_k^{in}) \tag{3.34}$$

For the solution of the load multiplier a constraint equation is needed. In this study a linear equation of the form

$$\underline{b}^T \delta \underline{a}_{k+1} = 0 \tag{3.35}$$

is used, where vector $\underline{b}$ is kept constant during the iteration process. For $\underline{b} = \Delta \underline{a}_0$ a conventional linearized arc-length method[19-22] is obtained. From this equation the load multiplier μ_k can be solved

$$\mu_k = \frac{\underline{b}^T \underline{\underline{K}}_k^{-1} \underline{f}_k^{in}}{\underline{b}^T \underline{\underline{K}}_k^{-1} \underline{f}} \tag{3.36}$$

When matrix $\underline{\underline{K}}$ does not change, as in the modified Newton-Raphson scheme, the same equation holds for increments of μ_k and $\underline{f}_k^{in}$. Substitution of this in the definition of a sub-increment of the out-of-balance vector yields

$$\delta \underline{r}_k = \delta \mu_k \underline{f} - \delta \underline{f}_k^{in} = (\underline{\underline{P}} - \underline{\underline{I}})\ \delta \underline{f}_k^{in} \tag{3.37}$$

where

$$\underline{\underline{P}} = \frac{\underline{f}\ \underline{b}^T \underline{\underline{K}}^{-1}}{\underline{b}^T \underline{\underline{K}}^{-1} \underline{f}} \tag{3.38}$$

Substitution from expression (3.9) and (3.6) gives

$$\delta \underline{r}_k = (\underline{\underline{P}} - \underline{\underline{I}})\ \underline{\underline{S}}_k\ \underline{\underline{K}}^{-1} \underline{r}_{k-1} \tag{3.39}$$

By writing $\delta \underline{r}_k$ in full, the following error reduction equation is obtained

$$\underline{r}_k = \underline{\underline{A}}_k^* \underline{r}_{k-1} \qquad ; \qquad \underline{\underline{A}}_k^* = (\underline{\underline{I}} + (\underline{\underline{P}} - \underline{\underline{I}})\ \underline{\underline{S}}_k\ \underline{\underline{K}}^{-1}) \tag{3.40}$$

The existence of a relationship of this kind ensures that the developments of the previous sections remain valid for a modified Newton-Raphson scheme.

3.5 Specialization to small deformation elastoplasticity

The initial stiffness method proves to have some attractive features when used as an iteration scheme for problems of small deformation elastoplasticity. As many of the problems in soil mechanics can be treated as such, some special attention will be given to this method here.

3.5.1. An accelerated initial stiffness method

The initial stiffness method has three pleasant features for small deformation plasticity computations. First of all the elasticity matrix remains constant for all loading steps, so that it has to be decomposed only once for the entire series of loading steps. Secondly the basically slow initial stiffness method can easily be upgraded by choosing appropriate values for the first iterate. By extrapolating results from previous load increments, we obtain good starting values for the iteration process.

For an angular yield surface, as implied by the Coulomb model or the Tresca model, the initial stiffness method has a third advantage. The resulting yield vertices at the ridges of the yield surfaces can be incorporated straightforwardly, whereas it is difficult to update the tangent stiffness matrix.

When using the elastic stiffness matrix, and also an overrelaxation factor, ω, equation (3.6) becomes

$$\underline{\underline{K}}_e \, \underline{\Delta a}_k = \underline{\underline{K}}_e \, \underline{\Delta a}_{k-1} + \omega \, \underline{r}_k \tag{3.41}$$

where $\underline{\Delta a}_0$ is extrapolated from the previous step. The values to be chosen for ω, to ensure a converging process, are restricted. This topic is addressed in the next section.

3.5.2. Overrelaxation and local convergence

For an associated flow rule, and no overrelaxation (ω=1.0), it is shown in Appendix B that all eigenvalues of the error reduction matrix are positive and less than or equal to one, i.e. $\alpha \in [0,1]$. Hence the proposed iteration scheme will show monotonous local convergence for associated plasticity. In reference (26) it is proved that the method even involves global convergence, i.e.

convergence independent of step size. In the case of non-associated plasticity we can give no such proof. However, experience based on analyses of many non-associated plasticity problems shows that the initial stiffness method performs reasonably well. It is only for large step sizes and/or overrelaxation that we experienced divergence. Whereas overrelaxation appears to be highly efficient in associated plasticity, it appears to be of little help in non-associated plasticity. In the latter case it may even destroy the convergence properties. To clarify this empirical finding, overrelaxation will now be considered in more detail.

Let us suppose that we have the special case in which the method without overrelaxation also converges for non-associated plasticity. In this case it is possible to study the influence of overrelaxation on the convergence properties. If we assume that $\bar{\alpha}$ is an eigenvalue for $\omega = 1$, then it follows from definition (3.14) of matrix $\underline{\underline{A}}$ that

$$\alpha = 1 - \omega + \omega \bar{\alpha} \tag{3.42}$$

Figure (3.2) gives a graphical representation of the above formula. From this figure it follows amongst others that

$$|\alpha| \in [0,1) \text{ for } \omega \in (0,2] \quad \text{and} \quad \bar{\alpha} \in [0,1) \tag{3.43}$$

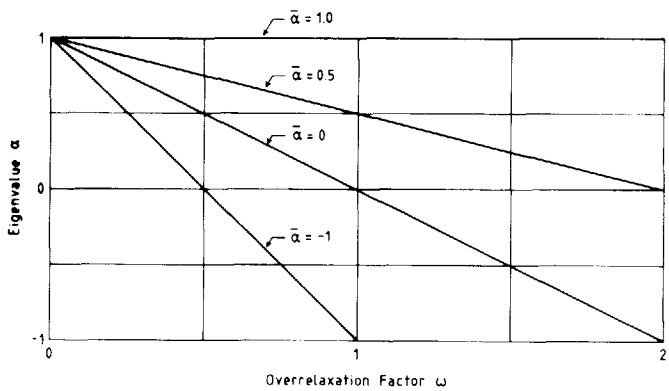

Figure 3.2. Eigenvalue α of the error reduction matrix against overrelaxation factor ω ; $\bar{\alpha}$ is eigenvalue for $\omega = 1$.

Hence the procedure preserves convergence when choosing overrelaxation factors in the well-known range between zero and two. However, this only holds true for positive values of the basic eigenvalue $\bar{\alpha}$, as induced by associated plasticity. For non-associated plasticity $\bar{\alpha}$ is not necessarily positive. In such situations overrelaxation with $1<\omega<2$ might destroy the convergence. The conclusion must be that overrelaxation is not advisable for non-associated plasticity. Another conclusion following from Figure (3.2) is that for associated plasticity problems choosing values for $\omega\in(0,1]$ will reduce the convergence speed, whereas $\omega\in(1,2]$ may increase the speed. For near elastic response, sub-incremental matrix $\underline{\underline{S}}$ will not differ much from elasticity matrix $\underline{\underline{K}}_e$, so that the error reduction matrix $\underline{\underline{A}}$ nearly vanishes. Hence, all eigenvalues $\bar{\alpha}$ will be approximately equal to zero and overrelaxation will slow down convergence. As plasticity develops, some eigenvalues $\bar{\alpha}$ will increase and become decisive for the convergence speed. This is where overrelaxation becomes beneficial as it reduces the largest eigenvalue.

3.6 Examples

The application of the step size correction scheme will be demonstrated by considering three problems of soil-structure interaction involving collapse. Here, no large deformation effects will be considered. Typical differences between analyses of associated and non-associated plasticity problems become evident.

3.6.1. Non-associated Mohr-Coulomb plasticity model

The examples of this chapter all concern the computation of accurate collapse loads for soil bodies. As a consequence we need a model which is accurate in the fully plastic range rather than at pre-failure working loads. For that reason the perfectly plastic Mohr-Coulomb model[15] is used, at least for the problems considered in this section.

The global yield function of the Mohr-Coulomb model consists of three regular functions. In terms of the principal stresses these functions may be

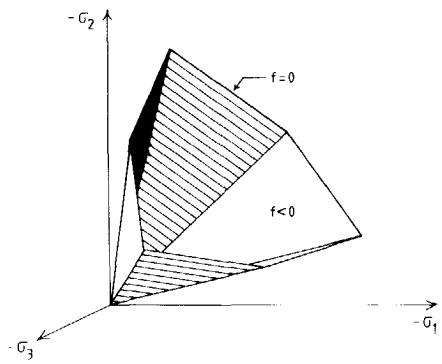

Figure 3.3. Mohr-Coulomb yield surface in principal stress space.

formulated as:

$$\begin{aligned} f_1 &= \frac{1}{2}\,|\sigma_2-\sigma_3| + \frac{1}{2}(\sigma_2+\sigma_3)\,\sin\Phi - c\,\cos\Phi \le 0 \\ f_2 &= \frac{1}{2}\,|\sigma_3-\sigma_1| + \frac{1}{2}(\sigma_3+\sigma_1)\,\sin\Phi - c\,\cos\Phi \le 0 \\ f_3 &= \frac{1}{2}\,|\sigma_1-\sigma_2| + \frac{1}{2}(\sigma_1+\sigma_2)\,\sin\Phi - c\,\cos\Phi \le 0 \end{aligned} \tag{3.44}$$

Here Φ denotes the friction angle of the granular material and c is the cohesive strength. Figure (3.3) shows the full angular Mohr-Coulomb surface in three-dimensional principal stress space. In the special case of a frictionless material the yield surface reduces to the well-known Tresca polygon.

Like the yield function, the global plastic potential function consists of three different functions:

$$\begin{aligned} g_1 &= \frac{1}{2}\,|\sigma_2-\sigma_3| + \frac{1}{2}(\sigma_2+\sigma_3)\,\sin\Psi \\ g_2 &= \frac{1}{2}\,|\sigma_3-\sigma_1| + \frac{1}{2}(\sigma_3+\sigma_1)\,\sin\Psi \\ g_3 &= \frac{1}{2}\,|\sigma_1-\sigma_2| + \frac{1}{2}(\sigma_1+\sigma_2)\,\sin\Psi \end{aligned} \tag{3.45}$$

Here, Ψ denotes the so-called angle of dilatancy. In the special case of $\Psi = \Phi$, the model becomes associated. The constitutive relation for the Mohr-Coulomb

model can be derived by following the method set out in section (2.5).

3.6.2. Rigid footing on a purely cohesive soil

A finite element program named PLAXIS is used to give some examples of the capabilities of the step size procedure. This program uses high-order 15-noded finite elements. These elements prove to yield accurate results for axi-symmetric deformation of virtually incompressible soils[31,32]. For a plane strain problem, like the one considered here, high-order elements tend to give smoother stress distributions than low-order elements.

Figure (3.4) shows the finite element mesh for the indentation problem of a strip footing on a soil having increasing cohesion with depth, and no friction. It is an associated plasticity problem. The material properties are as follows

shear modulus	G = 150 kPa
Poisson's ratio	ν = 0.49
friction angle	$\Phi = 0^{\circ}$
dilation angle	$\Psi = 0^{\circ}$
cohesion	c = 1- 2 kPa

Note that there is no uniform distribution of the cohesion, but that it increases with depth.

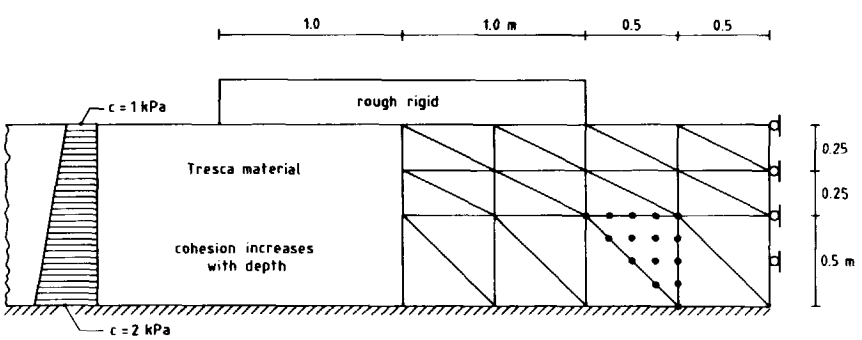

Figure 3.4. Finite element mesh for a rough strip footing on a cohesive stratum.

The computations for the footing indentation problem were carried out using the automatic scheme discussed in section 3.3.2, taking the following input values for the number of iterations per step:

desired minimum	$K_{min} = 4$
desired maximum	$K_{max} = 10$

After each scaling action the desired maximum number of iterations needs to be increased, as a step size change requires some extra iterations. For the present example we allow for 5 extra iterations after each scaling action. For the present computation the convergence tolerance was taken to be 5 per cent for the out-of-balance error. The out-of-solution error was not used as a control parameter, but only as an output quantity.

The first displacement increment of the footing is chosen in such a way that only one Gauss point enters a plastic state. As can be seen from the load-displacement curve, Figure (3.5), several scaling actions have been performed in subsequent steps. The step size is doubled during the second step and it is halved twice during the fourth step. Then step sizes are doubled in steps 11, 15, 16 and 19. In this calculation the average number of iterations per step is six. Hence the iterative procedure appears to be fast.

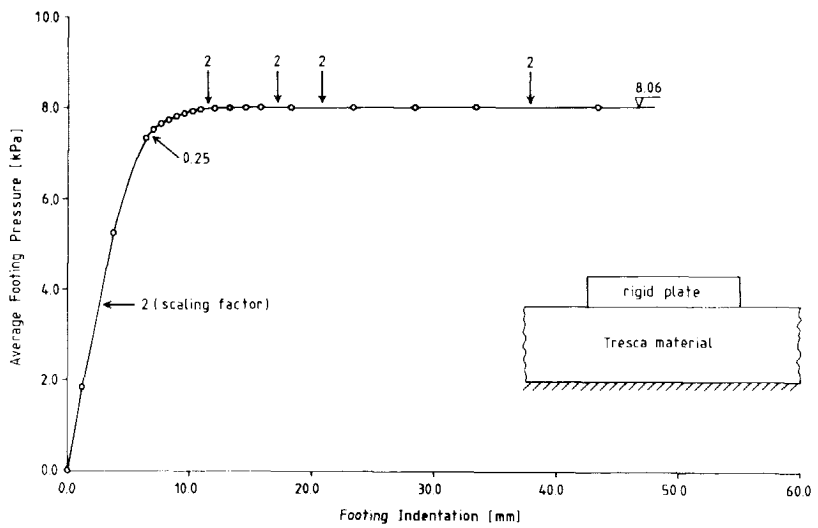

Figure 3.5. Load-displacement curve for footing on a cohesive stratum.

The value of the out-of-solution error may now be used to estimate the numerical accuracy of the load displacement curve. This error showed a value in the order of 8 per cent, which is regarded as being sufficiently close to the preset tolerance of 5 per cent. Experience shows that this is a general trend for problems of cohesion plasticity. The two error measures do not deviate considerably for such computations.

From Figure (3.5) it follows that there is a slight overshoot of the limit load. The analytical solution given by Davis and Booker[33] is 7.67 kPa, which is slightly below the numerical value of 8.06 kPa. If we observe the incremental displacement field at failure, Figure (3.6), the cause of the overshoot becomes evident. Just underneath the rough footing a zone with a very high horizontal displacement gradient has developed. This indicates the presence of a narrow shear band in the theoretical solution. Hence the numerical limit load will depend on the fineness of the mesh just below the footing.

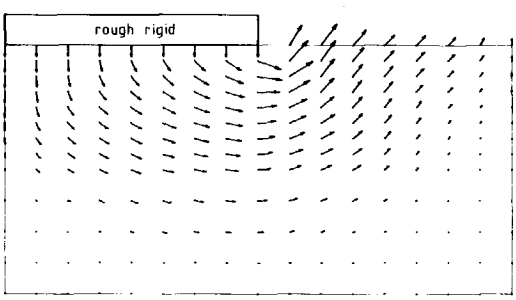

Figure 3.6. Incremental displacement field at failure for rough footing on a cohesive stratum.

Table (3.1) shows the relation between the Rayleigh quotient of equation (3.16) and the iteration number in step 3 of the automatic calculation. As can be seen from this table, the quotient becomes more or less constant after only three iterations. Such results justify the linearizations made in the theoretical developments of the previous sections.

The calculation was also done using manual control. In this case step sizes were kept constant, and equal to the initial one. For this problem of

associated plasticity, manual control required about the same total number of iterations. For non-associated plasticity, however, the step size is much more critical and significant differences occur, as will be shown by two other examples.

Table 3.1. The change of the Rayleigh quotient, equation (3.16) during the iteration process in step 3 of the footing on cohesive soil.

Iteration	Rayleigh quotient
2	0.597
3	0.707
4	0.741
5	0.812
6	0.762
7	0.810
8	0.747
9	0.810
10	0.791

3.6.3. Shallow cone penetration in purely frictional soil

Figure (3.7) shows the deformed finite element mesh for the axi-symmetric problem of a smooth rigid cone penetrating in purely frictional soil. In fact we consider a dense sand which is dilatant and highly frictional. The properties are as follows:

$$G = 10000 \text{ kPa} \ , \ \nu = 0.3 \ , \ \gamma = 16 \text{ kN/m}^3$$
$$c = 0 \ , \ \Phi = 40^\circ \ , \ \psi = 10^\circ \ , \ K_0 = 0.5$$

in which γ denotes the volumetric weight of the material and K_0 the ratio of the initial stresses due to soil weight.

This highly frictional non-associated problem proves to be difficult to solve by a manually controlled calculation. As there is no initial shear strength at the soil surface, the absence of cohesion dictates small step sizes at the beginning of loading. Shear strength is gradually built up together with the increase of normal stresses. Hereafter larger step sizes will be needed to prevent endless computation. Finally, in the fully plastic

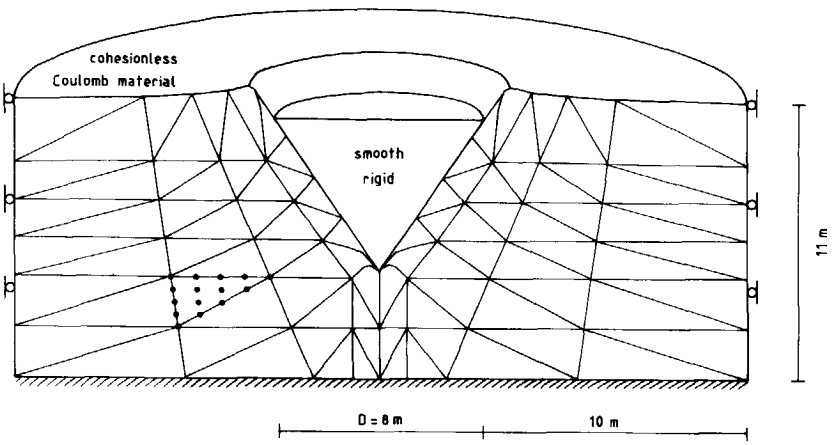

Figure 3.7. Deformed mesh at failure for cone penetration in a purely frictional soil.

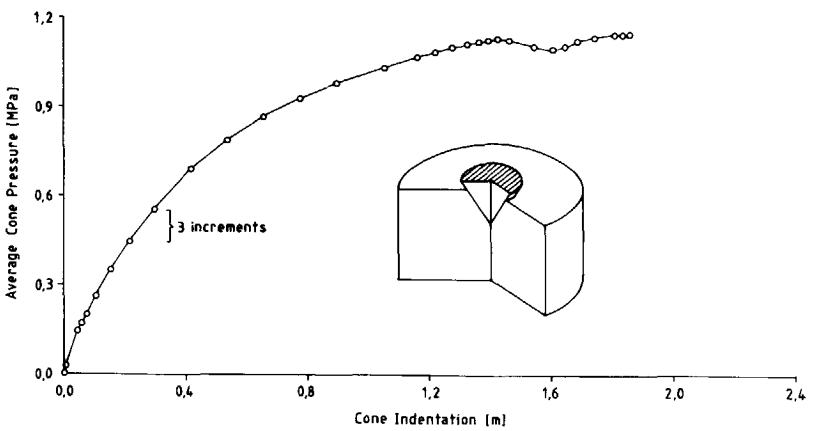

Figure 3.8. Load-displacement curve for cone penetration in cohesionless material.

range, the step size must be decreased again to prevent divergence of the iterative process.

Figure (3.8) shows the load displacement curve as obtained using the automatic step size correction procedure. The out-of-balance convergence tolerance was preset at 5 per cent. The input values for the step size procedure are the same as used in the previous section. It can be seen from this figure that at the beginning of loading small displacement increments are applied. In the middle part of the curve step sizes are considerably larger. Near failure, step sizes are reduced again.

The out-of-solution error varied substantially. At the end of each step, when the out-of-balance error had decreased to below 5 per cent, the out-of-solution error appeared to be in the order of 10 to 15 per cent. However, at failure the accuracy was better with an out-of-solution error in the order of 8 per cent. This agrees well with the obtained accuracy in the first example.

3.6.4. Rigid footing on purely frictional soil

As in the first, example we again consider a strip footing problem, but now for cohesionless soil and taking account of self weight. For a rough footing the collapse load is approximately known from Terzaghi's bearing capacity equation[34]. However, no analytical solution exists for a smooth footing. Similarly we are not aware of any finite element solutions for the limit load. Here we consider such a smooth footing problem with the following properties:

$$G = 50000 \text{ kPa} \ , \ \nu = 0.3 \ , \ \gamma = 16 \text{ kN/m}^3$$
$$c = 0 \ , \ \Phi = 30^\circ \ , \ \Psi = 0^\circ \ , \ K_0 = 1$$

The finite element mesh for this problem is shown in Figure (3.9).

This problem proved to be difficult to solve as divergence was experienced when step sizes were selected manually. Computations with automatic step size corrections were more successful. Figure (3.10) shows the computed load displacement curve. The step size control parameters were taken as in the previous examples, including an out-of-balance tolerance of 5 per cent. Initially this leads to very small step sizes, but later on larger steps are feasible.

The post-peak response visible in Figure (3.10) may cause some concern. It

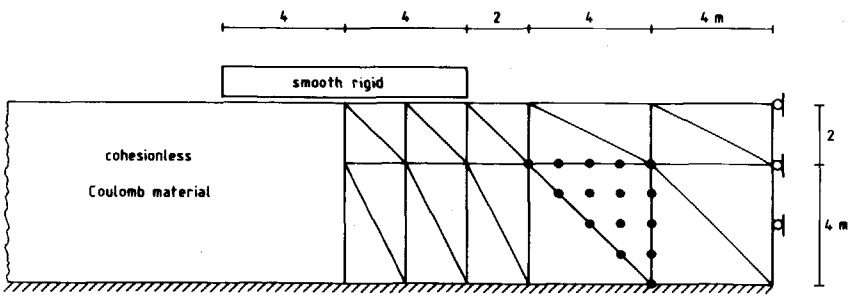

Figure 3.9. Finite element mesh for a smooth footing on purely frictional soil.

shows a heavy oscillation which damps out as the calculation progresses. The oscillations violate the obtained limit value of the load by 10 per cent. Hence for this particular problem a tolerance on the out-of-balance error yields inaccurate results. This conclusion is supported by the values of the out-of-solution error at the predicted peaks and troughs. At the first peak the out-of-solution measure predicts a 79 per cent error and at the first

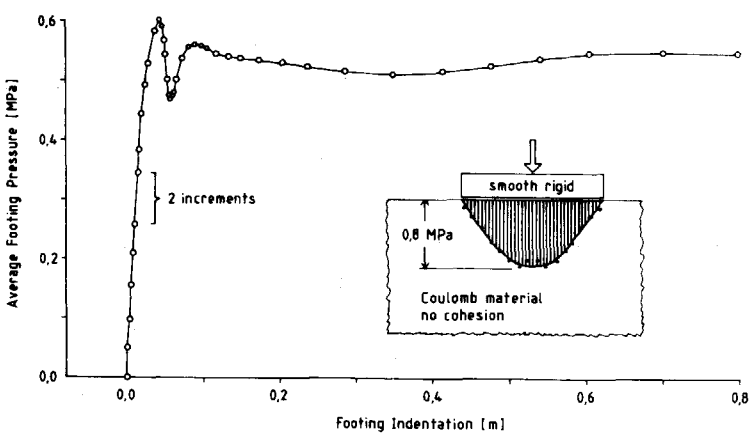

Figure 3.10. Load-displacement curve for a smooth footing on cohesionless material.

trough a value of 25 per cent is recorded. On the other hand, the final limit load turns out to be fairly accurate, as it shows an out-of-solution error of 8 per cent, which is in fact as accurate as the limit load obtained in the first example on cohesive soil.

At collapse the average footing pressure amounts to 545 kPa which compares well to data by Gussmann[35]. The latter solved this particular problem by an upper-bound technique to find a limiting pressure of 576 kPa.

The final collapse mechanism is shown in Figure (3.11). This mechanism differs considerably from the well-known Prandtl-type slip line fields for footings with cohesive resistance or resistance resulting from a surcharge on the soil surface. Similarly the computed pressures at the footing are not uniform at all as suggested by Prandtl-type solutions. The computed distribution is parabolic as indicated in the insert to Figure (3.10). This result is in line with a semi-analytical solution by Sokolovskii[36] for ponderable soil with little cohesion. Note that there is no analytical solution for completely cohesionless soil as considered here, so that a quantitative validation is impossible.

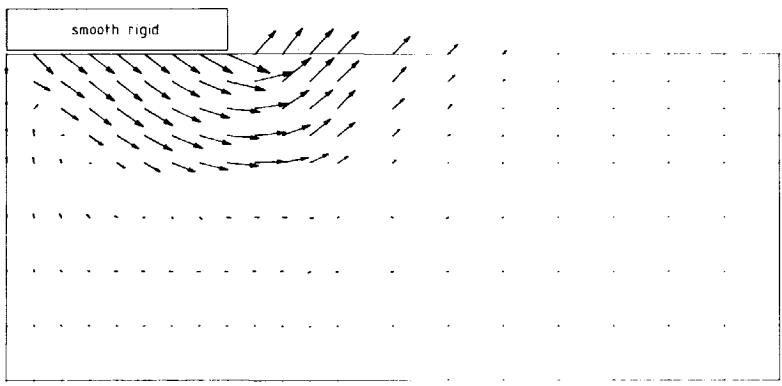

Figure 3.11. Failure mechanism for a smooth footing on cohesionless soil.

APPENDIX B

In this appendix some general properties of the elastic stiffness matrix $\underline{\underline{K}}_e$ and the sub-incremental stiffness matrix $\underline{\underline{S}}$ are derived. Bounds on the parameter α_m, which appears in the error reduction equation (3.15), are given for the case where the initial stiffness method is applied to problems of small strain associated plasticity.

To deduce the properties of the initial stiffness method, some general theorems of plasticity need to be introduced. Associated plasticity models adhere to the condition

$$(\underline{\sigma} - \underline{\sigma}^*)^T \dot{\underline{\varepsilon}}^p \geq 0 \tag{B1}$$

being named stability in the large by Drucker[26,37]. Here, $\underline{\sigma}$ is a state of stress on the yield surface with the associated plastic strain rate $\dot{\underline{\varepsilon}}^p$. The stress $\underline{\sigma}^*$ may represent any admissible stress at or inside the yield surface. Hence

$$f(\underline{\sigma}) = 0 \quad ; \quad f(\underline{\sigma}^*) \leq 0 \tag{B2}$$

In finite element computations we use finite strain increments $\Delta\underline{\varepsilon}$ rather than rates of strain. These finite strain increments are obtained by integrating strain rates over a loading step. In this study the implicit integration scheme is used. This method will be described in section 5.4 where it is used for the integration of a constitutive model for sand. It is shown in reference (26) that in the case of implicit integration Drucker's postulate applies to the total plastic strain increment for a loading step, i.e.

$$(\underline{\sigma} - \underline{\sigma}^*)^T \Delta\underline{\varepsilon}^p \geq 0 \tag{B3}$$

where $\underline{\sigma}$ is on the yield surface and $\Delta\underline{\varepsilon}^p$ is the associated plastic strain increment. We may now write for two subsequent iterations

$$(\underline{\sigma}_k - \underline{\sigma}^*)^T \Delta\underline{\varepsilon}_k^p \geq 0 \; ; \; (\underline{\sigma}_{k-1} - \underline{\sigma}^*)^T \Delta\underline{\varepsilon}_{k-1}^p \geq 0 \tag{B4}$$

or by choosing $\underline{\sigma}^* = \underline{\sigma}_{k-1}$ and $\underline{\sigma}^* = \underline{\sigma}_k$ respectively

$$(\underline{\sigma}_k - \underline{\sigma}_{k-1})^T \Delta\underline{\varepsilon}_k^p \geq 0 \; ; \; (\underline{\sigma}_{k-1} - \underline{\sigma}_k)^T \Delta\underline{\varepsilon}_{k-1}^p \geq 0 \tag{B5}$$

If we add these relations together, it is found that

$$\delta\underline{\sigma}^T\delta\underline{\varepsilon}^p = (\delta\underline{\varepsilon}^e)^T\underline{\underline{D}}^e\delta\underline{\varepsilon}^p \geq 0 \tag{B6}$$

where $\underline{\underline{D}}^e$ is the elasticity matrix and

$$\delta\underline{\sigma} \equiv \underline{\sigma}_k - \underline{\sigma}_{k-1} \quad ; \quad \delta\underline{\varepsilon}^p \equiv \Delta\underline{\varepsilon}^p_k - \Delta\underline{\varepsilon}^p_{k-1} \tag{B7}$$

Equation (B6) can be transformed into

$$(\delta\underline{\varepsilon}^e)^T\underline{\underline{D}}^e\delta\underline{\varepsilon}^p + (\delta\underline{\varepsilon}^p)^T\underline{\underline{D}}^e\delta\underline{\varepsilon}^p - \delta\underline{\varepsilon}^T\underline{\underline{D}}^e\delta\underline{\varepsilon} \geq -\delta\underline{\varepsilon}^T\underline{\underline{D}}^e\delta\underline{\varepsilon} \tag{B8}$$

The validity of this equation follows from the fact that the second term will always be positive, for matrix $\underline{\underline{D}}^e$ is positive definite, and the third term on the left hand side is simply equal to the term on the right hand side. The first two terms of equation (B8) can be combined to obtain

$$\delta\underline{\varepsilon}^T\underline{\underline{D}}^e\delta\underline{\varepsilon}^p - \delta\underline{\varepsilon}^T\underline{\underline{D}}^e\delta\underline{\varepsilon} \geq -\delta\underline{\varepsilon}^T\underline{\underline{D}}^e\delta\underline{\varepsilon} \tag{B9}$$

Now by making the substitutions

$$\underline{\underline{D}}^e(\delta\underline{\varepsilon}^p - \delta\underline{\varepsilon}) = \underline{\underline{D}}^e\delta\underline{\varepsilon}^e = \delta\underline{\sigma} \tag{B10}$$

equation (B9) will obtain the form

$$\delta\underline{\varepsilon}^T\delta\underline{\sigma} \leq \delta\underline{\varepsilon}^T\underline{\underline{D}}^e\delta\underline{\varepsilon} \tag{B11}$$

For associated plasticity, we have another inequality, namely

$$\delta\underline{\varepsilon}^T\delta\underline{\sigma} \geq 0 \tag{B12}$$

Both inequalities may be combined in the expression

$$0 \leq \delta\underline{\varepsilon}^T\underline{\underline{M}}\,\delta\underline{\varepsilon} \leq \delta\underline{\varepsilon}^T\underline{\underline{D}}^e\delta\underline{\varepsilon} \tag{B13}$$

where

$$\underline{\underline{M}}\,\delta\underline{\varepsilon} = \delta\underline{\sigma} \tag{B14}$$

Equation (B13) can be transformed into an equation for sub-increments of nodal forces and nodal displacements by integrating over the volume of the body.

This gives

$$0 \leq \int_V \delta\underline{\varepsilon}^T \underline{\underline{M}}\, \delta\underline{\varepsilon}\, dV \leq \int_V \delta\underline{\varepsilon}^T \underline{\underline{D}}^e \delta\underline{\varepsilon}\, dV \tag{B15}$$

This relation can be discretized by introducing finite element shape functions (2.83)

$$0 \leq \delta\underline{a}^T \underline{\underline{S}}\, \delta\underline{a} \leq \delta\underline{a}^T \underline{\underline{K}}_e \delta\underline{a} \tag{B16}$$

in which matrix $\underline{\underline{S}}$ represents the secant matrix for sub-increments.

Having obtained equation (B16), based on the general principles of plasticity, we can now focus attention on the eigenvalues of matrix $\underline{\underline{A}}$

$$\underline{\underline{A}} = (\underline{\underline{I}} - \underline{\underline{S}}\, \underline{\underline{K}}_e^{-1}) \tag{B17}$$

as used in the error reduction equation (3.14). However, it will first be shown that equation (B16) provides bounds for the eigenvalues of the closely related matrix $\underline{\underline{A}}^*$

$$\underline{\underline{A}}^* = (\underline{\underline{I}} - \underline{\underline{K}}_e^{-1} \underline{\underline{S}}) \tag{B18}$$

The eigenvalues α_i^* of this matrix are roots of the equation

$$\underline{\underline{A}}^* \underline{w}_i = \alpha_i^* \underline{w}_i \tag{B19}$$

It can now be derived, by pre-multiplying both sides of this equation by $\underline{w}^T$, that the eigenvalues α^* relate to the eigenvectors $\underline{w}$ as

$$(1 - \alpha_i^*) = \frac{\underline{w}_i^T \underline{\underline{S}}\, \underline{w}_i}{\underline{w}_i^T \underline{\underline{K}}_e \underline{w}_i} \tag{B20}$$

Equation (B16) holds for any vector $\delta\underline{a}$, so we may replace $\delta\underline{a}$ by the eigenvector $\underline{w}_i$, yielding for equation (B16)

$$0 \leq \underline{w}_i^T \underline{\underline{S}}\, \underline{w}_i \leq \underline{w}_i^T \underline{\underline{K}}_e \underline{w}_i \tag{B21}$$

Combining equations (B20) and (B21) gives the following bounds for all eigenvalues α_i^*

$$0 \leq \alpha_i^* \leq 1 \tag{B22}$$

These bounds hold for the eigenvalues of matrix $\underline{\underline{A}}^*$.

To obtain bounds for the eigenvalues of matrix $\underline{\underline{A}}$ we need to discuss the relationship between eigenvectors and eigenvalues of these two matrices. Matrices $\underline{\underline{A}}$ and $\underline{\underline{A}}^*$ can be related to each other by the equation

$$\underline{\underline{A}}^* = \underline{\underline{K}}_e^{-1} \underline{\underline{A}} \underline{\underline{K}}_e \tag{B23}$$

Substituting this expression into equation (B19), it is found that

$$\underline{\underline{K}}_e^{-1} \underline{\underline{A}} \underline{\underline{K}}_e \underline{w}_i = \alpha_i^* \underline{w}_i \tag{B24}$$

Multiplying both sides by $\underline{\underline{K}}_e$ yields

$$\underline{\underline{A}} \underline{v}_i = \alpha_i^* \underline{v}_i \quad ; \quad \underline{v}_i \equiv \underline{\underline{K}}_e \underline{w}_i \tag{B25}$$

Evidently $\underline{v}_i$ is an eigenvector of matrix $\underline{\underline{A}}$ and α_i^* is the associated eigenvalue. This shows that the eigenvalues of matrices $\underline{\underline{A}}$ and $\underline{\underline{A}}^*$ coincide. Hence, the bounds given by the inequalities (B22) for the eigenvalues α_i^* also apply to the eigenvalues of matrix $\underline{\underline{A}}$.

$$0 \leq \alpha_i \leq 1 \tag{B26}$$

It should be borne in mind that the above result applies for associated plasticity with implicit integration of the differential constitutive model.

To clarify the obtained result we can look at a fictitious one-dimensional system. In such a case matrices $\underline{\underline{K}}_e$ and $\underline{\underline{S}}$ degenerate to the scalars K and S respectively, which represent the initial elastic slope and subsequent elasto-plastic slopes of the load displacement graph of this system. For associated plasticity K and S are positive and $\alpha = 1 - \beta$, where β is the ratio of S over K; it is a relative current stiffness parameter. In this case the limiting values for S are: S = K for elastic behaviour and S = 0 for the fully plastic range. As a result β is in the range between zero and one; this means that α is positive. For non-associated plasticity we may have situations with $\beta<0$, a kind of softening, or even $\beta>1$, which means stiffening.

4. APPLICATION OF INTERFACE ELEMENTS

This chapter discusses the application of interface elements in the analysis of soil-structure interaction. Such interface elements are used to model the contact zone between the structure and the soil. For this purpose, a 10-noded finite element is formulated and its numerical integration is discussed.

Many problems of soil-structure interaction involve special points where the deformation field can become singular, one example being the flow of soil around a corner. A conventional finite element mesh lacks the flexibility to model this phenomenon. Consequently, finite elements are distorted to an extreme extent, thus yielding non-physical stress results. A solution to this problem is presented in section 4.4, where a special use of interface elements is advocated. Three problems of soil-structure interaction, all involving points of singular deformation, are discussed. Special attention will be given to the quality of stress results and limit loads.

4.1 Interface elements in soil-structure interaction

In the analysis of soil-structure interaction, the development of displacement singularities and zones of high distortion requires particular attention. Special finite elements can be used to model these zones. The first use of such interface elements or joint elements[38-41] was made in the analysis of rock masses with predefined joints. Later, interface elements were also applied to the problem of soil-structure interaction[42-52]. Independently from this, the analysis of concrete fracture led to the development of lumped interface elements, in which the contacting faces are coupled by node-to-node spring boxes[53,54].

Roughly speaking, two approaches may be found in the literature. One approach[42-47] is to treat the interface as a direct problem of compatibility. Compatibility requirements are enforced exactly, for example by means of Lagrangian multipliers, or approximately by means of a penalty formulation. The second approach (references 38-41,48-52) uses the physical concept of an interface element. Here, a constitutive equation relates contact stresses to slip and compression. From a mathematical point of view, this approach and the penalty approach coincide. A detailed description of interface formulations is

given by Hohberg[55]. The second approach will be chosen in this study. An interface element can easily be incorporated in a multi-purpose finite element program without the need for special features like the introduction of Lagrangian multipliers or the need to update the kinematic constraints.

4.2 Formulation of an interface element

4.2.1. Constitutive relation

The constitutive equation for the interface behaviour will be based on expression (2.73),

$$\underset{\sim}{\overset{\circ}{t}} = \underline{\underline{D}}^{e}_{c}\, \Delta\underset{\sim}{\dot{u}}^{e} = \underline{\underline{D}}^{e}_{c}(\Delta\underset{\sim}{\dot{u}} - \Delta\underset{\sim}{\dot{u}}^{p}) \tag{4.1}$$

which relates an objective rate of traction, $\underset{\sim}{\overset{\circ}{t}}$, to the relative displacement across an interface surface, $\Delta\underset{\sim}{\dot{u}}^{e}$. For matrix $\underline{\underline{D}}^{e}_{c}$ the following simple expression is chosen

$$\underline{\underline{D}}^{e}_{c} = \begin{bmatrix} k_s & 0 \\ 0 & k_n \end{bmatrix} \tag{4.2}$$

Note that the elastoplastic stiffness matrix, which is derived from further development of equation (4.1), will generally contain off-diagonal terms. For computations in the fully plastic range the definition of the D-matrix is basically not very important. Here, the elastic slip becomes negligibly small and, as a result, $\underset{\sim}{\dot{t}}_{c}$ vanishes. Boulon[8] presents an incrementally non-linear constitutive model, which can be used to give a more accurate prediction of interface behaviour in the pre-failure range.

Interface stiffnesses k_s and k_n should be chosen such that the initial slopes of load-displacement curves closely resemble those which are obtained without the use of interfaces. In this way, the influence of interfaces is limited to the case of true plastic slip, where it enhances the flexibility of the model. Upper bounds to the values of k_s and k_n are determined by possible ill-conditioning of the stiffness matrix. Presently, we are relating interface stiffnesses to the mean element length l, the shear modulus of the soil G and

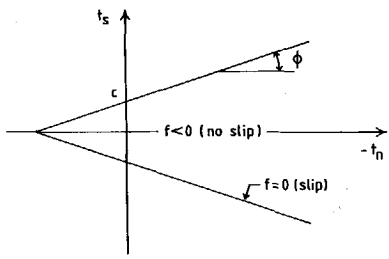

Figure 4.1. Coulomb yield locus for an interface element.

Poisson's ration ν, in the following way

$$k_s = \mu \frac{G}{l} \quad ; \quad k_n = \mu \frac{G}{(1-2\nu)l} \tag{4.3}$$

For the present calculations we used μ=50. However, suitable values for k_s and k_n are difficult to choose in advance and, as a result, the elastic solution should be checked with the above considerations in mind.

In the present study we consider only a simple Mohr-Coulomb yield function as depicted in Figure (4.1)

$$f(\underline{t}) = |t_s| + t_n \tan\phi_i - c_i \tag{4.4}$$

It involves the contact pressure t_n and the shear stress t_s. Parameters ϕ_i and c_i are the interface friction angle and adhesion. The plastic part of the relative displacement across an interface surface, $\Delta\underline{\dot{u}}^p$, becomes non-zero when the increase of traction is such that

$$f(\underline{t}) = 0 \qquad \text{and} \qquad \frac{\partial f}{\partial \underline{t}}^T \underline{\underline{D}}_c^e \Delta\underline{\dot{u}} \geq 0 \tag{4.5}$$

The rate of plastic slip is derived from the plastic potential function g,

$$g(\underline{t}) = |t_s| + t_n \tan\psi_i \tag{4.6}$$

which contains the dilation angle ψ_i. The use of a non-associated flow rule with $\psi_i < \phi_i$ prevents the over-prediction of plastic dilation. In confined problems this would yield an over-estimation of contact pressures and thus of

the shear strength.

The relation between the plastic part of the relative displacement and the above plastic potential function is given by

$$\dot{\Delta u}^{p} = \dot{\lambda} \frac{\partial g}{\partial t} \tag{4.7}$$

The multiplier $\dot{\lambda}$ can be solved from the consistency condition $\dot{f} = 0$, which after some elaboration yields

$$\dot{\lambda} = \frac{1}{d} \frac{\partial f}{\partial t}^{T} \underline{\underline{D}}_{c}^{e} \dot{\Delta u} \quad ; \quad d = \frac{\partial f}{\partial t}^{T} \underline{\underline{D}}_{c}^{e} \frac{\partial g}{\partial t} \tag{4.8}$$

The incremental constitutive relation is obtained by combining expressions (4.1) to (4.8)

$$\overset{\circ}{t} = \underline{\underline{D}}_{c}^{ep} \dot{\Delta u} \tag{4.9}$$

where for positive values of t_s

$$\underline{\underline{D}}_{c}^{ep} = \frac{k_s k_n}{d} \begin{bmatrix} \tan\phi \tan\psi & -\tan\phi \\ -\tan\psi & 1 \end{bmatrix} \quad ; \quad d = k_s + k_n \tan\phi \tan\psi \tag{4.10}$$

For negative values of t_s the off-diagonal terms change their sign. Inspection of matrix $\underline{\underline{D}}_{c}^{ep}$ shows that for $\dot{\Delta u}_n = \dot{\Delta u}_s \tan\psi$ the increment of traction vanishes, as in fact is to be expected. For non-associated material behaviour, i.e. for $\psi \neq \phi$, this matrix becomes non-symmetric.

A relationship for finite increments of stress and strain can be obtained by integrating equation (4.9). If the stress path intersects the yield locus during a loading step, the material behaviour changes from elastic to elastoplastic. Hence, integration of equation (4.9) would incorporate the determination of this intersection. This complication is eliminated if we make use of an implicit integration scheme[56].

Upon integration, equation (4.1) becomes

$$\Delta t = \underline{\underline{D}}_{c}^{e} (\Delta u - \Delta u^{p}) \quad ; \quad \Delta u = \int \dot{\Delta u} \, dt \tag{4.11}$$

If we now define

$$f^{e} \equiv f \left(t_{0} + \underline{\underline{D}}_{c}^{e} \Delta u \right) \tag{4.12}$$

then equation (4.8) can be simplified to

$$\dot{\lambda} = \frac{1}{d} \dot{f}^e \tag{4.13}$$

or after integration

$$\Delta\lambda = \frac{1}{d} (f^e - f_0^e) = \frac{f^e}{d} \tag{4.14}$$

As the initial stress state $\underline{t}_0$ always satisfies the condition $f(\underline{t}_0) = 0$, the term f_0^e can be deleted from this expression. When this relation for $\Delta\lambda$ is substituted in equation (4.11), we obtain

$$\Delta\underline{t} = \underline{\underline{D}}_c^e (\Delta\underline{u} - \Delta\lambda \frac{\partial g}{\partial \underline{t}}) \tag{4.15}$$

which is used to compute an increment of stress.

4.2.2. Finite element discretization

Section 2.7 discussed the finite element discretization of the equation of continued equilibrium. In the problems of this chapter no large deformation effects will be considered and, as a consequence, the tangent stiffness matrix for the interface element is completely defined by equation (2.94). For reasons given in section 3.5, the initial stiffness method is used in the numerical analysis of problems of small deformation elastoplasticity. Consequently, only the elastic stiffness matrix needs to be derived.

Figure (4.2) shows the 10-noded zero-thickness element that will be used in this study. This particular element was chosen for its compatibility with 15-noded triangular elements. According to equation (2.94), the stiffness matrix of this element can be written as

$$\underline{\underline{K}}_c^e = \int_{Sc} \underline{\underline{\Delta N}}^T \underline{\underline{D}}_c^e \underline{\underline{\Delta N}} \, dS \tag{4.16}$$

where interpolation matrix $\underline{\underline{\Delta N}}$ follows from equation (2.89). This matrix

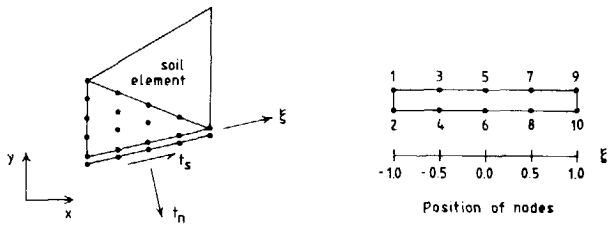

Figure 4.2. Geometry of a 10-noded interface element.

interpolates relative displacement over nodal values in the following way

$$\begin{bmatrix} \Delta u_r(\xi) \\ \Delta u_z(\xi) \end{bmatrix} = \begin{bmatrix} \Delta \underline{\underline{N}}(\xi) \end{bmatrix} \begin{bmatrix} a_{r1} \\ a_{z1} \\ \vdots \\ a_{r10} \\ a_{z10} \end{bmatrix} \tag{4.17}$$

where ξ is a local element coordinate, Figure (4.2). Interpolation matrix $\Delta \underline{\underline{N}}$ can be obtained in a straightforward manner. With the above definition of interpolation we find

$$\Delta \underline{\underline{N}} = \begin{bmatrix} N_1 & 0 & -N_1 & 0 & \cdots & N_5 & 0 & -N_5 & 0 \\ 0 & N_1 & 0 & -N_1 & \cdots & 0 & N_5 & 0 & -N_5 \end{bmatrix} \tag{4.18}$$

The shape functions N_1 to N_5 are defined as follows

$$\begin{aligned} N_1(\xi) &= \tfrac{2}{3}(\xi + \tfrac{1}{2})\,\xi\,(\xi - \tfrac{1}{2})\,(\xi - 1) \\ N_2(\xi) &= -\tfrac{8}{3}(\xi + 1)\,\xi\,(\xi - \tfrac{1}{2})\,(\xi - 1) \\ N_3(\xi) &= 4\,(\xi + 1)\,(\xi + \tfrac{1}{2})\,(\xi - \tfrac{1}{2})\,(\xi - 1) \\ N_4(\xi) &= -\tfrac{8}{3}(\xi + 1)\,(\xi + \tfrac{1}{2})\,\xi\,(\xi - 1) \\ N_5(\xi) &= \tfrac{2}{3}(\xi + 1)\,(\xi + \tfrac{1}{2})\,\xi\,(\xi - \tfrac{1}{2}) \end{aligned} \tag{4.19}$$

Element stiffness matrix (4.16) can now be elaborated for the case of

axi-symmetry

$$\underline{\underline{K}}_c^e = 2\pi \int_\xi \underline{\underline{\Delta N}}^T \, \underline{\underline{D}}_c^e \, \underline{\underline{\Delta N}} \; r \; J \; d\xi \tag{4.20}$$

where r is the radial coordinate and J is the Jacobian of the transformation from global to local coordinates

$$J = \sqrt{\left(\frac{\partial r}{\partial \xi}\right)^2 + \left(\frac{\partial z}{\partial \xi}\right)^2} = \frac{1}{2} L \tag{4.21}$$

For a straight element, this Jacobian reduces to half of the element length.

It should be noted that, due to definition (4.17), matrix $\underline{\underline{D}}_c^e$ relates global components of traction to global components of relative displacement

$$\underline{\underline{D}}_c^e = \begin{bmatrix} k_s n_r^2 + k_n n_z^2 & k_s n_r n_z - k_n n_r n_z \\ k_s n_r n_z - k_n n_r n_z & k_s n_z^2 + k_n n_r^2 \end{bmatrix} \tag{4.22}$$

Here n_r and n_z are the components of a unit vector in the direction of the interface element. An advantage of this definition is that matrix $\underline{\underline{K}}_c^e$ in equation (4.20) does not have to be transformed to global coordinates before addition to the global stiffness matrix.

In the case of plane strain conditions, the stiffness matrix reduces to

$$\underline{\underline{K}}_c^e = \int_\xi \underline{\underline{\Delta N}}^T \, \underline{\underline{D}}_c^e \, \underline{\underline{\Delta N}} \; J \; d\xi \tag{4.23}$$

4.2.3. Numerical spatial integration

For the evaluation of the element stiffness matrix and the associated load vectors some integration scheme needs to be employed. When considering straight interface elements with uniform stiffnesses, exact integration is feasible. Nevertheless, a numerical integration scheme will be employed for two reasons. First, exact integration becomes less attractive in the case of curved elements with varying stiffnesses, as encountered in the general case of soil-structure interaction. Second, exact integration proves to yield undesirable oscillations in the computed stress results. This issue will be discussed here and an improvement based on selective integration will be presented.

In the case of plane strain deformation, evaluation of the element stiffness

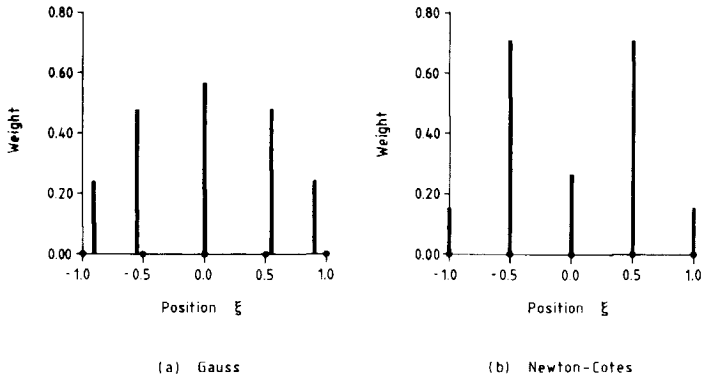

Figure 4.3. Position and weights of integration points.

matrix (4.23) involves integration of polynomials of degree 8, at least when the element is straight and the stiffness is uniform. When employing a Gauss quadrature scheme[14], exact integration up to degree 9 can be obtained by choosing 5 integration points; their positions and weights are given in Figure (4.3a).

To judge the actual performance of an interface element, a problem of elastic deformation will be considered, Figure (4.4). The theoretical solution[57] for this strip footing problem shows a stress concentration near the edge of the plate. Consequently, this problem presents a severe test for the quality of interface stresses.

The finite element mesh and material parameters for this analysis are shown in Figure (4.4). Interface elements are added along the base of the foundation. To simulate an incompressible contact, the value for k_n has been chosen in such a way that relative displacements across the interface remains within 1 per cent of the footing displacement. The value for k_s has been taken as equal to zero, thus modelling a smooth contact.

Figure (4.5a) shows the theoretical and computed contact pressures near the edge of the footing. The numerical result displays a considerable oscillation in this region. In fact, observations of this kind were made by several researchers[52,54,58] working with interface elements. In general, interface stress results prove to be poor when some stress concentration is present.

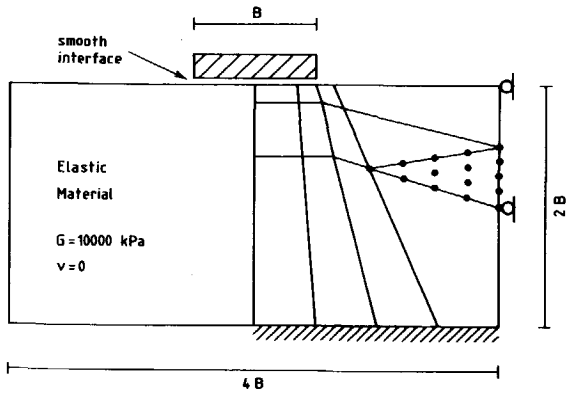

Figure 4.4. Finite element mesh and material parameters for a smooth footing on elastic sub-soil.

As shown in references (52,54,58), oscillations in stress results can be suppressed by choosing lumped interface stiffness matrices. One way of obtaining a lumped matrix is by employing a Newton-Cotes integration scheme[14], in which the integration points and weights are taken as in Figure (4.3b). An advantage over other ways of lumping is that no ad hoc definition of stress is needed and that certain compatibility requirements between interface elements and continuum elements are automatically retained. A discussion on the properties of Newton-Cotes integration is given further on in this section.

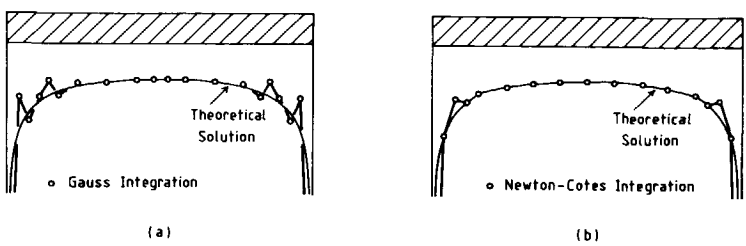

Figure 4.5 Contact pressure underneath a rigid footing on elastic sub-soil.

The stress distribution of Figure (4.5b) has been computed using a lumped interface element. It is clear from this result that oscillations are reduced considerably. In addition, stresses become continuous from one element to the next, which is in accordance with the theoretical solution. Hence from a practical point of view Newton-Cotes integration yields better results than Gauss integration. This also holds true for problems of plastic slip. Consider for example a pull-out problem as depicted in Figure (4.6). When increasing the load on the geotextile, local slip is induced in the interface. When using Gauss integration, this local disturbance propagates through the element, Figure (4.6b), whereas it is kept local with Newton-Cotes integration, Figure (4.6c).

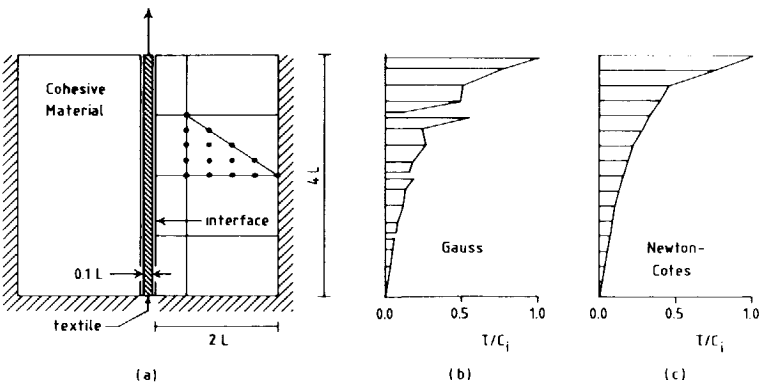

Figure 4.6. Pull-out problem (a) and shear stress results for local slip. (b) Gauss integration. (c) Newton-Cotes integration.

We will now turn to a more thorough discussion of Newton-Cotes integration and Gauss integration. First, the subject of stress transfer from the interface element to its environment and vice versa is addressed. It will be shown that for Newton-Cotes integration some oscillatory stress components are suppressed, whereas others are amplified. Second, the properties of the interface element are discussed for the case of local slip, as encountered in the above pull-out problem. This analysis sheds light on the origin of oscillatory stress results in such a case.

In the displacement based finite element method, equilibrium is obtained at the level of nodal forces. Consequently, stress transfer from the interface element to its environment and vice versa involves nodal equilibrium

$$\int_{Sc} \underline{\underline{N}}_i^T \, \underline{t}_i \, dS = \int_{Sc} \underline{\underline{N}}_e^T \, \underline{t}_e \, dS \tag{4.24}$$

where a subscript "e" denotes the environment and "i" denotes the interface element. When compatible interpolations are chosen, shape functions $\underline{\underline{N}}_i$ and $\underline{\underline{N}}_e$ coincide along boundary S. The only difference between $\underline{t}_i$ and $\underline{t}_e$ then stems from differences in integration.

Let us now consider what relation exists between $\underline{t}_i$ and $\underline{t}_e$ where the interface nodal forces follow from Newton-Cotes integration, whereas those of the environment are obtained with Gaussian integration. For this purpose, the traction $\underline{t}$ is interpolated over nodal values $\hat{\underline{t}}$

$$\underline{t}(\xi) = \underline{\underline{N}}(\xi) \, \hat{\underline{t}} \tag{4.25}$$

Substitution in equation (4.24) thus yields

$$\underline{\underline{M}}_i \, \hat{\underline{t}}_i = \underline{\underline{M}}_e \, \hat{\underline{t}}_e \tag{4.26}$$

where

$$\underline{\underline{M}} = \int_{Sc} \underline{\underline{N}}^T \underline{\underline{N}} \, dS \tag{4.27}$$

This allows for the definition of a stress transfer matrix $\underline{\underline{T}}$ in such a way that

$$\hat{\underline{t}}_i = \underline{\underline{T}} \, \hat{\underline{t}}_e \quad ; \quad \underline{\underline{T}} = \underline{\underline{M}}_i^{-1} \, \underline{\underline{M}}_e \tag{4.28}$$

When Gaussian integration is used for the interface element, matrices $\underline{\underline{M}}_i$ and $\underline{\underline{M}}_e$ become equal and, as a result, matrix $\underline{\underline{T}}$ reduces to the unity matrix. Now stress will transfer without any change. However, when Newton-Cotes integration is used, matrices $\underline{\underline{M}}_i$ and $\underline{\underline{M}}_e$ differ considerably, namely

$$\underline{\underline{M}}_i = \frac{\frac{1}{2}L}{90} \begin{bmatrix} 14 & 0 & 0 & 0 & 0 \\ 0 & 64 & 0 & 0 & 0 \\ 0 & 0 & 24 & 0 & 0 \\ 0 & 0 & 0 & 64 & 0 \\ 0 & 0 & 0 & 0 & 14 \end{bmatrix} \tag{4.29}$$

and

$$\underline{\underline{M}}_e = \frac{\frac{1}{2}L}{90} \begin{bmatrix} 9.270 & 9.397 & -5.524 & 1.778 & -0.921 \\ 9.397 & 56.889 & -12.190 & 8.127 & 1.778 \\ -5.524 & -12.190 & 59.429 & -12.190 & -5.524 \\ 1.778 & 8.127 & -12.190 & 56.889 & 9.397 \\ -0.921 & 1.778 & -5.524 & 9.397 & 9.270 \end{bmatrix} \tag{4.30}$$

For notational convenience the components of matrix $\underline{\underline{M}}_e$ have here been rounded off at the third decimal position.

To study the stress transfer properties of matrix $\underline{\underline{T}}$, the tractions $\hat{\underline{t}}_i$ and $\hat{\underline{t}}_e$ should be referred to the base of eigenvectors of matrix $\underline{\underline{T}}$

$$\hat{\underline{t}}_e = \sum_k \hat{t}_e^k \, \underline{v}_k \quad ; \quad \hat{\underline{t}}_i = \sum_k \hat{t}_i^k \, \underline{v}_k \tag{4.31}$$

Here $\underline{v}_k$ is an eigenvector of matrix $\underline{\underline{T}}$. Substitution in equation (4.28) then yields

$$\hat{t}_i^k = \lambda_k \hat{t}_e^k \tag{4.32}$$

where λ_k is the eigenvalue corresponding to vector $\underline{v}_k$. In fact, we could call λ_k an amplification factor, since it amplifies or suppresses a certain constituent of the traction.

Figure (4.7) shows the five eigenvectors of matrix $\underline{\underline{T}}$ and their corresponding eigenvalues. From this it follows that two constituents of the traction are transferred without any change, $\lambda=1$, two constituents are suppressed, $\lambda<1$, and one constituent is amplified, $\lambda>1$. It is important to note that for a linear variation of traction, compatibility between the "Newton-Cotes interface" and its "Gaussian environment" is retained. This ensures that, in the case of elasticity, mesh refinement will eventually result in convergence to the theoretical solution[13]. A second conclusion is that two types of stress oscillation are suppressed by Newton-Cotes integration, but a third type is amplified. Fortunately, the first two types are likely to be present in stress results, whereas the third type is not. This is due to the fact that abrupt changes of boundary conditions are modeled at the edge of an element.

In the example of a footing on elastic subsoil, the stress oscillation strongly resembles the eigenmode of Figure (4.7c). In terms of equation (4.31) this means that in addition to the linear components $\hat{t}_e^1$ and $\hat{t}_e^2$, the

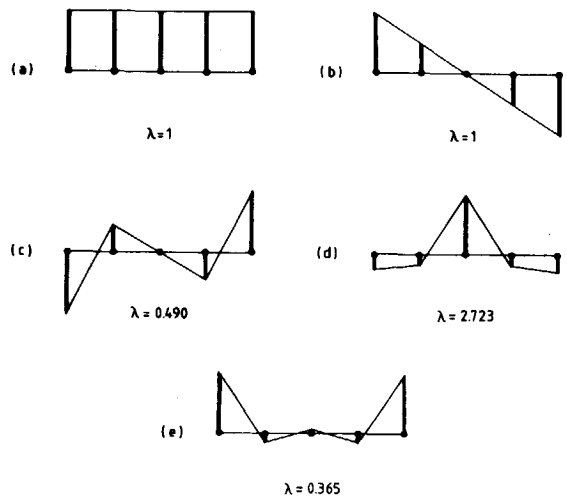

Figure 4.7. Five eigenmodes of the stress transfer matrix and associated amplification factors.

oscillatory component $\hat{t}_e^3$ dominates the traction. Consequently, in this case, Newton-Cotes integration leaves the linear components unaffected and suppresses the oscillation. This conclusion is supported by the result of Figure (4.5b).

In the pull-out example, involving local plastic slip, it was shown that also during plastic deformation stress oscillations may develop in the Gaussian interface element. To clarify this phenomenon, we need to study the stress increase in an interface element subject to local slip. Figure (4.8) shows an interface element which is embedded in a rigid continuum. Except for one nodal pair, all other pairs are prevented from slipping. However, as the displacement is derived from interpolation, the slip between the nodes is not zero. When employing Gauss integration, this distributed slip induces stress increase in all but two integration points, Figure (4.8). The first integration point behaves plastically and the centre point coincides with a nodal pair, thus both avoiding stress increase. Figure (4.8) shows that the stress in the last two integration points will decrease, as is in fact supported by the result for the pull-out problem of Figure (4.6b).

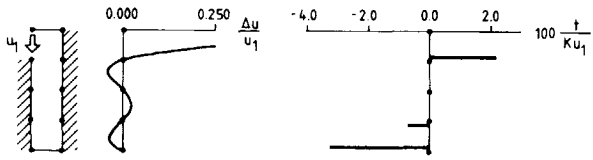

Figure 4.8. Gauss integration: stress oscillation due to local slip.

Due to the special position of Newton-Cotes integration points, local slip can be accommodated without stress increase. As a result, the quality of stresses in the pull-out problem improves substantially. Now a local disturbance induces only local change.

In reality, the continuum surrounding the interface element will not be rigid. The assumption that it is rigid can be seen as a limiting case. The other limiting case is obtained when we assume that the continuum is absent. An eigenvalue analysis of the element tangent stiffness matrix shows that in this case a mechanism will develop which is determined by the nodal slip vector $\underline{\Delta a}_s$

$$\underline{\Delta a}_s^G = \begin{bmatrix} 1.0000 \\ -0.0208 \\ 0.0000 \\ 0.0060 \\ 0.0492 \end{bmatrix} \quad ; \quad \underline{\Delta a}_s^{NC} = \begin{bmatrix} 1 \\ 0 \\ 0 \\ 0 \\ 0 \end{bmatrix} \tag{4.33}$$

where a superscript denotes the type of integration. This shows that with Newton-Cotes integration a local mechanism develops, whereas in the case of Gauss integration the mechanism involves small slip at four nodal pairs. Both displacement modes are true mechanisms in the sense that they do not involve any stress increase.

When the interface element is embedded in a deformable continuum, the mechanism in the Gaussian element will be resisted to some extent, whereas in the case of Newton-Cotes integration it may develop freely. Again this agrees with the differences observed between the results for the two kinds of integration.

The above discussions on the properties of Gauss and Newton-Cotes integration shows that the latter has some apparent advantages when used for the numerical spatial integration of the finite element. For this reason, unless explicitly stated to the contrary, Newton-Cotes integration will be used in the remainder of this study.

4.3 Rigid footing on purely cohesive soil

The contact pressure under a rigid footing on a purely cohesive soil at collapse follows from the well-known slip line solution by Prandtl[59]. The pressure is constant along the base of the footing, having a value of $(\pi+2)c$, where c is the cohesion of the material. This particular problem has been analyzed with the finite element mesh of Figure (4.9). Along the base of the footing, 10-noded interface elements are applied.

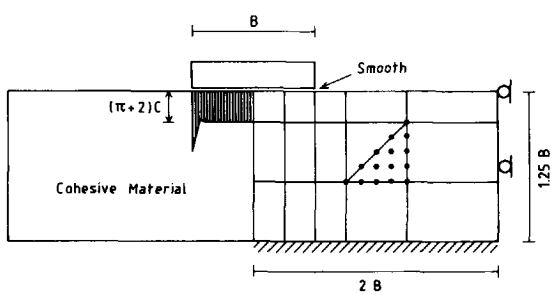

Figure 4.9. Spurious stress concentration at collapse.

Figure (4.9) shows the computed contact pressures at failure. The result obtained compares well with the theoretical solution. However, near the edge of the plate a stress concentration is visible. The reason for this overshoot becomes clear when we look at the computed velocity field at failure, Figure (4.10). The velocity field shows a strong gradient near the edge of the plate: underneath the plate the soil moves downwards, at the edge it moves sideways and to the right of the plate it moves up. Accordingly, the triangular element

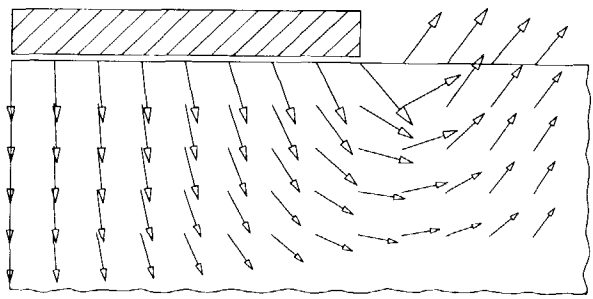

Figure 4.10. Extreme deformation at collapse near edge of footing.

at the edge of the plate is distorted to an extreme extent, thus yielding a non-physical stress concentration.

The theoretical slip line solution by Prandtl involves a so-called singular plasticity point at the edge of the plate, where the direction of the velocity field is not uniquely defined. Such singular points are likely to occur in all problems of soil-structure interaction which display a sudden change of boundary condition or involve plastic flow around corners. Consequently, this phenomenon is of general interest and will therefore be studied in more detail.

4.4 A special use of interface elements

In the remainder of this chapter we will concentrate on a very special use of interface elements to model singular plasticity points.

Singular plasticity points are best illustrated by considering problems involving perfectly plastic material. Figure (4.11) shows the slip line solution for the footing problem of the previous section. The velocity field is fully symmetric. The material between OPR slides downwards along OP and the triangle RQS slides upwards along QS. The material in the centre sectors PQR does not move as a rigid block. There is a singularity at R, the edge of the die. The singular velocity at R is plotted in Figure (4.11b); it is a fan radiating in different directions. Such a singularity cannot be modelled by a

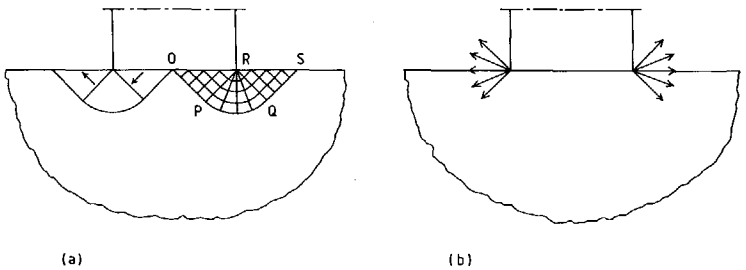

Figure 4.11. Theoretical slip line solution for a smooth die. (a) slip line field. (b) singular velocity at corner point.

conventional finite element computation which involves regular displacements for all material points. Despite this shortcoming of the conventional finite element method, it yields reasonable results for this particular problem, as was shown in the previous section.

The effects of singular plasticity points become more severe when considering buried structures in a soil mass or piercing problems in metal plasticity. A well-known problem of deep penetration is shown in Figure (4.12).

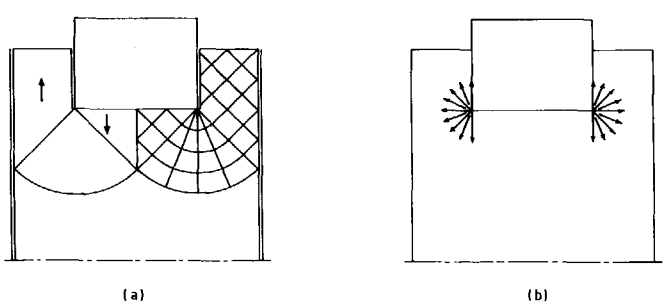

Figure 4.12. Theoretical slip line solution for a rough rigid punch penetrating into cohesive soil. (a) slip line field. (b) singular velocity at corner point.

Here the plane strain problem of piercing by a flat punch into cohesive material is analytically solved by Hill[3]. The difference from the previous problem of surface penetration is not only the embedment, but also the roughness of the flat punch. As a rough punch is considered, the material below the punch does not slip to the sides, but only moves down. In contrast, the material along the shaft moves upwards. Hence an extremely strong displacement discontinuity occurs at the edges, as indicated in Figure (4.12b). In section 4.5 it will be shown that strong discontinuities like this tend to yield poorer finite element solutions. Here the numerical collapse load is much too high. Even a fine mesh is too much constrained, resulting in high stress concentrations at the edges. To overcome this effect of singular plasticity points, it would seem that we need to incorporate some potential slip lines into the finite element mesh. Provision for such slip lines is easily incorporated using interface elements in between two common finite elements.

It should be emphasized that such potential slip lines are not zones of weakness since they have the same strength properties as the rest of the material.

4.5 The penetration of a flat rigid punch in cohesive material

In this section the quality of interface stresses will be analyzed for the problem shown in Figure (4.13). In the context of soil mechanics this problem might represent a model test for a punch penetrating into clay. The material parameters for this problem are as follows

shear modulus	: $G = 1000$ kPa
Poisson's ratio	: $\nu = 0.49$
shear strength	: $c = 10$ kPa
interface stiffness	: $k_n = 50$ $k_s = 2500$ kN/m^3
adhesion	: $c_c = 10$ kPa

Note that the base of the punch is fully rough, whereas the side is fully smooth.

The theoretical solution given by Hill for the limit load is based on the

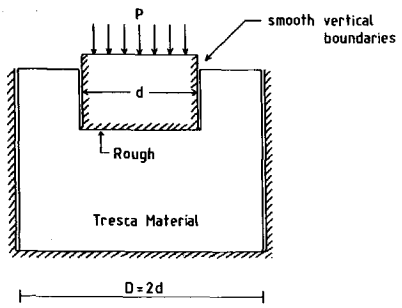

Figure 4.13. Rough rigid punch penetrating into cohesive material.

slip line field on the left hand side of Figure (4.14). The theoretical contact pressure at the base of the punch depends on the ratio of d/D where d is the width of the punch and D is the size of the container. We will consider the special ratio of d/D = 0.5 as it gives precisely a constant limiting contact pressure of $p = (\pi + 2)\, c$. Figure (4.15a) shows the finite element schematization of the punch problem. Along the base of the punch two interface elements were added to enable representation of contact pressures.

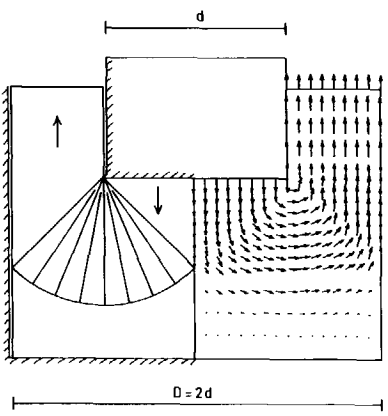

Figure 4.14. Velocity field at failure for a rough rigid punch.

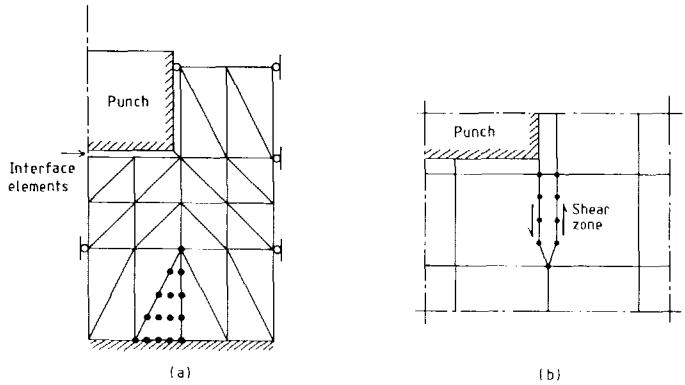

Figure 4.15. Finite element mesh for a punch indentation problem. (a) element subdivision. (b) potential slip plane.

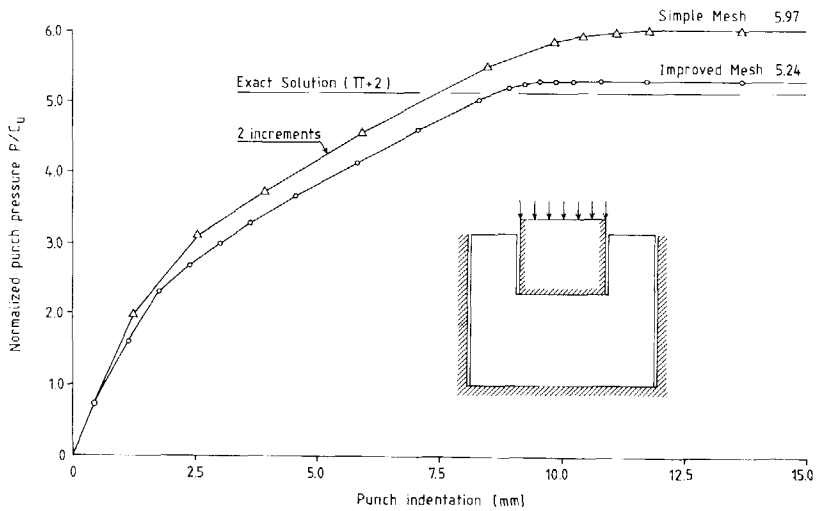

Figure 4.16. Load displacement curve for a rough rigid punch penetrating into cohesive soil.

The load-displacement curve as obtained by the finite element calculation is shown in Figure (4.16). A true limit load is obtained. This load is 14 per cent in excess of the exact solution. The computed stresses at the base of the punch are shown in Figure (4.17a). The quality of the computed stresses is quite poor; according to the theoretical solution, there should be no stress concentrations near the edges.

The finite element calculation was repeated for a mesh with potential discontinuities as indicated in Figure (4.15b). The load-displacement curve, Figure (4.16), shows that this schematization indeed computes a better collapse load. Now the error is only 2 per cent, as compared to the exact solution. The quality of interface stresses, Figure (4.17b), is also improved substantially; stress concentrations have virtually disappeared. Closer inspection of the results shows that at collapse the shear stress in the internal interface element is equal to the shear strength; it thus represents a true slip line.

Figure (4.14) shows the velocity field at collapse for the improved schematization. At the edge of the punch, the computed velocity actually becomes discontinuous as in the theoretical solution.

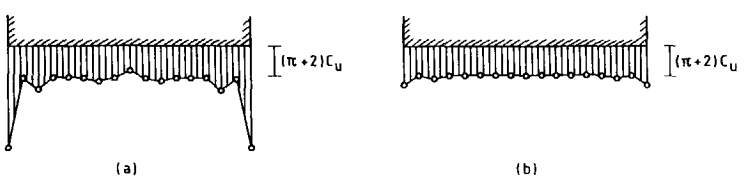

Figure 4.17. Computed contact pressure under a rigid punch. (a) simple mesh. (b) improved mesh with singular velocity point.

4.6 A solution to the trapdoor problem

The plane strain problem of a passive trapdoor, Figure (4.18), has been analyzed by several researchers[31,60]. In the context of this chapter the treatment of the boundary discontinuity at the edge of the trapdoor is of

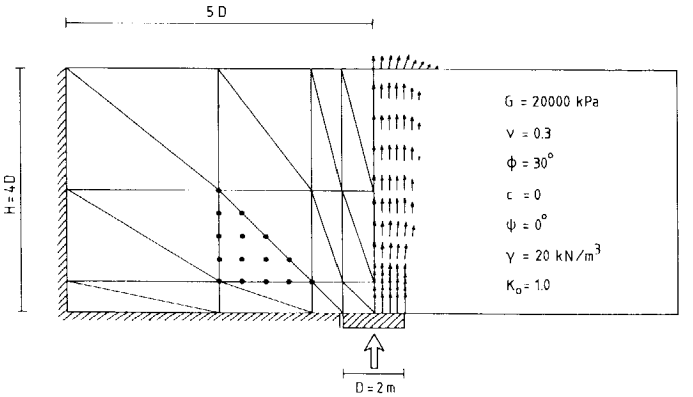

Figure 4.18. Finite element mesh and velocity field at failure for a trapdoor problem.

interest. In previous analyses this discontinuity was "smoothed out" by taking a linear variation of prescribed displacements in a small transition zone, Figure (4.19a). In the present analysis the mesh contains an interface element to anticipate the singular velocity, Figure (4.19b). Here, as in reality, the influence of this singularity is now concentrated in a very thin zone. The strength properties of the interface element coincide with those of the soil

$$k_n = 2.5\ k_s = 2500\ MN/m^3 \qquad \phi_c = \phi = 30^\circ$$
$$c_c = c = 0\ kPa \qquad \psi_c = \psi = 0^\circ$$

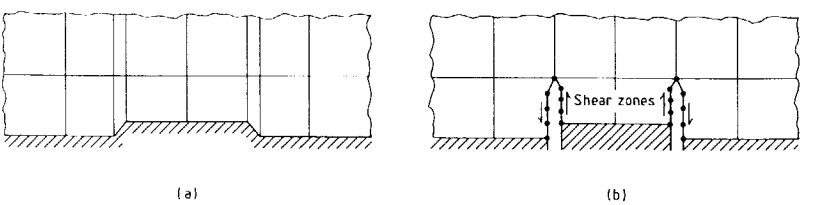

Figure 4.19. Solution to the trapdoor discontinuity. (a) conventional approach. (b) singular point approach.

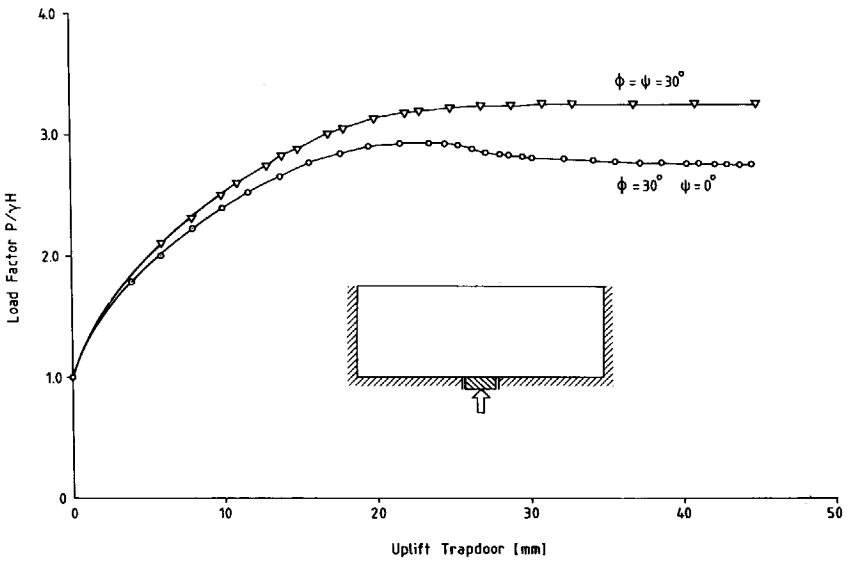

Figure 4.20. Load-displacement curves for a trapdoor problem.

Figure (4.20) shows the load-displacement curve for the uplift of the trapdoor. Now it might be argued that an interface in the interior of the mesh will erroneously attract the failure mechanism. To weaken this argument a second analysis was made for an associated material with a dilatancy angle of $\psi_c = \psi = 30^\circ$. The velocity field at collapse of this computation is shown in Figure (4.21). Now the shear band has an inclination with respect to the

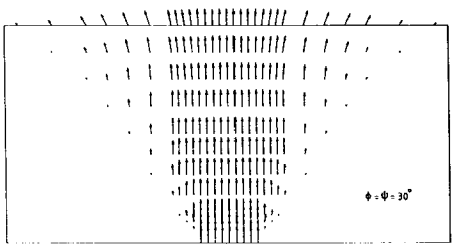

Figure 4.21. Velocity field at failure for a trapdoor problem in frictional material with high dilation.

vertical axis due to the dilation of the material. In this case the interface element only creates a velocity discontinuity at the boundary of the mesh. The shear band that originates at this point does not follow the direction of the interface.

4.7 Analysis of a pile penetration problem in cohesive soil

The empirical formulae for the bearing capacity of piles make a distinction between a tip contribution and a shaft contribution to the limit load. In this section we will concentrate on the end bearing for a pile with a flat tip, placed in a pre-bored hole, Figure (4.22). The pile is assumed to have been installed in a homogeneous clay layer. The properties are chosen in such a way that they correspond to undrained stiff clay behaviour:

ratio of shear modulus over cohesion:	$G/c = 100$
Poisson's ratio	$\nu = 0.49$

As friction is absent, the Coulomb yield criterion degenerates to the Tresca criterion. The contact between pile and soil is assumed to be completely rough, so the adhesion is equal to the shear strength of the soil.

The finite element schematization of this problem is shown in Figure (4.22). Again a mesh of 15-noded elements is used, supplemented with 10-noded interface elements along the tip and shaft of the pile. The latter interfaces are merely used to represent contact pressures. In a first schematization of the problem no special measures are taken to anticipate the discontinuous displacement at the edge of the tip. In a second schematization, however, the technique of adding internal interfaces, as developed in the previous sections, is employed. In this way two potential slip planes are created at the edge of the tip, Figure (4.23). Actually the singular point C in this figure is now split into four points. Starting at the prescribed vertical displacement of C_1, point C_2 slides horizontally away from C_1. Relative to this, point C_3 slides vertically. The net displacement of point C_4 is upwards, allowing for slip along the shaft.

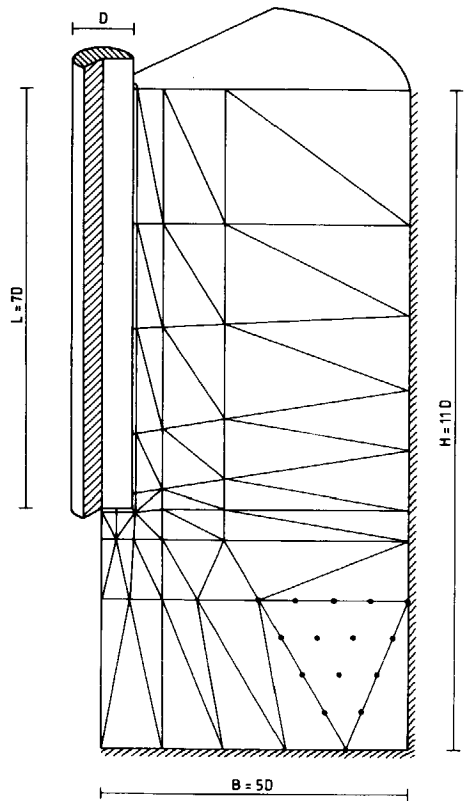

Figure 4.22. Finite element mesh for a pile penetration problem.

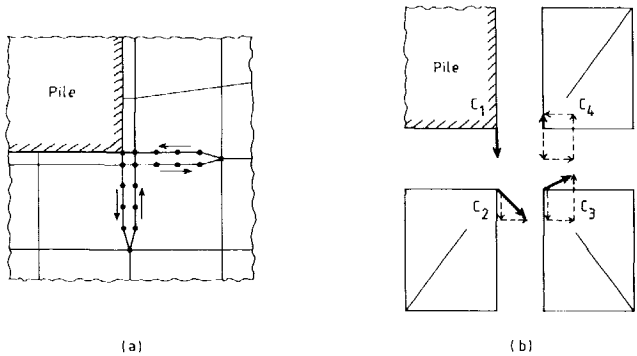

Figure 4.23. Introduction of potential slip planes in the finite element mesh for a pile.

Bearing factors for the simple and the improved mesh are compared in Figure (4.24). The bearing factor, N_c, is the ratio of the average contact pressure over the shear strength. Empirical factors reported in the literature[61] range between 10 and 20. Both analyses fall within this range. However, the simple mesh yields a 25 per cent higher limit load as compared to the improved mesh. This difference is even more dramatic than in the analysis of the punch problem, where a 12 per cent difference was obtained.

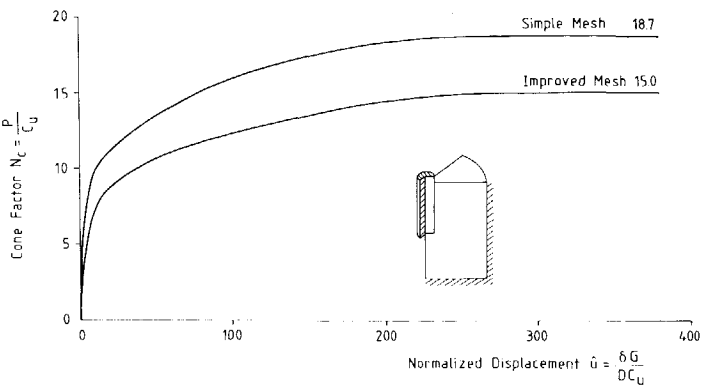

Figure 4.24. Tip reaction curve for a penetrating pile with a flat tip.

Note that open hole computations[62] yield values in the order of $N_c = 9$. However, in such analyses the soil at the shaft is free to move inward.

In the simple schematization of the Hill punch problem, the overshoot of the limit load was caused by a stress concentration near the edge of the punch. The same proves to be the case in the present analysis, as can be seen from Figure (4.25a). Again the simple mesh shows a stress concentration near the edge of the tip. For axisymmetric configurations this contributes even more to the limit load than in the case of plane strain, as the area increases with radius. In addition to this, the pressure on the lower part of the shaft obtained with this simple mesh shows a non-physical raggedness. The improved mesh, on the other hand, is found to yield much better results, as indicated in Figure (4.25b). The tip pressure distribution is very smooth and does not culminate in a peak value near the edge. The same smoothness characterizes the shaft pressure.

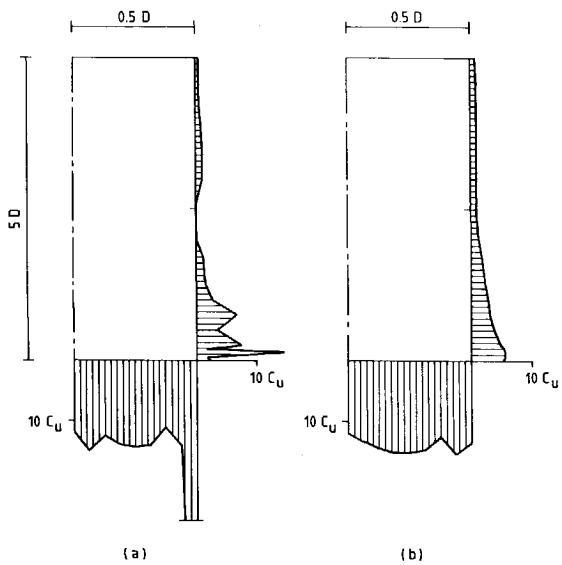

Figure 4.25. Contact pressure along tip and shaft for a penetration problem at failure. (a) simple mesh. (b) improved mesh with singular point treatment.

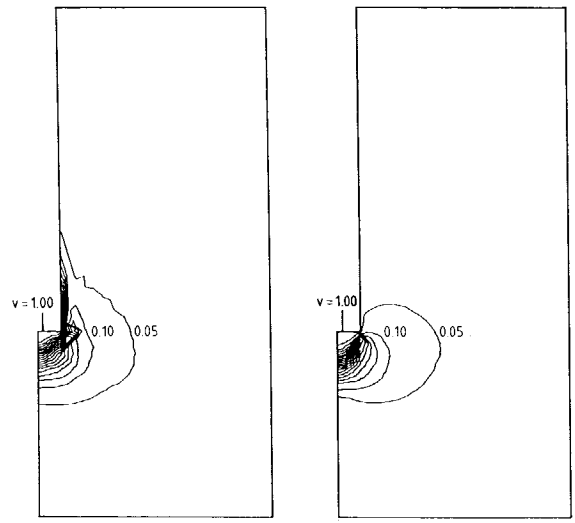

Figure 4.26. Velocity intensity contours for a pile at failure. (a) simple mesh. (b) improved mesh with singular point treatment.

Like in the Hill problem, the simple schematization for the pile problem suffers from a lack of flexibility near the edge of the tip. This can also be demonstrated by looking at the contour plots of the velocity intensity at failure, Figure (4.26). This intensity is defined as:

$$v = \frac{\sqrt{v_x^2 + v_y^2}}{v_{pile}} \tag{4.34}$$

where v_x and v_y denote the Cartesian components of the velocity at a material point. For both meshes the soil movement appears to be concentrated near the tip of the pile. The only, albeit significant, difference between the two sets of contour lines is the soil velocity field at the lower part of the shaft. In the result for the simple schematization, Figure (4.26a), a concentration of contours is obtained, indicating a zone with a high velocity gradient. In this region, the soil elements distort without any slip at the shaft, even though

interface elements were used. Apparently, the boundary condition at the corner point prevents direct slipping. As explained before, splitting the corner into four separate points allows for slip along the shaft in the improved schematization. As a result the contour plot for this case, Figure (4.26b), does not show a high velocity gradient in the soil elements near the shaft. Now the mesh offers enough flexibility to cope with the corner singularity.

Some researchers[31,63] performed similar small strain computations for the bearing factor. A striking difference between the present analysis and those in the literature is the normalized displacement, u, at which collapse is assumed. This displacement is defined as

$$u = \frac{\delta \; G}{D \; c} \tag{4.35}$$

where

δ = tip displacement

D = pile diameter

G = shear modulus

c = cohesion

A typical value in the literature is in the order of u = 25, whereas collapse occurs here at a value of approximately u = 300. Apparently collapse is assumed to occur when the tangent to the tip reaction curve becomes very small as compared to the initial one. Indeed, at a value of u = 30 the present analysis already yields a slope reduction of 98 per cent. However, it can be seen from the tip reaction curves that at this point the tip factor is still far from its ultimate value. In fact, when collapse is assumed at this point, a bearing factor of about 9 instead of 15 is obtained.

5. A CAP PLASTICITY MODEL FOR SAND

So far attention has been focused on the prediction of collapse loads for problems of soil-structure interaction. Methods for tracing the equilibrium path and for the treatment of singular points in the deformation field were introduced to enable accurate predictions of limit loads. The Mohr-Coulomb model computes fairly accurate collapse loads and, as a consequence, the subject of constitutive modelling has not yet received much attention. However, in this chapter we aim to analyze pre-failure displacements. Consequently, we need to study the capability of the model to predict accurate deformations.

First, the suitability of the Mohr-Coulomb model for making engineering predictions of deformation is discussed. In addition, the desired characteristics of an improved model are outlined. Secondly, a cap model, which is based on well-known soil parameters, is proposed and elaborated. This model is first developed for triaxial stress states only. Simulation of some proportional strain paths demonstrates its possibilities and limitations. After that, an extension to general stress states is given. The numerical integration of the model is discussed in a separate section.

5.1 Limitations of the elastic-perfectly plastic model

The elastic-perfectly plastic Mohr-Coulomb model, as outlined in section 3.6.1, uses Hooke's law to describe an isotropic elastic response. Consequently, only two parameters, say the shear modulus G and Poisson's ratio ν, can be chosen to match test results. This gives rise to two questions, namely: which test should be used to obtain those parameters and how should the result be linearized to determine their value.

The most common laboratory tests in engineering practice are the oedometer test, the triaxial test and the simple and direct shear tests[64]. As the number of parameters is limited, we should choose the test which best reflects the deformations to be expected in the engineering problem being considered. Unfortunately, many engineering problems display all kinds of deformations. In a pile penetration problem, for example, the soil underneath the tip is subject to high isotropic compression, whereas near the shaft the soil is

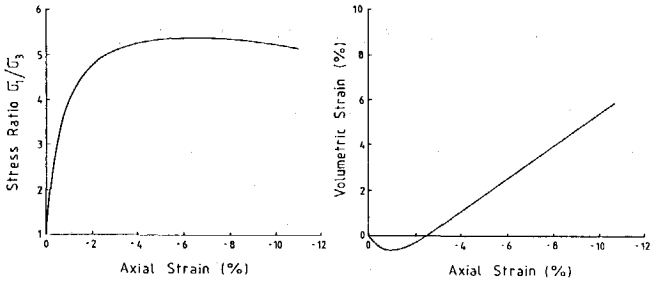

Figure 5.1.Triaxial test results for sand.

highly distorted. Changes in deformation can also occur during the loading history, like in a footing problem when the direction of loading changes from vertical (compression) to horizontal (shearing). This now reveals a shortcoming of the model. When the shear modulus and Poisson's ratio are obtained from one specific test, the prediction of deformations will only be accurate for a limited range of stress paths.

Figure (5.1) shows a typical result from a triaxial test on sand. From this, values for G and ν could be obtained by linearizing a relevant part of the curve. Values for ν_0 tend to be in the order of 0.0 to 0.2, whilst for ν_{50} values of up to 0.3 can be found. If we now suppose that a one-dimensional settlement problem were to be simulated, we would obtain a K_0 value in the range of 0.0 to 0.4, which is fairly low. Clearly, we have thus exceeded the applicability of the obtained Poisson's ratio.

A major shortcoming of the model becomes clear when isotropic compression is considered. In this case, the model predicts elastic response irrespective of the load level. However, compression tests clearly show that the volumetric strain consists of a reversible as well as an irreversible part, Figure (5.2). So, when selecting the elastic parameters, we should choose between accurate prediction of compression or of swelling, realizing that either of the two excludes the other. From inspection of compression tests on sand, it becomes clear that typical differences between bulk moduli in compression and swelling respectively are in the order of a factor 2 to 3. At first glance, it would seem attractive to determine a shear modulus from the triaxial test and a bulk modulus from the isotropic or one-dimensional compression test. It would seem that in this way, at least when considering loading only, we will obtain good predictions of distortion and compression at the same time. Unfortunately, it

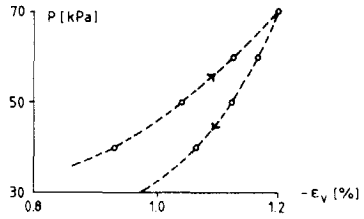

Figure 5.2. Isotropic compression and swelling of sand.

is very likely that this will result in a negative value of Poisson's ratio. Although a negative value for ν is not excluded from a theoretical point of view, it has never been observed in a test and should therefore be avoided.

When designing a model with a higher degree of accuracy, a balance should be struck between the increase of predictive power and that of complexity. Here an outline is given of the desired features of such a model.

We would like to obtain a model which gives a better prediction of compressive behaviour. This is of the utmost importance when studying for example a pile penetration problem, as it involves a zone of high compression just underneath the pile tip.

An initial improvement could be obtained by introducing hardening plasticity for compressive stress paths. In this manner, it is possible to differentiate between swelling and compression behaviour. A low bulk modulus in compression is then feasible without affecting elastic constants.

Secondly, accurate prediction of K_0 consolidation would mean a considerable enhancement of the model. This behaviour could then be captured without the need for high values of Poisson's ratio.

In fact, the model behaviour in both types of compression can be improved by introducting a cap plasticity concept, as will be shown in the next section.

5.2 A K_0-cap model in triaxial stress space.

Figure (5.2) shows a typical result from an isotropic compression test on sand. In reference (65) it is shown that both the swelling and compression behaviour can approximately be described by the logarithmic functions

$$\varepsilon_c - \varepsilon_{c0} = \lambda^* \ln\left(\frac{p}{p_0}\right) \quad ; \quad \varepsilon_s - \varepsilon_{s0} = \kappa^* \ln\left(\frac{p}{p_0}\right) \tag{5.1}$$

in which λ^* and κ^* are referred to as compression index and swelling index respectively. Both ε_c and ε_s stand for volumetric strains and not void ratios as more frequently used. Conform Houlsby[65], we write λ^* and κ^* and not λ and κ since the latter classically refer to void ratio's. When both expressions are differentiated, we obtain the following definitions of bulk moduli

$$K_c \equiv \frac{\dot{p}}{\dot{\varepsilon}_c} = p/\lambda^* \quad ; \quad K_s \equiv \frac{\dot{p}}{\dot{\varepsilon}_s} = p/\kappa^* \tag{5.2}$$

Apparently, the ratio of K_c over K_s remains constant during loading and unloading.

As we do not want to introduce more elastic constants, the K_s modulus should be derived from G and ν in the following way

$$K_s = \frac{2G(1+\nu)}{3(1-2\nu)} \tag{5.3}$$

The bulk modulus in compression is now readily derived from

$$K_c = \frac{\kappa^*}{\lambda^*} K_s \tag{5.4}$$

Consequently, we introduce λ^*/κ^* as a new material parameter. Its value can be determined from the expression

$$\frac{\lambda^*}{\kappa^*} = \frac{\Delta\varepsilon_c}{\Delta\varepsilon_s} \tag{5.5}$$

which relates it to the ratio of total over recoverable strain in an isotropic compression test.

Equation (5.2) specifies a linear relationship between the bulk moduli and the isotropic stress. This concept is not adopted in the present model. Instead, a choice is made for a dependency of the shear modulus on the pressure. Moreover, this relationship is not linear but of the form

$$G = G_a \left(\frac{p}{p_a} \right)^{\beta} \tag{5.6}$$

where p_a is the equivalent of 100 kPa in the appropriate units of p, and G_a is the shear modulus at this pressure. Factor β depends on the material under consideration. For sand we use $\beta \cong 0.5$, whereas for clay $\beta \cong 1.0$ would be more appropriate. This dependency was proposed by Vermeer[66] after inspection of many triaxial test data on sand and clay. This choice now implies that both K_c and K_s become a non-linear function of the pressure.

To obtain a model for triaxial stress states, the concept of a cap yield function will be introduced. Several such models have been derived in the literature before. Among the best known are the Cam-clay model[67] and its modified versions[68-71]. The common feature of all of these models is that the elastic region in stress space is bounded by a closed yield surface, as depicted in Figure (5.3). Another family of constitutive models[72-76] is found by combining two separate surfaces, one to describe shear behaviour and the other to model compression. As an example of this group, Figure (5.4) shows the double hardening model by Vermeer[72].

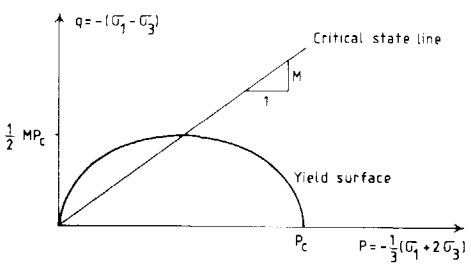

Figure 5.3. Yield locus of the Modified Cam-clay model.

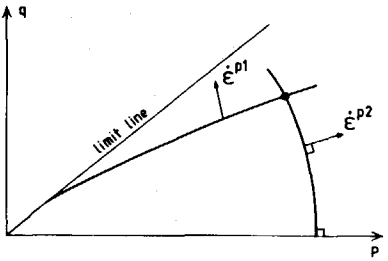

Figure 5.4. Yield loci of Vermeer's[72] double hardening model.

Here the second concept will be chosen, for it can be based on the well-established Mohr-Coulomb model. In fact, we can enhance this model simply by adding a cap yield function. The shape of this function in triaxial stress space could be determined in detail by a series of tests with proportional strain paths. However, this is obviously beyond the objective of the model, as set out in the previous section. Here, another approach will be taken. The general shape of the cap will be chosen so that it is in qualitative agreement with observations; its final shape will be determined by one parameter only. This parameter can then be chosen in such a way that in one-dimensional compression a realistic K_0 state is obtained. In fact, this K_0 value will be the last input parameter of the model.

For the mathematical description of the cap-plasticity model, the isotropic stress p and shear stress q are introduced

$$p = -\frac{1}{3}(\sigma_1 + 2\sigma_3) \quad ; \quad q = -(\sigma_1 - \sigma_3) \tag{5.7}$$

where σ_1 and $\sigma_2 = \sigma_3$ are the principal stresses. Note that here the conventions $\sigma_3 > \sigma_2 > \sigma_1$ and tension positive are adopted. Consequently, positive p denotes compression. The Mohr-Coulomb yield surface and the cap surface can be written in terms of parameters p and q. For the Mohr-Coulomb surface we thus find

$$f_m(p,q) = q - Mp - C \tag{5.8}$$

where

$$M = \frac{6 \sin\phi}{3 - \sin\phi} \quad ; \quad C = \frac{6\, c \cos\phi}{3 - \sin\phi} \tag{5.9}$$

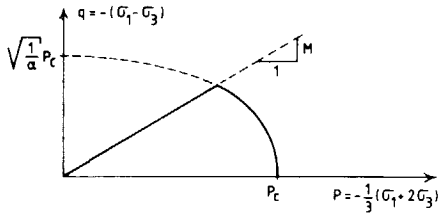

Figure 5.5. The K_0-cap model in triaxial stress space.

Figure (5.5) shows the cap surface that will be used in this study. The shape of this cap has some similarity to that of the modified Cam-clay model. However, the present cap has its crest point at the intersection with the q-axis, whereas in the modified Cam-clay model it is located at the intersection with the critical state line. The present cap yield surface is described by the expression

$$f_c(p,q) = p^2 + \alpha\, q^2 - p_c^2 \tag{5.10}$$

where α determines the shape of this cap and p_c determines its position. The change of p_c will be described by a hardening relation which is based on the former considerations of isotropic compression. Parameter α will be related to the coefficient of lateral earth pressure in one-dimensional compression, K_0.

Expression (5.10) is as a yield function in a hardening plasticity model. The general relation (2.59) for the flow rule of a strain-hardening material can in the case of a single hardening parameter be reformulated in the following way

$$\dot{\underline{\varepsilon}}^p = \frac{1}{h}\, \underline{n}_g\, \underline{n}_f^T\, \dot{\underline{\sigma}} \tag{5.11}$$

where unit vectors $\underline{n}_f$ and $\underline{n}_g$ are defined as

$$\underline{n}_f = \frac{\partial f}{\partial \underline{\sigma}} \Big/ \left|\frac{\partial f}{\partial \underline{\sigma}}\right| \quad ; \quad \underline{n}_g = \frac{\partial g}{\partial \underline{\sigma}} \Big/ \left|\frac{\partial g}{\partial \underline{\sigma}}\right| \tag{5.12}$$

and h follows from the consistency condition

$$\dot{f} \equiv \frac{\partial f}{\partial \underline{\sigma}}^T \dot{\underline{\sigma}} + \frac{\partial f}{\partial p_c} \dot{p}_c = 0 \tag{5.13}$$

The increase of p_c can be related to the plastic strain rate by considering isotropic compression. The rate of plastic volume strain is found by subtracting $\dot{\varepsilon}_s$ from $\dot{\varepsilon}_c$ as defined in equation (5.2)

$$\dot{\varepsilon}_v^p = \frac{\dot{p}}{K_c} - \frac{\dot{p}}{K_s} = \frac{1}{H} \dot{p} \tag{5.14}$$

where

$$H = \frac{K_c K_s}{K_s - K_c} \tag{5.15}$$

Note that hardening modulus H can be related to λ^*/κ^* and K_s with the aid of expression (5.4)

$$H = \frac{\kappa^*/\lambda^*}{1 - \kappa^*/\lambda^*} K_s \tag{5.16}$$

For isotropic compression, where $q = 0$, $\dot{p}$ and $\dot{p}_c$ coincide. Consequently, $\dot{p}$ in equation (5.14) can be replaced by $\dot{p}_c$ to obtain

$$\dot{p}_c = H \dot{\varepsilon}_v^p \tag{5.17}$$

This is the desired hardening relation which can be used to supplement the consistency condition. In this section, the following definition of strain rate is adopted

$$\dot{\underline{\varepsilon}} = \begin{bmatrix} \dot{\varepsilon}_p \\ \dot{\varepsilon}_q \end{bmatrix} \tag{5.18}$$

where the volumetric strain rate $\dot{\varepsilon}_p$ and the distortion $\dot{\varepsilon}_q$ are defined as

$$\dot{\varepsilon}_p = -\frac{1}{3}(\dot{\varepsilon}_1 + 2\dot{\varepsilon}_3) \quad ; \quad \dot{\varepsilon}_q = -(\dot{\varepsilon}_1 - \dot{\varepsilon}_3) \tag{5.19}$$

Consequently, the hardening relation (5.17) can be transformed into a more

general form

$$\dot{p}_c = H \, \underline{e}_p^T \, \underline{\dot{\varepsilon}}^p \tag{5.20}$$

where

$$\underline{e}_p = \begin{bmatrix} 3 \\ 0 \end{bmatrix} \tag{5.21}$$

Combination of equations (5.11), (5.13) and (5.20) yields, after some rearranging, the following expression for h

$$h = - H \left(\frac{\partial f}{\partial p_c} \underline{e}_p^T \underline{n}_g \right) \Big/ \left| \frac{\partial f}{\partial \underline{\sigma}} \right| \tag{5.22}$$

The present model will be based on the concept of associated plasticity, namely

$$\frac{\partial g}{\partial \underline{\sigma}} = \frac{\partial f}{\partial \underline{\sigma}} \tag{5.23}$$

Parameter h can be evaluated for the proposed yield function of equation (5.10)

$$h = 3 \, H \, \frac{p_c \, p}{p^2 + \alpha^2 q^2} \tag{5.24}$$

For stress states on the yield surface, f_c in equation (5.10) vanishes. This enables us to express p_c in terms of p and q

$$p_c = \sqrt{p^2 + \alpha \, q^2} \tag{5.25}$$

Combining equations (5.24) and (5.25) yields the desired expression for parameter h

$$h = 3 \, H \, \frac{\sqrt{1 + \alpha \, (q/p)^2}}{1 + \alpha^2 (q/p)^2} \tag{5.26}$$

The relation between α in equation (5.10) and the coefficient of lateral earth pressure, K_0, can be derived by considering the general constitutive equation for the cap model. This equation is obtained by adding the elastic strain rate

to the plastic strain rate in expression (5.11)

$$\dot{\underline{\varepsilon}} = \underline{\underline{D}}^{-1} \dot{\underline{\sigma}} + \frac{1}{h} \underline{n}_f \underline{n}_f^T \dot{\underline{\sigma}} \tag{5.27}$$

This relation can be written in full as

$$\begin{aligned} \dot{\varepsilon}_p &= \tfrac{1}{3} \dot{p} / K_s + (\dot{p}\, n_p^2 + \dot{q}\, n_p n_q) / h \\ \dot{\varepsilon}_q &= \tfrac{1}{2} \dot{q} / G + (\dot{p}\, n_p n_q + \dot{q}\, n_q^2) / h \end{aligned} \tag{5.28}$$

Here, n_p and n_q are the components of vector $\underline{n}_f$. In one-dimensional compression, a distinct relationship exists between $\dot{\varepsilon}_p$ and $\dot{\varepsilon}_q$, as well as between $\dot{p}$ and $\dot{q}$, namely

$$\dot{\varepsilon}_p = \tfrac{1}{3} \dot{\varepsilon}_q \; ; \quad \dot{q} = \bar{K}_0 \dot{p} \tag{5.29}$$

where

$$\bar{K}_0 = \frac{3(1-K_0)}{1+2K_0} \tag{5.30}$$

Apparently, α should be such that

$$\frac{h}{G} \bar{K}_0 + 2 (n_p n_q + \bar{K}_0 n_q^2) = 2 \frac{h}{K_s} + 6 (n_p^2 + \bar{K}_0 n_p n_q) \tag{5.31}$$

At the intersection between the K_0 line and the cap, the values for n_p and n_q are

$$n_p = \frac{1}{\sqrt{1 + \alpha^2 \bar{K}_0^2}} \quad ; \quad n_q = \frac{\alpha \bar{K}_0}{\sqrt{1 + \alpha^2 \bar{K}_0^2}} \tag{5.32}$$

and for parameter h we obtain

$$h = 3 H \frac{\sqrt{1 + \alpha \bar{K}_0^2}}{1 + \alpha^2 \bar{K}_0^2} \tag{5.33}$$

Substitution of those expressions in condition (5.31) yields for α

$$2 \bar{K}_0^3 \alpha^2 + 2 (\bar{K}_0 - 3 \bar{K}_0^2) \alpha - 6 = 3 (2 \frac{H}{K_s} - \frac{H}{G} \bar{K}_0) \sqrt{1 + \alpha \bar{K}_0^2} \tag{5.34}$$

This equation should be solved iteratively. To this end, it is used as a predictor - corrector scheme: the left hand side computes a correction from substitution of a prediction in the right hand side. Starting this process with $\alpha = 0$, it rapidly converges to a positive root.

The plasticity model which follows from the combination of perfect elasticity according to Hooke's law with the Mohr-Coulomb yield function and the above cap function will be called the K_0-cap model. It has eight constants, all of which have a distinct engineering background. In addition to the well-known five parameters of the Mohr-Coulomb model, namely G, ν, ϕ, c and ψ, three extra constants are introduced: λ^*/κ^* K_0 and the overconsolidation ratio OCR. This last parameter determines the initial position of the cap yield locus in the following way

$$p_c^0 = OCR \sqrt{p_0^2 + \alpha\, q_0^2} \tag{5.35}$$

where p_0, q_0 is the initial stress state.

In the remainder of this section, it will be demonstrated how the model behaves when subjected to some proportional strain paths. In addition, a drained triaxial test will be simulated.

Figure (5.6) shows a qualitative plot of the stress paths obtained for three different strain paths. The first path results from isotropic compression, number two follows from loading and unloading in one-dimensional compression and number three is obtained from an undrained triaxial test. For dilative

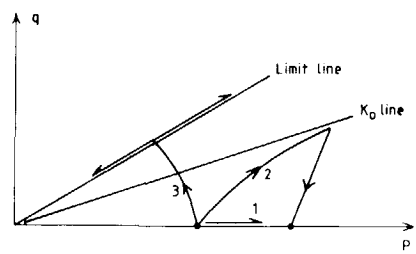

Figure 5.6. Stress paths from the K_0-cap model for (1) isotropic compression, (2) oedometer test, (3) undrained triaxial test.

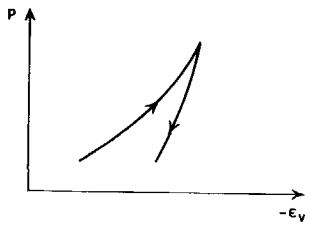

Figure 5.7. K_0-cap model in isotropic compression and swelling.

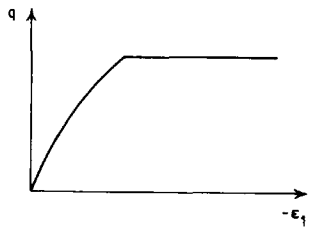

Figure 5.8. Simulation of a drained triaxial test.

material, in which $\psi > 0$, stress path number three continues upwards on the failure line, whereas for $\psi < 0$, it moves in the opposite direction. In isotropic and one-dimensional compression, the stress strain curves of Figure (5.7) are obtained.

The stress strain curve for a triaxial test simulation is shown in Figure (5.8). The abrupt change in the curve corresponds to the point where the failure line is reached. Typical values computed for G_0 / G_{50} are in the range of 1.5 to 2.5.

5.3 Generalization to general stress states

The K_0-cap model of the previous section only describes stress paths in triaxial stress space. Here, the model will be extended to include general stress and strain paths. In a first subsection, the cap yield function is described in principal stress space. The form of this general cap surface is such that it intersects the Mohr-Coulomb surface in a deviatoric plane. To this end, ridges are introduced in the cap surface. In a second subsection, the plastic flow rule will be extended to deal with singular points and singular lines in the combined yield surface.

5.3.1. A cap yield surface in principal stress space

In principal stress space, the Mohr-Coulomb surface is determined by the

equation

$$-\frac{1}{2}(\sigma_1 - \sigma_3) + \frac{1}{2}(\sigma_1 + \sigma_3)\sin\phi - c\cos\phi = 0 \tag{5.36}$$

at least when $\sigma_3 > \sigma_2 > \sigma_1$ and when tension is assumed to be positive. Alternatively, this may be presented as follows

$$\bar{q} - M\bar{p} - C = 0 \tag{5.37}$$

where

$$\begin{aligned} \bar{p} &\equiv -\frac{1}{3}(\sigma_1 + \sigma_2 + \sigma_3) \\ \bar{q} &\equiv (\sigma_2 - \sigma_1) + \frac{3 + \sin\phi}{3 - \sin\phi}(\sigma_3 - \sigma_2) \end{aligned} \tag{5.38}$$

For these definitions equation (5.37) coincides exactly with equation (5.36). Moreover, for $\sigma_2 = \sigma_3$, $\bar{p}$ and $\bar{q}$ coincide with p and q of equation (5.7). Constants M and C in the above expression are defined in equation (5.9). This suggests a general approach for extending a criterion in p,q space to a criterion in principal stress space, namely by replacing stress parameters p and q by the parameters of equation (5.38). Thus we obtain a family of surfaces, $f(\bar{p},\bar{q}) = 0$, which have in common that their intersection with the deviatoric plane is a straight line. For every choice of $\bar{p}$ and $\bar{q}$ which makes f vanish, the equation of this line is given by the intersection of the planes v_1 and v_2

$$\begin{aligned} v_1 &: (\sigma_1 + \sigma_2 + \sigma_3) = -3\,\bar{p} \\ v_2 &: (\sigma_2 - \sigma_1) + \frac{3 + \sin\phi}{3 - \sin\phi}(\sigma_3 - \sigma_2) = \bar{q} \end{aligned} \tag{5.39}$$

The direction vector $\underline{r}$ of this line is found by computing the cross product of the normal vectors of v_1 and v_2

$$\underline{r} = \begin{bmatrix} 1 + \sin\phi \\ -2 \\ 1 - \sin\phi \end{bmatrix} \tag{5.40}$$

Figure (5.9) shows the yield surfaces of the K_0-cap model. The six intersecting cap surfaces are obtained from a permutation of σ_1, σ_2 and σ_3 in the definition (5.38) of $\bar{q}$.

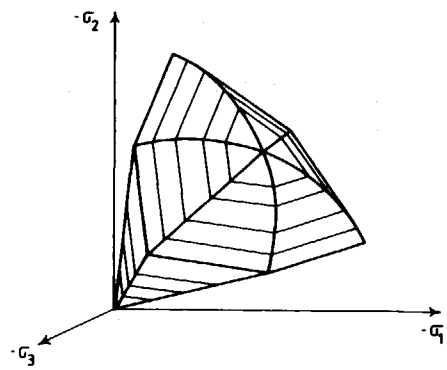

Figure 5.9. K_0-cap yield surfaces in principal stress space.

The above generalization of the cap model may seem quite arbitrary and it may be questioned whether the proposed shape is supported by test results. For high values of $\bar{q}$, i.e. near the Mohr-Coulomb surface, the soil behaviour will be influenced by impending failure and, as a result, it is favourable that in the deviatoric plane the shapes of the Mohr-Coulomb surface and the cap surface coincide. However, near the hydrostatic axis, a circular shape would seem more appropriate. For low values of $\bar{q}$, the frictional characteristics of the material are less pronounced. Nevertheless, the angular cap will be used here, as it has some attractive features. First of all, thanks to the simplicity of the generalization, the mathematical description of the model becomes quite simple. Secondly, fully angular models, like the Mohr-Coulomb model, tend to improve the stability of numerical solution procedures. Smooth yield surfaces may involve zones of high curvature. For stress states in such zones, a slight change in the direction of the strain increment may yield a significant change in the direction of the stress increment. This may lead to numerical instabilities. However, a fully angular model involves so-called yield vertices, which implies that for a region of strain directions the stress remains on the ridge. This proves to stabilize numerical procedures. A last argument in favour of the angular model is that it does not introduce additional parameters to describe the shape of the yield locus in the deviatoric plane.

5.3.2 Mathematical description of the K_0-cap model

The general flow rule for a multi-surface plasticity model is given in section (2.5),

$$\dot{\underline{\varepsilon}}^p = \sum_{i=1}^{n} \dot{\lambda}_i \frac{\partial g_i}{\partial \underline{\sigma}} \tag{5.41}$$

where the index i ranges over all active yield surfaces. The multipliers are solved from the consistency conditions $\dot{f}_i = 0$. Hence, the number of unknown multipliers $\dot{\lambda}_i$ is equal to the number of active yield surfaces. From Figure (5.9) it becomes clear that for stress states on the cap surface, the number of active yield functions can be one, two, four or six. Here it will be shown that, due to symmetry, the number of simultaneous equations will not exceed two. The following discussion concentrates on the treatment of ridges and of singular points in the surface.

In the remainder of this section, we will differentiate between two types of ridges. The first type is found from the intersection of the yield surface with a triaxial plane, whereas the second is found from the intersection of the cap surface and the Mohr-Coulomb surface. For convenience, the first type will be called a triaxial ridge and the second a deviatoric ridge, for it is contained in a deviatoric plane.

In general, the consistency conditions for a stress state on a ridge read in full

$$\begin{aligned} \dot{f}_1 &\equiv \frac{\partial f}{\partial \underline{\sigma}}_1^T \dot{\underline{\sigma}} + \frac{\partial f}{\partial p_c}_1 \dot{p}_c = 0 \\ \dot{f}_2 &\equiv \frac{\partial f}{\partial \underline{\sigma}}_2^T \dot{\underline{\sigma}} + \frac{\partial f}{\partial p_c}_2 \dot{p}_c = 0 \end{aligned} \tag{5.42}$$

When the flow rule (5.41) is substituted, this yields a linear system of equations for $\dot{\lambda}_1$ and $\dot{\lambda}_2$. In fact, this is the way we should proceed for a deviatoric ridge, as no further simplification is possible.

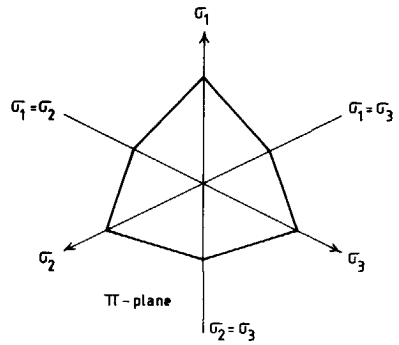

Figure 5.10. Symmetry of yield surfaces with respect to the triaxial planes.

However, Figure (5.10) shows that at a triaxial ridge the intersecting surfaces are symmetric with respect to the triaxial plane. This characteristic can be exploited in the solution of the consistency conditions. To this end, those conditions are summed to become one

$$\dot{f}^{*} \equiv \underline{a}_{s}^{T}\, \dot{\underline{\sigma}} + \frac{\partial f^{*}}{\partial p_{c}}\, \dot{p}_{c} = 0 \tag{5.43}$$

where $f^{*} = f_1 + f_2$ and

$$\underline{a}_{s} = \frac{\partial f}{\partial \underline{\sigma}}_{1} + \frac{\partial f}{\partial \underline{\sigma}}_{2} \tag{5.44}$$

The increment of stress is found from

$$\dot{\underline{\sigma}} = \underline{\underline{D}}\, \dot{\underline{\varepsilon}} - \underline{\underline{D}} \left(\dot{\lambda}_1 \frac{\partial g}{\partial \underline{\sigma}}_{1} + \dot{\lambda}_2 \frac{\partial g}{\partial \underline{\sigma}}_{2} \right) \tag{5.45}$$

which can be restated as follows

$$\dot{\underline{\sigma}} = \underline{\underline{D}}\, \dot{\underline{\varepsilon}} - \underline{\underline{D}} \left(\tfrac{1}{2}(\dot{\lambda}_1 + \dot{\lambda}_2)\, \underline{b}_{s} + \tfrac{1}{2}(\dot{\lambda}_1 - \dot{\lambda}_2)\, \underline{b}_{d} \right) \tag{5.46}$$

where

$$\underline{b}_{s} = \left(\frac{\partial g}{\partial \underline{\sigma}}_{1} + \frac{\partial g}{\partial \underline{\sigma}}_{2} \right) \quad ; \quad \underline{b}_{d} = \left(\frac{\partial g}{\partial \underline{\sigma}}_{1} - \frac{\partial g}{\partial \underline{\sigma}}_{2} \right) \tag{5.47}$$

Due to symmetry of the yield and plastic potential surfaces, vectors $\underline{a}_s$ and $\underline{b}_s$ are parallel to the triaxial plane, whereas vector $\underline{b}_d$ is perpendicular to this plane. Consistency condition (5.43) can be supplemented with equation (5.46) to obtain

$$\underline{a}_s^T \underline{\underline{D}} \dot{\underline{\varepsilon}} - \tfrac{1}{2}(\dot{\lambda}_1 + \dot{\lambda}_2)\, \underline{a}_s^T \underline{\underline{D}}\, \underline{b}_s - \tfrac{1}{2}(\dot{\lambda}_1 - \dot{\lambda}_2)\, \underline{a}_s^T \underline{\underline{D}}\, \underline{b}_d + \frac{\partial f^*}{\partial p_c} \dot{p}_c = 0 \tag{5.48}$$

As matrix $\underline{\underline{D}}$ is derived from isotropic elasticity according to Hooke, we have in addition

$$\underline{a}_s^T \underline{\underline{D}}\, \underline{b}_d = 2G\, \underline{a}_s^T \underline{b}_d = 0 \tag{5.49}$$

which leads to the following simplified equation

$$\underline{a}_s^T \underline{\underline{D}} \dot{\underline{\varepsilon}} - \dot{\lambda}^* \underline{a}_s^T \underline{\underline{D}}\, \underline{b}_s + \frac{\partial f^*}{\partial p_c} \dot{p}_c = 0 \tag{5.50}$$

where $\dot{\lambda}^* = \frac{1}{2}(\dot{\lambda}_1 + \dot{\lambda}_2)$. For a non-hardening surface, like the Mohr-Coulomb surface, it follows that

$$\frac{\partial f^*}{\partial p_c} \dot{p}_c = 0 \tag{5.51}$$

and, as a result, $\dot{\lambda}^*$ can be solved from

$$\dot{\lambda}^* = \frac{\underline{a}_s^T \underline{\underline{D}} \dot{\underline{\varepsilon}}}{\underline{a}_s^T \underline{\underline{D}}\, \underline{b}_s} \tag{5.52}$$

So far the Mohr-Coulomb yield surface has been considered, for which we assume perfect plasticity with $\partial f^*/\partial p_c = 0$. For a ridge on the hardening cap the expression for $\dot{\lambda}^*$ is slightly more involved. In this case equation (5.20) yields

$$\frac{\partial f^*}{\partial p_c} \dot{p}_c = H \frac{\partial f^*}{\partial p_c}\, \underline{e}_p^T \left(\dot{\lambda}^*\, \underline{b}_s + \tfrac{1}{2}(\dot{\lambda}_1 - \dot{\lambda}_2)\, \underline{b}_d \right) \tag{5.53}$$

where

$$\underline{e}_p = \frac{\partial \varepsilon_v^p}{\partial \underline{\varepsilon}^p} \tag{5.54}$$

Vector $\underline{e}_p$ points along the hydrostatic axis, which implies that

$$\underline{e}_p^T \, \underline{b}_d = 0 \tag{5.55}$$

As a result, equation (5.50) yields for this case

$$\dot{\lambda}^* = \frac{\underline{a}_s^T \, \underline{\underline{D}} \, \dot{\underline{\varepsilon}}}{\left(\underline{a}_s^T \, \underline{\underline{D}} \, \underline{b}_s - H \, \frac{\partial f^*}{\partial p_c} \, \underline{e}_p^T \, \underline{b}_s \right)} \tag{5.56}$$

A stress increment now follows from equation (5.46)

$$\dot{\underline{\sigma}} = \underline{\underline{D}} \, \dot{\underline{\varepsilon}} - \dot{\lambda}^* \, \underline{\underline{D}} \, \underline{b}_s - \tfrac{1}{2}(\dot{\lambda}_1 - \dot{\lambda}_2) \, 2G \, \underline{b}_d \tag{5.57}$$

The undetermined multiplier $(\dot{\lambda}_1 - \dot{\lambda}_2)$ should be such that the stress increment $\dot{\underline{\sigma}}$ remains in the triaxial plane, i.e.

$$\underline{b}_d^T \, \dot{\underline{\sigma}} = 0 \tag{5.58}$$

which after substitution of equation (5.57) yields

$$\tfrac{1}{2}(\dot{\lambda}_1 - \dot{\lambda}_2) = \frac{\underline{b}_d^T \, \dot{\underline{\varepsilon}}}{\underline{b}_d^T \, \underline{b}_d} \tag{5.59}$$

The complete stress strain relation for a stress state on a triaxial ridge can now be presented as follows

$$\dot{\underline{\sigma}} = \left[\underline{\underline{D}} - \underline{\underline{D}}_s^p - \underline{\underline{D}}_d^p \right] \dot{\underline{\varepsilon}} \tag{5.60}$$

where $\underline{\underline{D}}$ is the usual elasticity matrix according to Hooke and

$$\underline{\underline{D}}_s^p = \frac{\underline{\underline{D}} \, \underline{b}_s \, \underline{a}_s^T \, \underline{\underline{D}}}{\left(\underline{a}_s^T \, \underline{\underline{D}} \, \underline{b}_s - H \, \frac{\partial f^*}{\partial p_c} \, \underline{e}_p^T \, \underline{b}_s \right)} \tag{5.61}$$

will be called the triaxial plastic reduction matrix. Matrix $\underline{\underline{D}}_d^p$ will be referred to as the deviatoric plastic reduction matrix

$$\underline{\underline{D}}_d^p = 2G \, \frac{\underline{b}_d \, \underline{b}_d^T}{\underline{b}_d^T \, \underline{b}_d} \tag{5.62}$$

5.3.3 Simultaneous cap yielding and Coulomb yielding

Figure (5.9) shows a singular point at the intersection of a triaxial ridge in the cap surface and a triaxial ridge in the Mohr-Coulomb surface. The specification of the stress strain relation at this point involves the determination of four plastic multipliers. Instead of solving four simultaneous linear equations, we can make use of the triaxial - deviatoric decomposition, as introduced in the previous section

For the determination of the cap multiplier $\dot{\lambda}^*_c = \frac{1}{2}(\dot{\lambda}_{1c} + \dot{\lambda}_{2c})$ and the Mohr-Coulomb multiplier $\dot{\lambda}^*_m = \frac{1}{2}(\dot{\lambda}_{1m} + \dot{\lambda}_{2m})$, an extension of equation (5.50) can be used

$$\begin{aligned} \underline{a}^T_{sm} \underline{\underline{D}} \dot{\underline{\varepsilon}} - \dot{\lambda}^*_m \underline{a}^T_{sm} \underline{\underline{D}} \underline{b}_{sm} - \dot{\lambda}^*_c \underline{a}^T_{sm} \underline{\underline{D}} \underline{b}_{sc} &= 0 \\ \underline{a}^T_{sc} \underline{\underline{D}} \dot{\underline{\varepsilon}} - \dot{\lambda}^*_m \underline{a}^T_{sc} \underline{\underline{D}} \underline{b}_{sm} - \dot{\lambda}^*_c \underline{a}^T_{sc} \underline{\underline{D}} \underline{b}_{sc} + \frac{\partial f^*}{\partial p_c} \dot{p}_c &= 0 \end{aligned} \qquad (5.63)$$

where a subscript "m" has been added for the Mohr-Coulomb surface and "c" for the cap surface. Note that the extra term in each equation stems from the extension of the flow rule to deal with two active ridges. Substitution from expression (5.53) allows for the solution of the above system of equations. Subsequently, a stress increment follows from

$$\dot{\underline{\sigma}} = \underline{\underline{D}} \dot{\underline{\varepsilon}} - \dot{\lambda}^*_c \underline{\underline{D}} \underline{b}_{sc} - \dot{\lambda}^*_m \underline{\underline{D}} \underline{b}_{sm} - \dot{\underline{\sigma}}_d \qquad (5.64)$$

where

$$\dot{\underline{\sigma}}_d = \frac{1}{2}(\dot{\lambda}_{1c} - \dot{\lambda}_{2c})\, 2G\, \underline{b}_{dc} + \frac{1}{2}(\dot{\lambda}_{1m} - \dot{\lambda}_{2m})\, 2G\, \underline{b}_{dm} \qquad (5.65)$$

However, as $\underline{b}_{dc}$ and $\underline{b}_{dm}$ have the same direction, the last two terms can be added to yield a new equation with the undetermined parameter $\dot{\alpha}$

$$\dot{\underline{\sigma}} = \underline{\underline{D}} \dot{\underline{\varepsilon}} - \dot{\lambda}^*_c \underline{\underline{D}} \underline{b}_{sc} - \dot{\lambda}^*_m \underline{\underline{D}} \underline{b}_{sm} - \dot{\alpha}\, 2\, G\, \underline{b}_{d} \qquad (5.66)$$

Consequently, when condition (5.58) is applied to the above equation, we find for parameter $\dot{\alpha}$

$$\dot{\alpha} = \frac{\underline{b}^T_d \dot{\underline{\varepsilon}}}{\underline{b}^T_d \underline{b}_d} \qquad (5.67)$$

The stress strain relation for the singular point at the intersection of the two ridges now becomes

$$\dot{\underline{\sigma}} = \left[\underline{\underline{D}} - \underline{\underline{D}}^{p}_{mm} - \underline{\underline{D}}^{p}_{mc} - \underline{\underline{D}}^{p}_{cm} - \underline{\underline{D}}^{p}_{cc} - \underline{\underline{D}}^{p}_{d} \right] \dot{\underline{\varepsilon}} = \underline{\underline{D}}^{ep} \dot{\underline{\varepsilon}} \tag{5.68}$$

where matrices $\underline{\underline{D}}$ and $\underline{\underline{D}}^{p}_{d}$ are as in equation (5.60) and

$$\begin{aligned}
\underline{\underline{D}}^{p}_{mm} &= \frac{1}{d} \left(\underline{a}^{T}_{sc} \underline{\underline{D}} \underline{b}_{sc} - H \frac{\partial f^{*}}{\partial p_{c}} \underline{e}^{T}_{p} \underline{b}_{sc} \right) \underline{\underline{D}} \underline{b}_{sm} \underline{a}^{T}_{sm} \underline{\underline{D}} \\
\underline{\underline{D}}^{p}_{mc} &= - \frac{1}{d} \left(\underline{a}^{T}_{sm} \underline{\underline{D}} \underline{b}_{sc} \right) \underline{\underline{D}} \underline{b}_{sm} \underline{a}^{T}_{sc} \underline{\underline{D}} \\
\underline{\underline{D}}^{p}_{cm} &= - \frac{1}{d} \left(\underline{a}^{T}_{sc} \underline{\underline{D}} \underline{b}_{sm} \right) \underline{\underline{D}} \underline{b}_{sc} \underline{a}^{T}_{sm} \underline{\underline{D}} \\
\underline{\underline{D}}^{p}_{cc} &= \frac{1}{d} \left(\underline{a}^{T}_{sm} \underline{\underline{D}} \underline{b}_{sm} \right) \underline{\underline{D}} \underline{b}_{sc} \underline{a}^{T}_{sc} \underline{\underline{D}}
\end{aligned} \tag{5.69}$$

and in addition

$$d = \left(\underline{a}^{T}_{sm} \underline{\underline{D}} \underline{b}_{sm} \right) \left(\underline{a}^{T}_{sc} \underline{\underline{D}} \underline{b}_{sc} - H \frac{\partial f^{*}}{\partial p_{c}} \underline{e}^{T}_{p} \underline{b}_{sc} \right) - \left(\underline{a}^{T}_{sc} \underline{\underline{D}} \underline{b}_{sm} \right) \left(\underline{a}^{T}_{sm} \underline{\underline{D}} \underline{b}_{sc} \right) \tag{5.70}$$

The construction of matrix $\underline{\underline{D}}^{ep}$ in equation (5.68) becomes particularly simple when its constituents are computed relative to their own specific frame of reference and are transformed to a common global frame of reference afterwards. Triaxial plastic reduction matrices $\underline{\underline{D}}^{p}_{mm}$, $\underline{\underline{D}}^{p}_{mc}$, $\underline{\underline{D}}^{p}_{cm}$ and $\underline{\underline{D}}^{p}_{cc}$ can best be determined in the p,q-space, then be transformed to principal stress space and subsequently to general stress space. Note that during the first transformation we should differentiate between an extension ridge, with $\sigma_1 = \sigma_2$ and a compression ridge with $\sigma_2 = \sigma_3$. Deviatoric plastic reduction matrix $\underline{\underline{D}}^{p}_{d}$ is easily obtained by choosing the normal vector of the triaxial plane for vector $\underline{b}_{d}$, after which the obtained matrix should be transformed to general stress space.

At the compression point of the cap surface, the direction of plastic flow coincides with the hydrostatic axis

$$\dot{\underline{\varepsilon}}^{p} = \dot{\lambda} \underline{e}_{p} \tag{5.71}$$

Consequently, we only need to determine one plastic multiplier from the consistency condition

$$\frac{1}{3}\frac{\partial f}{\partial p}\,\underline{e}_p^T\,(\underline{\underline{D}}\,\dot{\underline{\varepsilon}} - \dot{\lambda}\,\underline{\underline{D}}\,\underline{e}_p) + \frac{\partial f}{\partial p_c}\,\dot{p}_c = 0 \tag{5.72}$$

Thus, we find for the stress strain relation

$$\dot{\underline{\sigma}} = \left[\,\underline{\underline{D}} - \underline{\underline{D}}_a^p\,\right]\dot{\underline{\varepsilon}} \tag{5.73}$$

where

$$\underline{\underline{D}}_a^p = \frac{K_s\,\underline{e}_p\,\underline{e}_p^T}{1 + \frac{H}{K_s}} \tag{5.74}$$

5.4 Finite increments of stress and strain

In finite element computations, finite increments of stress should be related to finite increments of strain. To this end, the differential stress strain law must be integrated over a finite time step. The implicit integration scheme, references (56,22,26,29,31) proves to be a robust scheme for integration of the Mohr-Coulomb model. In the case of a linear yield surface, like the Mohr-Coulomb surface, this scheme integrates exactly. Moreover, it dispenses with the need to determine the intersection of the stress path and the yield surface. This integration scheme will also be applied to the cap model. However, due to the non-linearity of the cap surface, implicit integration is not exact. Hence, a sub stepping scheme is introduced to prevent inaccurate integration.

5.4.1 Semi implicit integration

The general stress strain relation for a multi-surface plasticity model is given in section (2.5); here it will be repeated for convenience

$$\dot{\underline{\sigma}} = \underline{\underline{D}}\,\dot{\underline{\varepsilon}} - \underline{\underline{D}}\sum_{i=1}^{n}\dot{\lambda}_i\,\frac{\partial g_i}{\partial \underline{\sigma}} \tag{5.75}$$

Integration over a finite time step Δt yields

$$\Delta \underline{\sigma} = \underline{\underline{D}}\, \Delta \underline{\varepsilon} - \underline{\underline{D}} \sum_{i=1}^{n} \int_{t}^{t+\Delta t} \dot{\lambda}_i \frac{\partial g_i}{\partial \underline{\sigma}}\, dt \tag{5.76}$$

When the plastic potential function is part wise linear along a stress path, vector $\partial g/\partial \underline{\sigma}$ is independent of $\underline{\sigma}$ and, consequently, equation (5.76) may be replaced by

$$\Delta \underline{\sigma} = \underline{\underline{D}}\, \Delta \underline{\varepsilon} - \sum_{i=1}^{n} \Delta\lambda_i\, \underline{\underline{D}}\, \frac{\partial g_i}{\partial \underline{\sigma}} \tag{5.77}$$

When the plastic potential function is curved in principal stress space, this result can be interpreted as a one-step approximation of the integral. In fact, as pointed out by Vermeer[56], evaluation of vector $\partial g/\partial \underline{\sigma}$ at

$$\underline{\sigma} = \underline{\sigma}_0 + \Delta \underline{\sigma} \tag{5.78}$$

would yield an implicit integration. As this requires an iterative determination of the flow direction, instead we will evaluate vector $\partial g/\partial \underline{\sigma}$ at

$$\underline{\sigma}_e = \underline{\sigma}_0 + \underline{\underline{D}}\, \Delta \underline{\varepsilon} \tag{5.79}$$

Equation (2.66) shows that the plastic multipliers may be expressed by

$$\dot{\lambda}_k = \sum_{i=1}^{n} B^{-1}_{ki} \frac{\partial f}{\partial \underline{\sigma}}^{T}_{i}\, \underline{\underline{D}}\, \dot{\underline{\varepsilon}} \tag{5.80}$$

If f^e is defined as

$$f^e \equiv f\,(\underline{\sigma}_e) \tag{5.81}$$

then equation (5.80) can be simplified to

$$\dot{\lambda}_k = \sum_{i=1}^{n} B^{-1}_{ki}\, \dot{f}^e_i \tag{5.82}$$

which upon integration yields

$$\Delta\lambda_k = \sum_{i=1}^{n} B^{-1}_{ki} \, (f^e_i - \langle f^e_{io} \rangle) \tag{5.83}$$

Here the brackets $\langle f^e_{io} \rangle$ denote that $\langle f^e_{io} \rangle = 0$ for $f^e_{io} < 0$ and $\langle f^e_{io} \rangle = f^e_{io}$ when $f^e_{io} > 0$. This second contribution can be disregarded for a linear yield function, as the stresses $\underline{\sigma}_0$ will in such a case always yield $f^e_{io} \leq 0$. However, integration of a non-linear yield function involves some approximation and may result in $f^e_{io} > 0$.

An increment of stress is now obtained from combination of equations (5.77) and (5.83).

5.4.2 Incorporation of the model in a finite element program

Section 5.3.2 on the mathematical description of the model showed that a range of possibilities exists for the number of active yield surfaces. Consequently, when the model is applied in a finite element program, there should be some systematic way of finding the correct number of active surfaces and of the corresponding stress return scheme. Here, this practical aspect of the model will be discussed.

The increment of stress is computed with a two step return scheme[56,22]. First a test increment of stress is based on the assumption of elasticity

$$\underline{\sigma}_e = \underline{\sigma}_0 + \underline{\underline{D}} \, \underline{\Delta\varepsilon} \tag{5.84}$$

After this, this stress state is returned to the yield surface according to

$$\underline{\sigma} = \underline{\sigma}_e - \sum_{i=1}^{n} \Delta\lambda_i \, \underline{\underline{D}} \, \frac{\partial g_i}{\partial \underline{\sigma}} \tag{5.85}$$

Any stress state is completely determined when its principal values and principal directions are known. Due to the coaxiality of the flow rule, stress states $\underline{\sigma}$ and $\underline{\sigma}_e$ have the same principal directions. Consequently, the second phase of the integration sequence can conveniently be described in terms of principal stresses.

Section 5.3.1 on the generalization of the yield surface to principal stress

space shows that it is constructed from six similar surfaces. In fact, the only difference between those surfaces is obtained by rearranging the principal stresses in definition (5.38). This leads to a second simplification of the return scheme, namely the treatment of only one yield surface and its bounding ridges. To this end, the principal stresses of stress state $\underline{\sigma}_e$ are computed and rearranged, such that $\sigma_3 > \sigma_2 > \sigma_1$. In this case, the active yield function is described by

$$f(\bar{p},\bar{q}) = 0 \tag{5.86}$$

in which

$$\begin{aligned} \bar{p} &= -\frac{1}{3}(\sigma_1 + \sigma_2 + \sigma_3) \\ \bar{q} &= (\sigma_2 - \sigma_1) + \frac{3 + \sin\phi}{3 - \sin\phi}(\sigma_3 - \sigma_2) \end{aligned} \tag{5.87}$$

Figure (5.11) shows this function in deviatoric stress space, where it is a line. The triaxial ridges form the intersections with the neighbouring surfaces. The compression ridge is found from the intersection with the surface based on

$$\bar{q} = (\sigma_3 - \sigma_1) + \frac{3 + \sin\phi}{3 - \sin\phi}(\sigma_2 - \sigma_3)\ , \tag{5.88}$$

whereas the extension ridge follows from the intersection with the surface based on

$$\bar{q} = (\sigma_1 - \sigma_2) + \frac{3 + \sin\phi}{3 - \sin\phi}(\sigma_3 - \sigma_1) \tag{5.89}$$

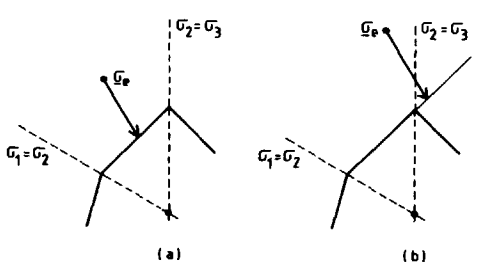

Figure 5.11. Stress return to yield surface. (a) regular surface. (b) false return.

In the remainder of this section, a rough description will be given of the subsequent steps in the procedure for finding the correct stress correction of equation (5.85). Here a method of reduction of possibilities is followed.

First, the Mohr-Coulomb model is treated, yielding a temporary stress result $\underset{\sim}{\sigma}_m$. This value is tested for its validity by computing $f_c(\bar{p}_m, \bar{q}_m)$. If $f_c < 0$, then the result $\underset{\sim}{\sigma}_m$ is accepted, otherwise the cap surface becomes active. Now, the stress $\underset{\sim}{\sigma}_e$ is returned to the regular cap surface. Again this may succeed, as in Figure (5.11a), or fail, as in Figure (5.11b). Upon failure, a triaxial ridge is treated. After this, a test is made for the Mohr-Coulomb surface, which may lead to a return to a deviatoric ridge or, in succession, even to a singular point at the intersection of ridges, Figure (5.9). This procedure is continued until a satisfactory stress increment is obtained.

5.4.3 Sub-stepping scheme

It was observed in section 5.4.1. that the implicit integration scheme enables exact integration of constitutive equations based on linear plastic potential functions. However, the cap yield surface is not linear and, as a result, the accuracy of integration will depend on the size of a strain increment. Consequently, this size should be limited to an acceptable level. For this purpose, a sub-stepping scheme is introduced.

This scheme consists of two parts. As there is no simple equation describing the intersection of the stress path and the yield surface, the strains are incremented in the first part until a yield surface is reached. In the second part, the plastic branch of the stress path is treated.

The step size in the second part of the scheme is determined on the basis of two criteria. The first criterion judges the drift from the yield surface. It computes the value of the normalized yield function after a trial return to the cap surface

$$\varepsilon_1 = f_c(\bar{p}_t, \bar{q}_t) \;/\; p_c^2 \tag{5.90}$$

Here yield function f_c follows from equation (5.10). A suitable step size is now obtained from the assumption that this error reduces linearly with the step size.

Equation (5.77) assumed the normal to the plastic potential surface to be

constant along the stress path. To judge the accuracy of this assumption, a second criterion is employed

$$\varepsilon_2 = 1 - \underline{n}_0^T \, \underline{n}_e \tag{5.91}$$

where $\underline{n}_0$ is the normal to the surface at the initial stress state and $\underline{n}_e$ is the normal at the stress state $\underline{\sigma}_e$. Obviously, for a linear plastic potential function both vectors coincide and, as a result, the error vanishes.

A suitable step size for the sub-increment of strain is now found from

$$\delta\underline{\varepsilon} = \Delta\underline{\varepsilon} \; / \; \mu \quad ; \quad \mu = \max \left\{ \frac{\varepsilon_1}{\bar{\varepsilon}_1} \, , \, \frac{\varepsilon_2}{\bar{\varepsilon}_2} \, , \, 1 \right\} \tag{5.92}$$

Parameters $\bar{\varepsilon}_1$ and $\bar{\varepsilon}_2$ are preset tolerances for the error measures and "max" denotes the "maximum value of". Note that μ is rounded off to the nearest integer value. Typical values for the preset tolerances are in the order of five per cent.

5.5 SIMULATION OF A CIRCULAR FOOTING TEST

The K_0-cap model, as developed in the previous sections, will be used in the simulation of a footing indentation test. Data for this problem are obtained from the tests by Labanieh in Grenoble[77].

5.5.1 Interpretation of triaxial test data

The material used in the footing test is Hostun sand with a D_{50} of 0.63 mm. Maximum and minimum void ratios are $e_{max} = 0.79$ and $e_{min} = 0.52$ respectively. The test was performed on loose sand with a void ratio of $e = 0.74$, which implies a relative density of RD = 19 per cent. From this it follows that the initial density of the sand in the test is $\gamma = 15.4$ kN/m^3.

Labanieh reports a series of triaxial tests at different confining pressures. Figure (5.12) shows the results in the form of diagrams for axial strain versus axial stress and axial strain versus radial strain. The first yields information on the friction angle ϕ and Young's modulus E, whereas the second gives Poisson's ratio ν and the dilation angle ψ.

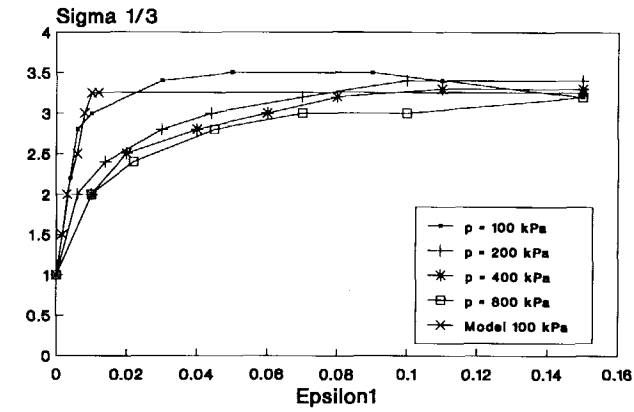

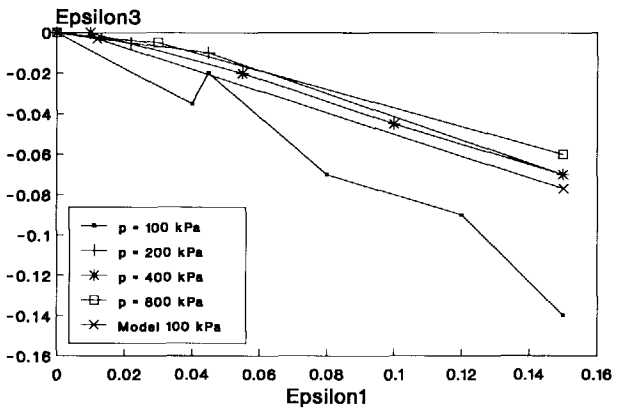

Figure 5.12. Triaxial test results for Hostun sand.

Friction angle ϕ:

This parameter is determined from the value of σ_1/σ_3 at collapse

$$\frac{1+\sin\phi}{1-\sin\phi} = \left(\frac{\sigma_1}{\sigma_3} \right)_u \tag{5.93}$$

From this it follows that values of ϕ range from $\phi = 33^\circ$ at low confining pressures to $\phi = 30^\circ$ at high confining pressures. For the present simulation a value of $\phi = 32^\circ$ is chosen, in view of the fact that pressures in the test will be fairly low.

Dilation angle ψ:

The ε_1, ε_3-curve can be used to obtain a value for the dilation angle. Inspection of the Mohr-Coulomb model shows that at failure

$$\frac{-2+\sin\psi}{1+\sin\psi} = \left(\frac{\dot{\varepsilon}_1}{\dot{\varepsilon}_3} \right)_u \tag{5.94}$$

Except for the test at a confining pressure of 100 kPa, all of the tests thus yield a value of ψ in the order of $\psi = 0^\circ$ to $\psi = 2^\circ$. This agrees well with the general finding that for quartz sand $\psi \cong \phi - 30^\circ$. The test at a pressure of 100 kPa yields a value of $\psi = 11^\circ$, which is completely out of line. Consequently, this value is rejected. Henceforth a value of $\psi = 2^\circ$ will be chosen.

Young's modulus E:

The initial slope of the stress-strain curve yields a value of Young's modulus

$$E_0 = \frac{(\sigma_1/\sigma_3)^{\cdot}_0}{\dot{\varepsilon}_1} \tag{5.95}$$

Inspection of the test results shows however that this value is difficult to determine. In addition, it is a function of confining pressure. Instead of determining this dependency in detail, the relation of equation (5.6) is postulated

$$E = E_{0a} \sqrt{\frac{p}{p_a}} \tag{5.96}$$

Subsequently, E_{0a} can be fitted to the available data. Thus, we obtain a value of $E_{0a} \cong 16$ MPa.

Poisson's ratio ν:

Poisson's ratio relates the axial strain to the radial strain in the following way

$$\nu_0 = - \left(\frac{\dot{\varepsilon}_3}{\dot{\varepsilon}_1} \right)_0 \tag{5.97}$$

From the tests it follows that ν_0 is in the order of $\nu_0 = 0.0$ to $\nu_0 = 0.2$. In the simulation the average value of $\nu_0 = 0.1$ will be chosen.

Additional parameters:

The parameter λ^*/κ^*, which was introduced in equation (5.5), can be determined from an isotropic compression test, where it relates the total strain increment to the recoverable strain increment. Unfortunately, no reliable data are available. Literature on compression tests for loose sand[78,79] shows that a value of $\lambda^*/\kappa^* \cong 1.7$ is quite realistic. The coefficient of lateral earth pressure, K_0, is reported to be $K_0 \cong 0.4$. Finally, a choice has to be made for the overconsolidation ratio, OCR. Taking into account that the sand was not pre-loaded before the test, we arrive at an OCR of 1.0.

Interface parameters:

Special interface elements will be applied at the contact between the footing and the sand. The elastic parameters k_s and k_n of equation (4.2) are chosen in such a way that the elastic compression and slip of the interface remain well within one per cent of the elastic footing indentation. The interface friction angle ϕ_i and dilation angle ψ_i follow from the tests by Plytas[80]. Thus, average values of $\phi_i = 28^\circ$ and $\psi_i = 0^\circ$ are found. Note that the tests display a bigger initial value of ψ_i. After some plastic distortion, however, this dilation rapidly reduces to zero. As the present interface model does not allow for a variable value of ψ_i, the low residual value of $\psi_i = 0^\circ$ is adopted.

Figure (5.12) shows the collected data of the four triaxial tests and a prediction with the K_0-cap model on the basis of the parameters in Table 5.1.

Table 5.1 Soil parameters for loose Hostun sand

parameter	value	unit
D_{50}	0.63	mm
e-max	0.79	
e-min	0.52	
e	0.74	
γ	15.4	kN/m3
E_{oa}	16	Mpa
ν_o	0.1	
ϕ	32	
c	0	kPa
ψ	2	
λ/κ	1.7	
K_o	0.4	
OCR	1.0	
k_s	10	GPa/m
k_n	10	GPa/m
ϕ_i	28	
c_i	0	kPa
ψ_i	0	

5.5.2 Simulation versus test results

The dimensions of the circular footing and the sand pit together with the finite element mesh are shown in Figure (5.13). The total sand pit has been modelled so as to rule out any possible boundary effects other than of the true boundaries of the pit.

The results for the test and the simulation are given in Figure (5.14). As can been seen from this figure, a remarkable fit is obtained up to displacement of about 10 mm. After this, the simulation computes collapse, whereas the test shows an increase of the force. It should be noted, however, that the present analysis does not include large deformation effects. Such effects are of major importance in footing problems on sandy soils. The simulation will therefore be repeated in the next chapter, where large deformation effects are discussed.

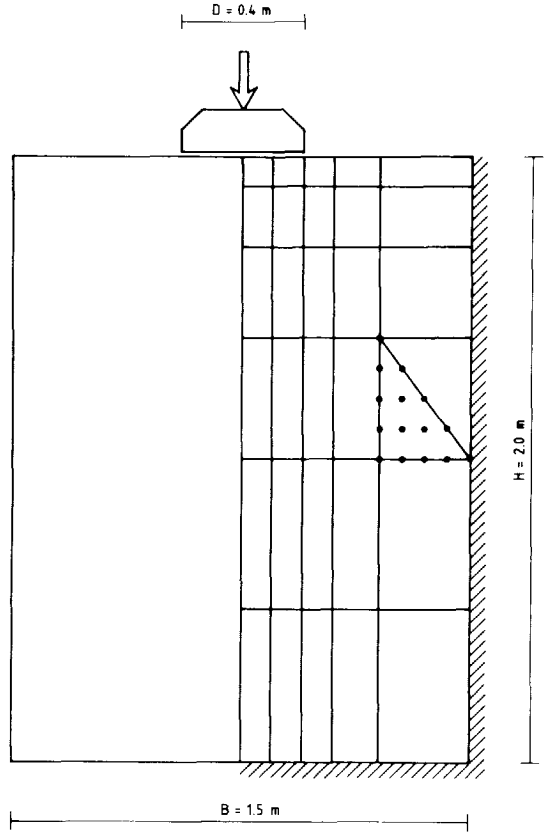

Figure 5.13. Finite element mesh for simulation of circular footing test.

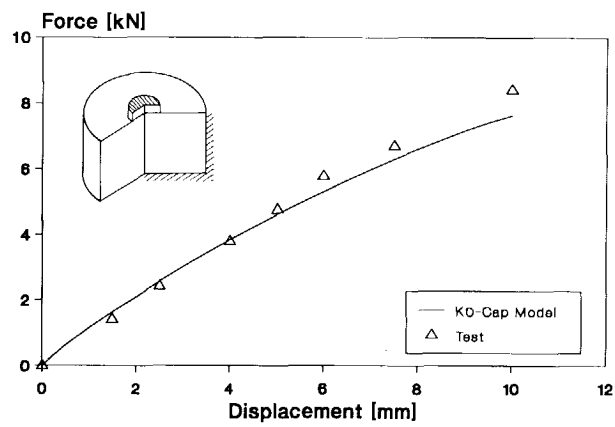

Figure 5.14. Load-displacement curve for circular footing test on sand.

6. LARGE DEFORMATION EFFECTS

Large deformation effects are of major importance in problems involving slender structural members like beams, plates and shells. Indeed, phenomena like buckling and stiffening could not be described without considering such effects, references (81,14,82,19). Soil bodies, however, are far from slender and, consequently, most finite element formulations tacitly disregard changes in geometry. However, it will be shown that in some cases of soil deformation incorporation of large deformation effects will enhance the quality of predictions.

This chapter will start by analyzing the problem of a bending cantilever to validate the updated Lagrangian technique as described in the first chapter. Subsequently, this technique is used in the analysis of the footing problem of Chapter 5, after which the difference is discussed between the results from a small deformation analysis and a large deformation analysis respectively.

The importance of large deformation effects in the problem of reinforced embankments on soft soil will also be studied. To this end, a membrane element is formulated. After validation, it is used in the analysis of embankment stability. Differences between small and large deformation analyses for both a non-reinforced and a reinforced embankment are discussed.

6.1 Large deflection of a bending cantilever

The problem of the large deflection of a slender beam was first discussed by Euler and Lagrange[83]. Here, the special case of a cantilever loaded at its end will be considered, as shown in Figure (6.1). The load does not change its direction during application. The theoretical solution to this problem involves so-called elliptic integrals, which have to be solved numerically[84].

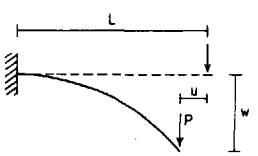

Figure 6.1. Horizontal cantilever with a vertical point load.

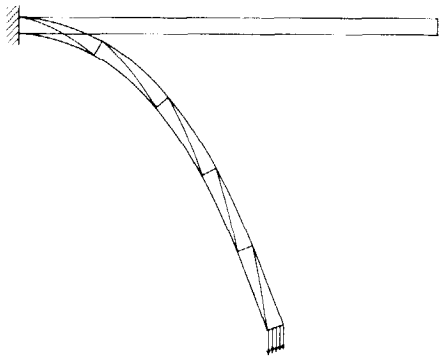

Figure 6.2. True deformation of finite element mesh for cantilever problem.

Figure (6.2) shows the deformed finite element mesh for this cantilever problem. To the left the cantilever is fully clamped, whereas to the right it is loaded by a traction. Note that this picture shows the true deformation, in the sense that both the mesh and the deformation are scaled to the same degree.

Figure (6.3) shows that the computed load-deflection curves are in close agreement with the theoretical solution. A small deviation occurs in the curve for the vertical displacement at high load levels: the finite element analysis computes a slightly larger deflection. This larger deflection can be attributed to the extension of the beam. The theoretical solution disregards this extension, whereas it becomes noticeable in the finite element solution. The importance of this effect is reduced when the slenderness of the beam increases. A remarkable fit is obtained for the horizontal displacement. It should be noted that this cantilever problem involves large rotations and displacements, whilst strains remain relatively small.

6.2 Simulation of a circular footing test

Section 5.5 described the small deformation analysis of a circular footing test. It was observed that the numerical result was in close agreement with the test up to a displacement of about 10 mm. After that, the numerical

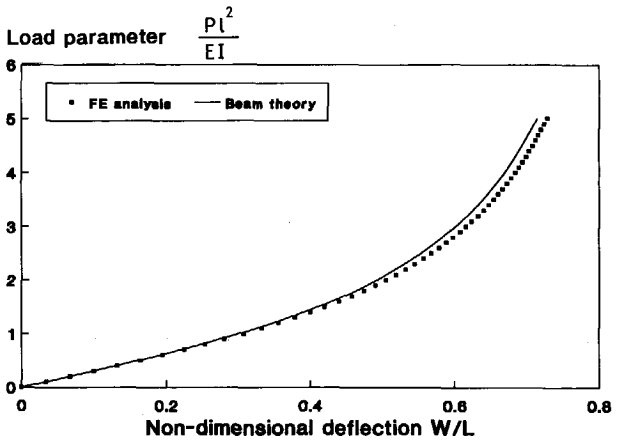

(a)

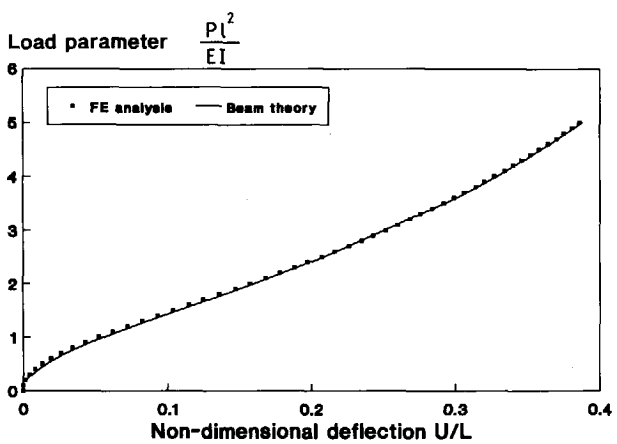

(b)

Figure 6.3. Large deformation of a cantilever. (a) vertical deflection. (b) horizontal deflection.

analysis predicted collapse, whereas the test showed a steady increase of the load. Here the analysis is repeated, this time taking large deformation effects into account. The load-displacement curves for both analyses are shown in Figure (6.4). For displacements up to 5 mm both curves virtually coincide. After this, the curves begin to drift apart. Here the large deformation analysis predicts a somewhat stiffer response. This difference becomes even more pronounced after a displacement of about 10 mm. Here, the large deformation analysis computes a slowly increasing load, whereas the small deformation analysis computes collapse. Hence, taking large deformation effects into account proves to be important in the case of a footing penetrating into loose sand. Due to the significant penetration, there will be a rapid development of an overburden load, which in turn causes an increase of the bearing capacity. In very dense sands, the penetration up to collapse will be much lower and, as a result, the increase of the bearing capacity will first develop in the post-collapse regime. In soft clays, on the other hand, deformations may be large, but the dependency of collapse loads on the overburden stress is less pronounced.

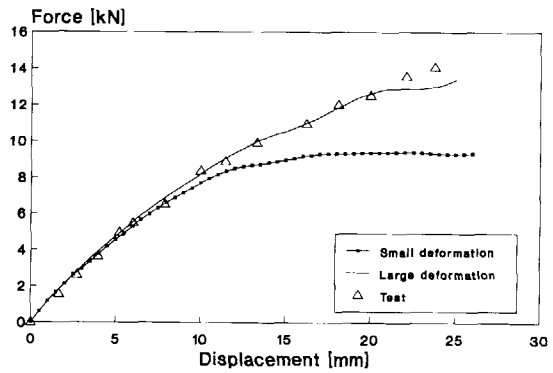

Figure 6.4. Load-displacement curves for circular footing test on sand.

6.3 Analysis of geotextile-reinforced soils

Geotextiles are used, amongst other things, to improve the stiffness and stability of soil bodies. Applications can be found in the reinforcement of unpaved roads and embankments[85]. The evaluation of deformation and stability of bodies containing geotextile calls for improved methods of analysis. Several such methods have been proposed in the past[86-92]. It has been shown that conventional limit equilibrium methods for slopes and trenches can be extended to take reinforcement into account[91,92]. The determination of deformation, however, seems to be more of a problem. For unpaved roads approximations are frequently based on beam-type calculations[88-90]. Naturally, this method can only be used in a limited number of cases. Unfortunately, no simple method exists for reinforced embankments.

Here, a finite element will be developed for the simulation of geotextile reinforcement. This element can be used to obtain detailed information on deformations, stability and textile forces.

6.3.1 Formulation of a large deformation membrane element

Figure (6.5) shows an axisymmetric membrane element and the stresses which act on it. The contribution of this element to the virtual work equation (2.7)

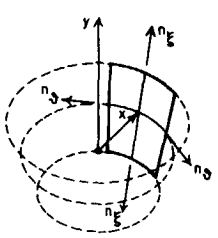

Figure 6.5. Stresses acting on an axisymmetric membrane element.

can conveniently be written in terms of those stresses and the associated strains

$$\delta W_m = \int_S (n_\xi \delta e_\xi + n_\vartheta \delta e_\vartheta)\, dS \tag{6.1}$$

where S is the surface of the element. The virtual elongations δe_ξ and δe_ϑ depend on the incremental length dl, its position in x-direction and the corresponding virtual displacement δu_x in the following way

$$\delta e_\xi = \frac{\delta(dl)}{dl} \quad ; \quad \delta e_\vartheta = \frac{\delta u_x}{x} \tag{6.2}$$

The virtual elongation δe_ξ can be related to the virtual displacements δu_x and δu_y by considering the definition of dl

$$dl = J\, d\xi \quad ; \quad J = \sqrt{\left(\frac{\partial x}{\partial \xi}\right)^2 + \left(\frac{\partial y}{\partial \xi}\right)^2} \tag{6.3}$$

Applying a variation to dl then yields

$$\delta(dl) = J^{-1}\left\{ \frac{\partial \delta u_x}{\partial \xi}\frac{\partial x}{\partial \xi} + \frac{\partial \delta u_y}{\partial \xi}\frac{\partial y}{\partial \xi} \right\} d\xi \tag{6.4}$$

from which it follows that

$$\delta e_\xi = J^{-2}\left\{ \frac{\partial \delta u_x}{\partial \xi}\frac{\partial x}{\partial \xi} + \frac{\partial \delta u_y}{\partial \xi}\frac{\partial y}{\partial \xi} \right\} \tag{6.5}$$

The equation of continued equilibrium (2.8) should now be supplemented with a contribution from the membrane element. To this end, the material rate of change of expression (6.1) is determined

$$\begin{aligned} (\delta W_m)^\cdot &= \int_S \{\dot{\underline{n}}^T \delta \underline{e} + \underline{n}^T \frac{(dS)^\cdot}{dS} \delta \underline{e} + \underline{n}^T (\delta \underline{e})^\cdot\}\, dS \\ &= \delta \dot{W}_{m1} + \delta \dot{W}_{m2} + \delta \dot{W}_{m3} \end{aligned} \tag{6.6}$$

where the stresses and strains are assembled in a vector. The first term in equation (6.6) stems from the increase of stress due to elongation of the membrane, whereas the second and third terms stem from geometry changes. Each of the above terms will now be elaborated.

The first term in equation (6.6) can be related to the strain rate by means of a constitutive relation. Here a simple relationship of the form

$$\dot{\underline{n}} = \underline{\underline{D}}\ \dot{\underline{e}} \tag{6.7}$$

will be adopted, in which stiffness matrix $\underline{\underline{D}}$ is expressed by

$$\underline{\underline{D}} = \begin{bmatrix} D_{\xi\xi} & D_{\xi\vartheta} \\ D_{\vartheta\xi} & D_{\vartheta\vartheta} \end{bmatrix} \tag{6.8}$$

The relation between the strain rate vector $\dot{\underline{e}}$ and the nodal velocities $\dot{\underline{a}}$ is determined by the strain interpolation matrix $\underline{\underline{B}}$

$$\dot{\underline{e}} = \underline{\underline{B}}\ \dot{\underline{a}} \tag{6.9}$$

where

$$\underline{\underline{B}} = \begin{bmatrix} J^{-2}\,\dfrac{\partial x}{\partial \xi} & J^{-2}\,\dfrac{\partial y}{\partial \xi} \\ x^{-1} & 0 \end{bmatrix} \underline{\underline{N}},_{\xi} \tag{6.10}$$

Note that for a 5-noded membrane element the definition of the displacement interpolation matrix $\underline{\underline{N}}$ differs slightly from the one given in equation (4.18) for the interface elements. Here this definition reads

$$\underline{\underline{N}} = \begin{bmatrix} N_1 & 0 & N_2 & 0 & \cdots & N_5 & 0 \\ 0 & N_1 & 0 & N_2 & \cdots & 0 & N_5 \end{bmatrix} \tag{6.11}$$

where the shape functions N_1 to N_5 are given in equation (4.19). Equation (6.9) also holds for the vector of virtual strains and the virtual nodal displacements, so we may write

$$\delta\underline{e} = \underline{\underline{B}}\ \delta\underline{a} \tag{6.12}$$

Substitution of relations (6.7) to (6.12) in the first term of equation (6.6) yields the discretized expression

$$\delta\dot{W}_{m1} = \delta\underline{a}^{T}\ \underline{\underline{K}}_{m1}\ \dot{\underline{a}} \tag{6.13}$$

where matrix $\underline{\underline{K}}_{m1}$ is the material tangent stiffness matrix for the membrane element

$$\underline{\underline{K}}_{m1} = \int_S \underline{\underline{B}}^T \, \underline{\underline{D}} \, \underline{\underline{B}} \, dS \tag{6.14}$$

The second term in equation (6.6) contains the stretch of the membrane

$$\frac{(dS)^{\cdot}}{dS} = \dot{e}_{\xi} + \dot{e}_{\vartheta} \equiv \underline{i}^T \, \dot{\underline{e}} \tag{6.15}$$

Combination of equations (6.9-6.12) and (6.15) yields after substitution in equation (6.6)

$$\delta \dot{W}_{m2} = \delta \underline{a}^T \, \underline{\underline{K}}_{m2} \, \dot{\underline{a}} \tag{6.16}$$

where

$$\underline{\underline{K}}_{m2} = \int_S \underline{\underline{B}}^T \, \underline{n} \, \underline{i}^T \, \underline{\underline{B}} \, dS \tag{6.17}$$

Evaluation of the third term in equation (6.6) is somewhat more involved, as it requires the material rate of change of the virtual strain vector. A straightforward derivation shows that the first component of this vector can be expressed as

$$(\delta e_{\xi})^{\cdot} \equiv \left\{ \frac{\delta(dl)}{dl} \right\}^{\cdot} = \delta \underline{u}^T_{,\xi} \, \underline{\underline{P}} \, \dot{\underline{u}}_{,\xi} \tag{6.18}$$

where matrix $\underline{\underline{P}}$ describes the local geometry of the line element being considered,

$$\underline{\underline{P}} = J^{-2} \begin{bmatrix} \left\{ 1 - 2 J^{-2} \left(\frac{\partial x}{\partial \xi} \right)^2 \right\} & \left\{ - 2 J^{-2} \frac{\partial x}{\partial \xi} \frac{\partial y}{\partial \xi} \right\} \\ \left\{ -2 J^{-2} \frac{\partial x}{\partial \xi} \frac{\partial y}{\partial \xi} \right\} & \left\{ 1 - 2 J^{-2} \left(\frac{\partial y}{\partial \xi} \right)^2 \right\} \end{bmatrix} \tag{6.19}$$

The second component yields the simple expression

$$(\delta e_{\vartheta})^{\cdot} \equiv \left\{ \frac{\delta u x}{x} \right\}^{\cdot} = \delta \underline{u}^T \, \underline{\underline{Q}} \, \dot{\underline{u}} \tag{6.20}$$

Matrix $\underline{\underline{Q}}$ only depends on the radial position of the element

$$\underline{\underline{Q}} = \begin{bmatrix} -x^{-2} & 0 \\ 0 & 0 \end{bmatrix} \tag{6.21}$$

Now, the third term of equation (6.6) can be discretized by introducing finite element shape functions (2.81) into expressions (6.18) and (6.20)

$$\delta \dot{W}_{m3} = \delta \underline{a}^T \underline{\underline{K}}_{m3} \dot{\underline{a}} \tag{6.22}$$

where

$$\underline{\underline{K}}_{m3} = \int_S (n_\xi \underline{\underline{N}}_{,\xi}^T \underline{\underline{P}} \underline{\underline{N}}_{,\xi} + n_\vartheta \underline{\underline{N}}^T \underline{\underline{Q}} \underline{\underline{N}}) \, dS \tag{6.23}$$

The total large deformation stiffness matrix for the membrane element is found from adding the three derived sub-matrices

$$\underline{\underline{K}}_m = \underline{\underline{K}}_{m1} + \underline{\underline{K}}_{m2} + \underline{\underline{K}}_{m3} \tag{6.24}$$

In Appendix C it is shown that this matrix contains the geometric stiffness matrix for a truss element[93] as a special case.

6.3.2. Large deflection of a pre-stressed membrane

The closed-form solution for the large deflection of a pre-stressed membrane can be used to validate the element of the previous section. When considering the problem of Figure (6.6), equilibrium yields the equation

$$F = 4 \, n_\xi \, u/l \tag{6.25}$$

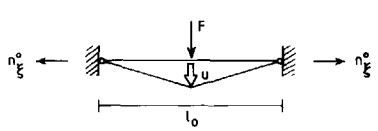

Figure 6.6. Large deflection of a pre-stressed membrane.

Constitutive relation (6.7) reduces in the case of a non-contracting, plane strain membrane to the expression

$$\dot{n}_\xi = D_{\xi\xi}\, \dot{l}/l \tag{6.26}$$

which after integration yields

$$n_\xi = D_{\xi\xi}\, \ln(l/l_0) + n_\xi^0 \tag{6.27}$$

Here, l_0 is the original length of the membrane and n_ξ^0 is the initial stress. The load-deflection relation is obtained by combining equations (6.25) and (6.27)

$$F = 4\, D_{\xi\xi}\, u/l\, \ln(l/l_0) + 4\, n_\xi^0\, u/l \tag{6.28}$$

This relation, together with the finite element result, is plotted in Figure (6.7). Note that for this analysis the special ratio of

$$D_{\xi\xi}/n_\xi^0 = \frac{4 - \sqrt{2}}{\sqrt{2}\, \ln \sqrt{2}} \tag{6.29}$$

has been chosen as it exactly yields a force of $F = 4\, n_\xi^0$ at a non-dimensional deflection of $u/l = 0.5$.

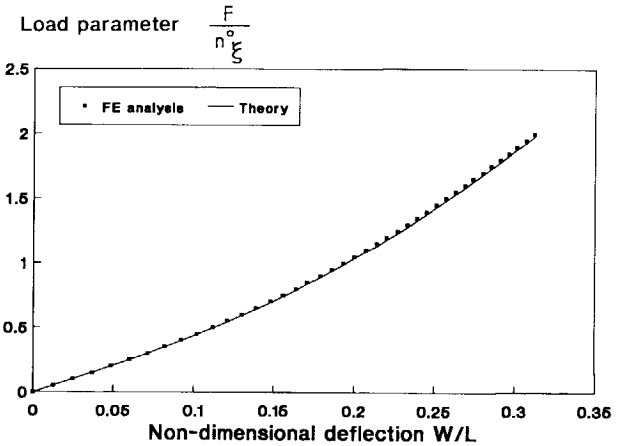

Figure 6.7. Load-displacement curve for a pre-stressed membrane.

6.4 Failure of a geotextile-reinforced embankment

In 1979, a test embankment was constructed in the Netherlands near the town of Almere[94]. The objective of this test was to measure the influence of geotextile reinforcement on the short term stability of an embankment on soft soil. To this end, two 60 metre long embankments were constructed on top of a soft clay deposit, Figure (6.8), one of which was reinforced, whilst the other one served as an non-reinforced reference. Shortly after completion, hydraulic filling of the sections started. Failure of the reinforced section was reported after 24 hours of filling, at which point the fill had reached a height of about 3 metres. The mechanism observed was one of circular sliding. The non-reinforced section failed at a height of 1.75 metres.

In the remainder of this section, a finite element analysis will be made of the above test. The results will be compared against observations.

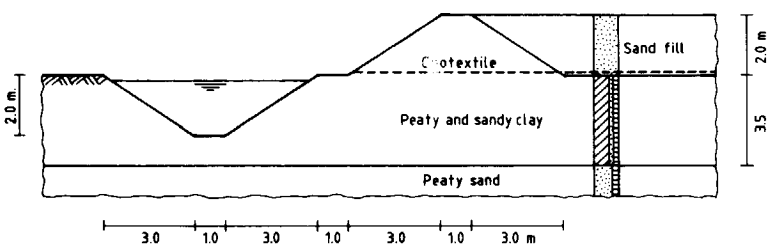

Figure 6.8. A geotextile-reinforced embankment on soft soil.

6.4.1. Schematizations

A CPT test indicated that the subsoil consisted of a 3.5 metre thick deposit of sandy and peaty clay, with a mean cone resistance of q_c = 150 kPa. Assuming a cone factor of 15, the undrained shear strength can be estimated to be c_u = 10 kPa. This layer is followed by a stiff and strong layer of peaty, medium coarse sand, which will serve as the lower boundary of the finite element mesh. Additional parameters for the clay layer are taken to reflect the soft, undrained response

$$\phi_u = \psi_u = 0, \qquad G = 350 \text{ kPa}, \qquad \nu_u = 0.49, \qquad \gamma = 20 \text{ kN/m}^3$$

As no tests were performed on the filling sand, some plausible values have to be chosen. Assuming a fully saturated medium course sand of loose density, we arrive at the following set of parameters

$G_{50} = 6000(p/p_a)^{0.5}$ kPa, $\nu'_{50} = 0.35$, $\phi' = 32^\circ$
$\psi' = 2^\circ$, $c' = 1$ kPa, $\gamma_{wet} = 20$ kN/m^3

where p_a is a pressure of 1 atm. in the appropriate unit of the isotropic pressure p. A dash is used to indicate effective properties relating to the soil skeleton.

The embankment was reinforced with the Stabilenka 200 polyester reinforcing mat[94], which has a stress strain curve as shown in Figure (6.9). It should be noted, however, that the material also shows a considerable creep. This creep effect will be disregarded, as only short term effects are considered. Due to its woven structure, the textile may also be expected to contract in the out-of-load direction. However, due to the lack of data on this contraction, it will be disregarded in the present analysis.

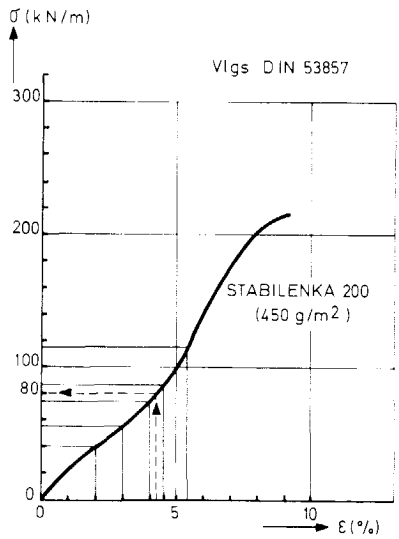

Figure 6.9. Stress-strain curve for Stabilenka 200 reinforcing mat[94].

The complete set of parameters for the textile is as follows

stiffness $D_{\xi\xi}$ = 1900 kN/m, Poisson's ratio ν = 0
tensile strength $\bar{n}_{\xi}$ = 200 kN/m

Special interface elements will be applied along both sides of the textile. The soil parameters of the interfaces relate to those from the adjacent soil. To reflect the effect of high distortion and the smoothness of the textile, the strength parameters are reduced to the following values

clay-textile interface	$\phi_u = 0^\circ$,	$\psi_u = 0^\circ$,	$c_u = 5$ kPa
sand-textile interface	$\phi' = 17^\circ$,	$\psi' = 0^\circ$,	$c' = 0.5$ kPa

Figure (6.10) shows the finite element mesh for all analyses of the embankment problem. At first sight, the mesh may seem to be extremely over-sized. However, it was decided to model the full length of the geotextile. In this way, the textile can be pulled out from the soil without experiencing any spurious constraints.

The filling process is modelled by gradually increasing the weight of the fill, which consists of a fixed layer of elements. At any point in the computation, the applied height of the fill follows from the expression

$$h = \frac{\gamma}{\gamma_{true}} h_{fixed} \qquad (6.30)$$

where γ is the applied weight, γ_{true} is the true weight of the fill and h_{fixed} is the thickness of the element layer.

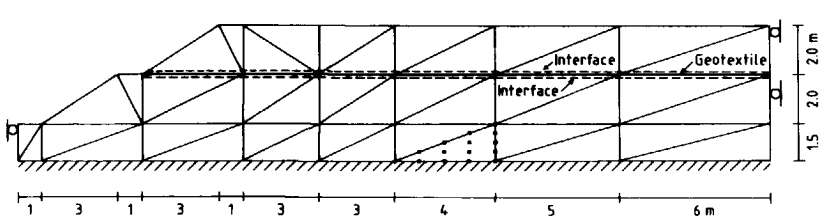

Figure 6.10. Embankment finite element mesh with geotextile and interfaces.

6.4.2. Discussion of the results

The test results do not incorporate measured load-displacement curves for particular points of the geometry. As a concequence, we cannot present a detailed comparison of measurements and computations. The only data available are for the occurrence of failure and the textile forces. The non-reinforced embankment was observed to fail at a filling height of 1.75 metres and the reinforced embankment failed at 3 metres.

The load-displacement curves for the large deformation finite element analyses of the embankment, Figure (6.11), show a general agreement with the test results. However, a small deformation analysis of the non-reinforced embankment, Figure (6.12), gives collapse at an embankment height of 1.3 metres, which is some 30 per cent lower than the observed value. Hence, it becomes clear that in this case large deformation effects are of considerable importance. As failure progresses, the limit load slowly increases. This phenomenon is due to the stabilizing effect of circular sliding, Figures (6.13a) and (6.13b). In general, embankments on very soft soils will experience considerable displacements up to impending failure, so that a large deformation analysis is of importance. By contrast, embankments on a stiff subsoil will show a more sudden collapse. Here, stabilizing effects will first occur in the post-peak regime.

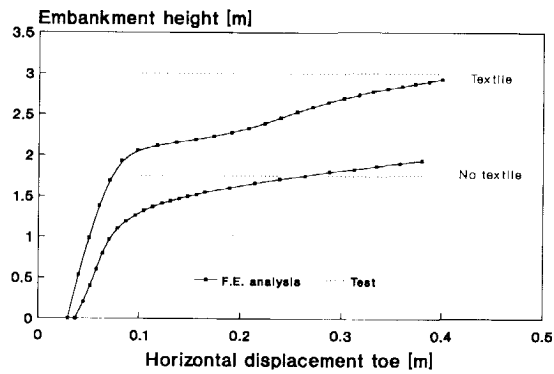

Figure 6.11. Load-displacement curves for two embankments loaded by a sand fill.

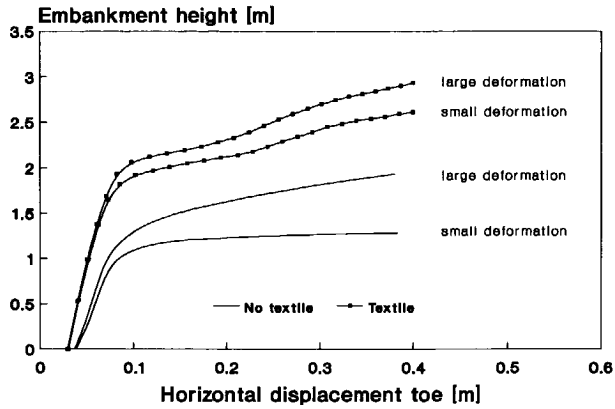

Figure 6.12. Large deformation effects in the analysis of two embankments.

The curves for the reinforced embankment display a much stiffer and stronger response. Both strength and stiffness increase by a factor of about 1.5 to 2.0. In this case the influence of large deformation effects seems to be less pronounced. An explanation can be found in the failure mechanism for this case, Figures (6.13c) and (6.13d). Again a curved slip surface develops in the retaining part of the embankment. However, after this, the textile is dragged along the soft clay layer, carrying the fill on top. In this case the associated build-up of the force in the textile dominates the response after development of the curved slip surface.

The deformed meshes for the four computations, Figure (6.14), show that in the reinforced embankment two competing mechanisms exist. The first resembles that of the non-reinforced embankment, whereas the second causes the retaining part of the embankment to move horizontally towards the ditch. The slip along the textile is clearly visible.

The normal stresses and shear stresses in the interface elements at both sides of the textile are depicted in Figure (6.15). In the result for the small deformation analysis, Figure (6.15a), the normal stresses below and above the textile coincide exactly. In this case the membrane element cannot carry any transversal load, as its curvature is disregarded. In the large deformation result, a slight difference is visible between the normal stresses

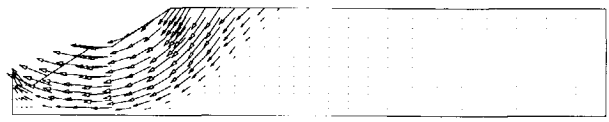

(a) non-reinforced embankment, small deformation analysis

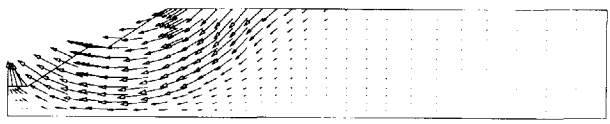

(b) non-reinforced embankment, large deformation analysis

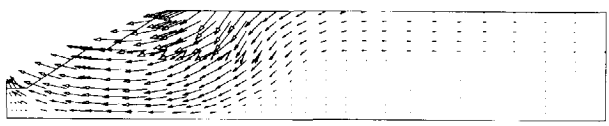

(c) reinforced embankment, small deformation analysis

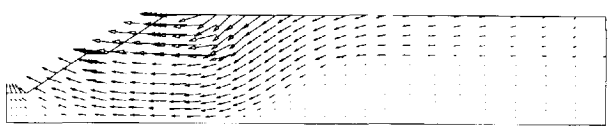

(d) reinforced embankment, large deformation analysis

Figure 6.13. Velocity fields at failure.

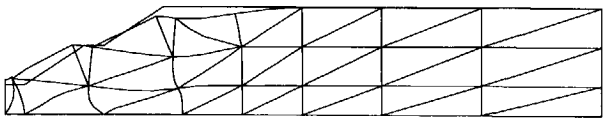

(a) non-reinforced embankment, small deformation analysis

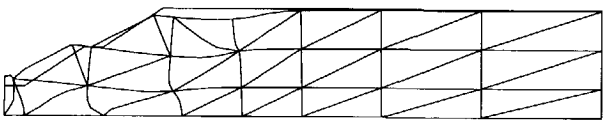

(b) non-reinforced embankment, large deformation analysis

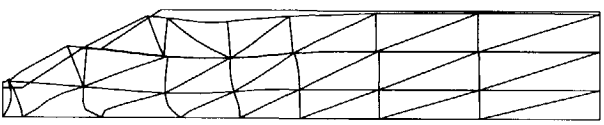

(c) reinforced embankment, small deformation analysis

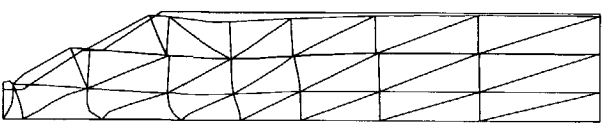

(d) reinforced embankment, large deformation analysis

Figure 6.14. Deformed meshes at failure.

at both sides of the textile. This difference is balanced by the curved membrane.

The shear stresses of Figure (6.15) clearly show the effect of the reinforcement. At the bottom of the textile, the shear stresses swiftly change their sign when crossing the curved slip surface. To the left of this surface the subsoil squeezes along the textile towards the ditch, whereas to the right the subsoil serves as a tie, holding back the textile. The shear stresses above the the textile show that the embankment on top is pushed in the direction of the ditch. At the interface between the fill and the textile virtually no shear stresses develop, indicating that the fill travels along on top of the textile.

The textile forces, Figure (6.16), are in agreement with the shear stress distribution: at both ends the forces vanish, whereas they attain their maximum value at the position of the curved slip plane. The maximum values of 75 and 80 kN/m are in the same order of magnitude as the measured maximum value of 90 kN/m.

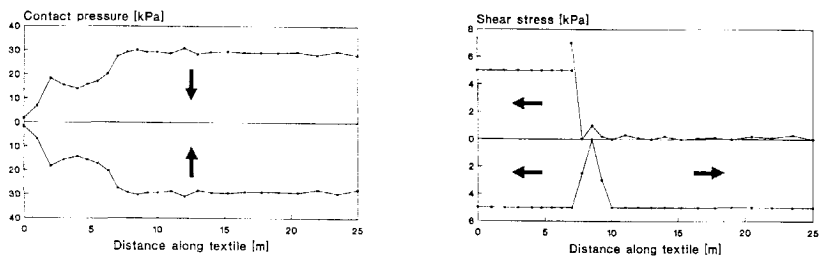

(a), (b) small deformation analysis

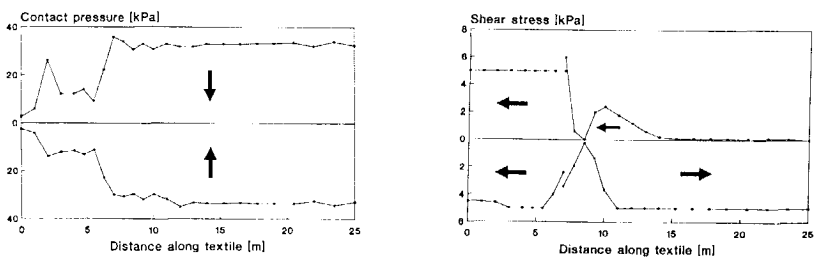

(c), (d) large deformation analysis

Figure 6.15. Stress distribution along geotextile.

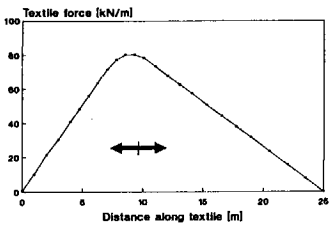

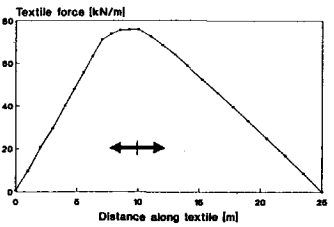

(a) small deformation analysis. (b) large deformation analysis.

Figure 6.16. Textile force at failure.

APPENDIX C

For plane strain conditions, equations (6.17) and (6.23) yield

$$\underline{\underline{K}}_{m2} + \underline{\underline{K}}_{m3} = \int_{\xi} n_{\xi} \, J^{-2} \, \underline{\underline{N}}^{T}_{,\xi} \, \underline{\underline{R}} \, \underline{\underline{N}}_{,\xi} \, J \, d\xi \tag{C1}$$

where

$$\underline{\underline{R}} = \begin{bmatrix} \left\{1 - J^{-2} \left(\frac{\partial x}{\partial \xi}\right)^2\right\} & \left\{-J^{-2} \frac{\partial x}{\partial \xi} \frac{\partial y}{\partial \xi}\right\} \\ \left\{-J^{-2} \frac{\partial x}{\partial \xi} \frac{\partial y}{\partial \xi}\right\} & \left\{1 - J^{-2} \left(\frac{\partial y}{\partial \xi}\right)^2\right\} \end{bmatrix} \tag{C2}$$

To arrive at this expression, definition (6.10) has been substituted. For an element which remains straight during deformation we may write

$$\underline{\underline{N}}_{,\xi} = \frac{1}{2} \begin{bmatrix} -1 & 0 & 1 & 0 \\ 0 & -1 & 0 & 1 \end{bmatrix} \tag{C3}$$

$$J^{-1} \frac{\partial x}{\partial \xi} = \cos\alpha$$

$$J^{-1} \frac{\partial y}{\partial \xi} = \sin\alpha \tag{C4}$$

where α is the angle enclosed by the x-axis and the element. For this special case, integration of equation (C1) yields

$$\underline{\underline{K}}_{m2} + \underline{\underline{K}}_{m3} = \frac{n_\xi}{l} \begin{bmatrix} \sin\alpha\sin\alpha & -\sin\alpha\cos\alpha & -\sin\alpha\sin\alpha & \sin\alpha\cos\alpha \\ -\sin\alpha\cos\alpha & \cos\alpha\cos\alpha & \sin\alpha\cos\alpha & -\cos\alpha\cos\alpha \\ -\sin\alpha\sin\alpha & \sin\alpha\cos\alpha & \sin\alpha\sin\alpha & -\sin\alpha\cos\alpha \\ \sin\alpha\cos\alpha & -\cos\alpha\cos\alpha & -\sin\alpha\cos\alpha & \cos\alpha\cos\alpha \end{bmatrix} \qquad (C5)$$

where l is the element length.

REFERENCES

1. W. Prager, *Introduction to Mechanics of Continua*, Dover Publications, New York, 1973.
2. A.J.M. Spencer, *Continuum Mechanics*, Longman, London, 1980.
3. R. Hill, *The Mathematical Theory of Plasticity*, Clarendon Press, Oxford, 1950.
4. B.A. Finlayson, *The Method of Weighted Residuals and Variational Principles*, Academic Press, 1972.
5. W.T. Koiter, 'General theorems for elastic-plastic solids', in I.N. Sneddon and R. Hill (eds.), *Progress in Solid Mechanics, Vol.1*, North-Holland, Amsterdam, 1960, pp. 165-221.
6. Y.C. Fung, *Foundations of Solid Mechanics*, Prentice-Hall, New Jersey, 1965.
7. J. van der Lugt, 'A finite element method for the simulation of thermo-mechanical contact problems in forming processes', *Dissertation*, Twente University of Technology, the Netherlands, 1988.
8. M. Boulon, 'Contribution a la mechanique des interfaces sols-structures', *Memoire d'Habilitation*, l'Universite Joseph Fourier de Grenoble, France, 1988.
9. F. Breinlinger, 'Bodenmechanische Stoffgleichungen bei grossen Deformationen sowie Be- und Endlastungsvorgängen', *Mitteilung 30*, Institut für Geotechnik Stuttgart, Germany, 1989.
10. R.M. McMeeking and J.R. Rice, 'Finite-element formulations for problems of large elastic-plastic deformation', *Int. J. Solids Struct.*, **11**, 601-616 (1975).
11. J. Huetink, 'On the simulation of thermo-mechanical forming processes', *Dissertation*, Twente University of Technology, the Netherlands, 1986.
12. J. Mandel, 'Généralisation de la théorie de W.T. Koiter', *Int. J. Solids Struct.*, 1, 273-295 (1965).
13. O.C. Zienkiewicz, *The Finite Element Method*, 3rd edn., McGraw-Hill, London, 1977.
14. K.J. Bathe, *Finite Element Procedures in Engineering Analysis*, Prentice-Hall, New Jersey, 1982.
15. I.M. Smith and D.V. Griffiths, *Programming the Finite Element Method, 2nd edn.*, J. Wiley and Son, New York, 1988.
16. D.R.J. Owen and E. Hinton, *Finite Elements in Plasticity*, Pineridge Press, Swansea, 1980.
17. P.G. Bergan, G. Horrigmoe, B. Kråkeland and T.H. Søreide, 'Solution techniques for non-linear finite element problems', *Int. J. Numer. Methods Eng.*, 12, 1677-1696 (1978).
18. R. Kolar and H.A. Kamel, 'On some efficient solution algorithms for nonlinear finite element analysis', in Bergan et al. (eds.), *Proc. Europe-U.S. Symposium on Finite Element Methods for Nonlinear Problems*, Springer-Verlag, Berlin Heidelberg, 1986, pp. 425-445.
19. W.C. Rheinboldt and E. Riks, 'Solution techniques for non-linear finite element equations', Chapter 7 in A.K. Noor and W.D. Pilkey (eds.), *State-of-the-Art Surveys on Finite Element Techniques*, ASME, New York, 1986.
20. P. Humbert and P. Mestat, 'Improved algorithm for non-linear analysis by the finite element method', in G. Swoboda (ed.), *Proc. 6th Int. Conf. on*

Numerical Methods in Geomechanics, Vol.1, Balkema, Rotterdam, 1988, pp. 195-204.
21. M.A. Crisfield, 'Some recent research on numerical techniques for structural analysis', in J. Middleton and G.N. Pande (eds.), *Numerical Methods in Engineering: Theory and Applications, Vol.2*, Balkema, Rotterdam, 1985, pp. 565-575.
22. R. de Borst, 'Non-linear analysis of frictional materials', *Dissertation*, Delft University of Technology, the Netherlands, 1986.
23. M.A. Crisfield, 'A fast incremental/iterative solution procedure that handles snap-through', *Comp. Struct.*, **13**, 55-62 (1981).
24. K.J. Bathe and E.N. Dvorkin, 'On the automatic solution of nonlinear finite element equations', *Comp. Struct.*, **17**, 871-879 (1983).
25. J.H. Wilkinson, *The Algebraic Eigenvalue Problem*, Clarendon Press, Oxford, 1965.
26. P.A. Vermeer and H. van Langen, 'Soil collapse computations with finite elements', *Ing.- Archiv*, **59**, 221-236 (1989).
27. W.F. Schmidt, 'Adaptive step size selection for use with the continuation method', *Int. J. Numer. Methods Eng.*, **12**, 677-694 (1978).
28. P.G. Bergan and R.W. Clough, 'Convergence criteria for iterative processes', *AIAA J.*, **10**, 1107-1108 (1972).
29. H. van Langen and P.A. Vermeer, 'Automatic step size correction for non-associated plasticity problems', *Int. J. Numer. Methods. Eng.*, **29**, 579-598 (1990).
30. P.A. Vermeer and R. de Borst, 'Non-associated plasticity for soils, concrete and rock', *Heron*, **29**, No. 3 (1984).
31. R. de Borst and P.A. Vermeer, 'Possibilities and limitations of finite elements for limit analysis', *Geotechnique*, **34**, 199-210 (1984).
32. S.W. Sloan and W.F. Randolph, 'Numerical prediction of collapse loads using finite element methods', *Int. J. Numer. Anal. Methods Geomech.*, **6**, 47-76 (1982).
33. E.H. Davis and J.R. Booker, 'The effect of increasing strength with depth on the bearing capacity of clays', *Geotechnique*, **23**, 551-563 (1973).
34. K. Terzaghi, *Theoretical Soil Mechanics*, Wiley, New York, 1940.
35. P. Gussmann, 'KEM in geomechanics', in G. Swoboda (ed.), *Proc. 6th Int. Conf. on Numerical Methods in Geomechanics, Vol.2*, Balkema, Rotterdam, 1988, pp. 823-828.
36. V.V. Sokolovskii, *Statics of Granular Media*, Pergamon, Oxford, 1965.
37. D.C. Drucker, 'A definition of stable inelastic material', *Trans. ASME J. Appl. Mech.*, **29**, 101-106 (1958).
38. R.E. Goodman, R.L. Taylor and T.L. Brekke, 'A model for the mechanics of jointed rock', *J. of the Soil Mech. Found. Div. ASCE*, **94**, SM3, 637-659 (1968).
39. R.E. Goodman and J. Dubois, 'Duplication of dilatancy in analysis of jointed rocks', *J. of the Soil Mech. Found. Div. ASCE*, **98**, SM4, 399-422 (1972).
40. O.C. Zienkiewicz, B. Best, C. Dullage and K.C. Stagg, 'Analysis of non-linear problems in rock mechanics with particular reference to jointed rock systems', in *Proc. 2nd Cong. Int. Soc. Rock Mech., Vol. 3*, Beograd, 1970, pp. 501-509.
41. J. Ghaboussi, E.L. Wilson and J. Isenberg, 'Finite element for rock joints and interfaces', *J. of the Soil Mech. Found. Div. ASCE*, **99**, SM10, 833-848 (1973).
42. P. Nath, 'The analysis of composite structures with prescribed frictional

conditions at the interfaces', *Int. J. Numer. Anal. Methods Geomech.*, **1**, 387-396 (1977).
43. N. Okamoto and M. Nakazawa, 'Finite element incremental contact analysis with various frictional conditions', *Int. J. Numer. Methods Eng.*, **14**, 337-357 (1979).
44. M. Boulon and P. Foray, 'Physical and numerical simulation of lateral shaft friction along offshore piles in sand', in *Proc. 3rd Int. Conf. Num. Meth. Offshore Piling*, Nantes, 1986, pp. 127-147.
45. N. Chandrasekaran, W.E. Haisler and R.E. Goforth, 'A finite element solution method for contact problems with friction', *Int. J. Numer. Methods Eng.*, **24**, 477-495 (1987)
46. P.R. Heyliger and J.N. Reddy, 'A mixed computational algorithm for plane elastic contact problems - I. formulation', *Comp. Struct.*, **26**, 621-634 (1987).
47. M.G. Katona, 'A simple contact-friction interface element with application to buried culverts', *Int. J. Numer. Anal. Methods Geomech.*, **7**, 371-384 (1983).
48. G.N. Pande and K.G. Sharma, 'On joint / interface elements and associated problems of numerical ill-conditioning', *Int. J. Numer. Anal. Methods Geomech.*, **3**, 293-300 (1979).
49. F.E. Heuzé and T.G. Barbour, 'New models for rock joints and interfaces', *J. Geot. Eng. Div. ASCE*, **108**, GT5, 757-776 (1982).
50. C.S. Desai, M.M. Zaman, J.G. Lighter and H.J. Siriwardana, 'Thin-layer element for interfaces and joints', *Int. J. Numer. Anal. Methods Geomech.*, **8**, 19-43 (1984).
51. C.S. Desai and S. Sargand, 'Hybrid FE procedure for soil-structure interaction', *J. Geot. Eng. Div. ASCE*, **110**, 473-486 (1984).
52. A. Gens, I. Carol and E.E. Alonso, 'An interface element formulation for the analysis of soil reinforcement interaction', *Computers and Geotechnics*, **7**, 133-151 (1988).
53. D. Ngo and A.C. Scordelis, 'Finite element analysis of reinforced concrete beams', *J. Am. Concrete Inst.*, **64**, (14), 152-163 (1967).
54. J.G. Rots, 'Computational modeling of concrete fracture', *Dissertation*, Delft University of Technology, the Netherlands, 1988.
55. J. Hohberg, 'Trennflächenformulierungen für die statische und dynamische Berechnung von Bogenstaumauern', *Bericht Nr. 163*, Institut für Baustatik und Konstrukion ETH Zürich, 1988.
56. P.A. Vermeer, 'A modified initial strain method for plasticity problems', *Proc. 3rd Int. Conf. on Numerical Methods in Geomechanics*, Balkema, Rotterdam, 1979, pp. 377-387.
57. J.P. Giroud, *Tables pour le calcul des fondations, Vol. 1*, Dunod, Paris, 1972.
58. J. Hohberg, 'A note on spurious oscillations in FEM joint elements', *Earthq. Eng. Struct. Dyn.*, **19**, 773-779 (1990).
59. L. Prandtl, 'Über die Härte plastischer Körper', *Nachr. d. Ges. d. Wiss., math. phys. Kl.*, Göttingen, 74
60. N.C. Koutsabeloulis and D.V. Griffiths, 'Numerical modelling of the trap door problem', *Geotechnique*, **39**, No. 1, 77-89 (1989).
61. J. de Ruiter, 'The static cone penetration test State-of-the-art-report', in *Proc. ESOPT II, Vol. 2*, Amsterdam, 1982, pp. 389-405.
62. D.V. Griffiths, 'Elasto-plastic analyses of deep foundations in cohesive soil', *Int. J. Numer. Anal. Methods Geomech.*, **6**, 211-219 (1982).
63. S.M. Willson, 'Finite element analysis of piles and penetrometers',

Dissertation, University of Manchester, United Kingdom, 1985.
64. R.F. Craig, '*Soil Mechanics*', Van Nostrand Reinhold, New York, 1978.
65. G.T. Houlsby, C.P. Wroth and D.M. Wood, 'Predictions of the results of laboratory tests on a clay using a critical state model', in G. Gudehus, F. Darve and I. Vardoulakis (eds.), *Results of the International Workshop on Constitutive Relations for Soils*, Balkema, Rotterdam, 1984, pp. 99-121.
66. P.A. Vermeer, 'Formulation and analysis of sand deformation problems', *Dissertation*, Delft University of Technology, the Netherlands, 1980.
67. N.A. Schofield and C.P. Wroth, *Critical State Soil Mechanics*, McGraw-Hill, London, 1968.
68. J.B. Burland, 'Deformation of soft clay', *Dissertation*, University of Cambridge, United Kingdom, 1967.
69. R. Nova and D.M. Wood, 'A constitutive model for sand in triaxial compression', *Int. J. Numer. Anal. Methods Geomech.*, **3**, 255-278 (1979).
70. M. Kavvadas and M.M. Baligh, 'Non-linear consolidation analyses around pile shafts', *Proc. 3rd Int. Conf. Beh. Offshore Struct., Vol.2*, MIT Press, 1982, pp. 338-347.
71. H. Sekiguchi and H. Ohta, 'Induced anisotropy and time dependency in clays', *Proc. 9th Int. Conf. SFME, Spec. Session 9*, Tokyo, 1977, pp. 163-175.
72. P.A. Vermeer, 'A double hardening model for sands', *Geotechnique*, **28**, 413-433 (1978).
73. P.V. Lade, 'Double hardening constitutive model for soils, parameter determination and predictions for two sands', *Proc. Cleveland Workshop Constitutive Equations for Granular Non-Cohesive Soils*, 1989, pp. 367-382.
74. O.C. Zienkiewicz and N.J. Naylor, 'Finite element studies of soils and porous media', in J.T. Oden and E.R. de Arantes (eds.), *Lect. Finite Elements in Continuum Mechanics*, UAH Press, 1973, pp. 459-493.
75. F.L. DiMaggio and I.S. Sandler, 'Material model for granular soils', *J. Eng. Mech. Div. ASCE*, **97**, 935-950 (1971).
76. I.S. Sandler, F.L. DiMaggio and G.Y. Baladi, 'Generalized cap model for geologic materials', *J. Geotech. Eng. Div. ASCE*, **102**, 683-697 (1976).
77. S. Labanieh, 'Modélisations non-linéaires de la rhéologie des sables et applications', *These*, L'Institut National Polytechnique de Grenoble, France, 1984.
78. G.Y. Baladi and B. Rohani, 'An elastic-plastic constitutive model for saturated sand subjected to monotonic and/or cyclic loadings', in W. Wittke (ed.), *Proc. 3rd Int. Conf. on Numerical Methods in Geomechanics, Vol. 1*, Balkema, Rotterdam, 1979, pp. 389-404.
79. I.M. Smith, 'Two 'Class A' predictions of offshore foundation performance', in G. Swoboda (ed.), *Proc. 6th Int. Conf. on Numerical Methods in Geomechanics, Vol.1*, Balkema, Rotterdam, 1988, pp. 137-144.
80. C. Plytas, 'Contribution a l'étude expérimentale et numérique des interfaces sols granulaires - structures', *These*, L'Université Scientifique et Médicale de Grenoble, France, 1985.
81. J.F. Besseling, 'Finite element methods', in J.F. Besseling and A.M.A. van der Heijden (eds.), *Proc. of the Symp. dedicated to the 65th Birthday of W.T. Koiter*, Delft University Press, Delft, 1979, pp. 53-78.
82. E. Ramm, 'Non-linear finite element analysis in structural mechanics', in W. Wunderlich, E. Stein and K.J. Bathe (eds.), *Proc. of the Europe-U.S. Workshop*, Ruhr Universität Bochum, 1980.

83. S. Timoshenko, *Theory of Elastic Stability*, 2nd edn., McGraw-Hill, New York, 1961.
84. K. Mattiasson, 'Numerical results from large deflection beam and frame problems analysed by means of elliptic integrals', *Int. J. Numer. Methods Eng.*, **17**, 145-153 (1981).
85. R. Veldhuijzen van Zanten (ed.), *Geotextiles and Geomembranes in Civil Engineering*, Balkema, Rotterdam, 1986.
86. H.J. Burd, 'A large displacement finite element analysis of a reinforced unpaved road', *Dissertation*, University of Oxford, United Kingdom, 1986.
87. J.P. Giroud and L. Noiray, 'Geotextile-reinforced unpaved road design', *J. Geotech. Eng. Div. ASCE*, **107**, GT9, 1233-1254 (1981).
88. J.B. Sellmeijer, C.J. Kenter and C. van den Berg, 'Calculation method for a fabric reinforced road', in J.P. Giroud and S.M. Warner (eds.), *Proc. 2nd Int. Conf. on Geotextiles*, Las Vegas, USA, 1982, pp. 393-398.
89. J.B. Sellmeijer, 'Design of geotextile reinforced paved roads and parking areas', in G. den Hoedt (ed.), *Proc. 4th Int. Conf. on Geotextiles, Geomembranes and Related Products, Vol. 1*, Balkema, Rotterdam, 1990, pp. 177-182.
90. H.B. Poorooshasb, 'Analysis of geosynthetic reinforced soil using a simple transform function', *Computers and Geotechnics*, **8**, No.4, 289-309 (1989).
91. J.R. Greenwood, 'Inclusion of reinforcement forces in stability analysis', in G. den Hoedt (ed.), *Proc. 4th Int. Conf. on Geotextiles, Geomembranes and Related Products, Vol. 1*, Balkema, Rotterdam, 1990, page 114.
92. M.J. Hamilton-Huisman, 'Design guidelines for reinforced embankments on soft soil using Stabilenka reinforcing mats', *ABT-Consulting Engineering and Enka Industrial Systems*, Arnhem, the Netherlands, 1987.
93. W.R. Spillers, 'Geometric stiffness matrix for space frames', *Comp. Struct.*, **36**, No.1, 29-37 (1990).
94. J. Brakel, M. Coppens, A.C. Maagdenberg and P. Risseeuw, 'Stability of slopes constructed with polyester reinforcing fabric, test section at Almere - Holland', in J.P. Giroud and S.M. Warner (eds.), *Proc. 2nd Int. Conf. on Geotextiles*, Las Vegas, USA, 1982, pp. 727-732.

SAMENVATTING

Het doel van deze studie is de verbetering van een aantal eindige elementen procedures voor de analyse van grond-deformatie en -stabiliteit. In het byzonder komt hierbij de interactie van grond en constructies aan de orde. Aangezien deze studie zich voornamelijk beperkt tot statische interactie van stijve constructies en min of meer slappe grond, ligt de nadruk op de beschrijving van het grondgedrag. In dergelijke gevallen wordt het niet-lineaire gedrag van het systeem geheel bepaald door de deformatie van de grond. Een uitzondering hierop vormt de interactie van grond en geotextiel-wapening. Aangezien de vervorming van geotextiel een grote rol speelt in het gedrag van gewapende grond, zal bij de behandeling van dit onderwerp de nodige aandacht besteed worden aan het constructieëlement zelf.

De indeling van dit rapport is als volgt. Hoofdstuk 2 behandelt de vergelijkingen voor de beschrijving van grote elastoplastische deformaties. De interpretatie van een aantal objectieve spanningstensoren krijgt hierbij speciale aandacht. Daarnaast geeft dit hoofdstuk het kader waarbinnen de elastoplastische modellen van volgende hoofdstukken ontwikkeld moeten worden.

Hoofdstuk 3 behandelt de oplossing van niet-lineaire eindige elementen vergelijkingen. De keuze van geschikte stapgrootten in de incrementeel-iteratieve procedure vormt een probleem in het geval van berekeningen voor grond met hoge wrijving. Hierdoor vergen dergelijke berekeningen veel tijd en ervaring. Een automatische stapgrootte procedure brengt verandering in deze situatie. De methode wordt toegepast op een aantal gronddeformatie problemen. Hoofdstuk 3 geeft daarnaast een bespreking van foutmaten en convergentie-criteria. Hierbij wordt benadrukt dat traditionele criteria in sommige gevallen geen goede schatting van de fout geven.

Hoofdstuk 4 beschrijft de theorie en toepassing van speciale elementen voor de interactie van grond en constructies. Na de formulering van deze zogenaamde "interface" elementen volgt een bespreking van de numerieke integratie. De kwaliteit van de berekende contactspanningen blijkt in hoge mate af te hangen van het gebruikte integratietype. Hierna komt een speciale toepassing van interface elementen aan de orde, te weten de behandeling van singuliere punten in het deformatieveld. Deze punten blijken in de meeste interactieproblemen op te treden. Een aantal voorbeelden toont aan dat de juiste behandeling van deze

punten van groot belang is.

In hoofdstuk 5 komt het gedrag van grond in het stadium voor bezwijken aan de orde. Het Mohr-Coulomb model wordt uitgebreid voor de nauwkeurige beschrijving van het compressiegedrag van zand. Het op deze wijze verkregen materiaalmodel is van het "cap"-type. De behandeling van ribben in singuliere vloeioppervlakken vormt een belangrijk onderdeel van deze bespreking. De klassieke behandeling wordt vereenvoudigd door gebruik te maken van een symmetriebeschouwing. De simulatie van een plaatproef toont de kwaliteit van het model.

Ter afsluiting van deze studie behandelt hoofdstuk 6 grote deformatie effecten in de analyse van grondlichamen. De plaatproef van hoofdstuk 5 wordt opnieuw geanalyseerd om de invloed van grote deformaties te tonen. Hierna wordt een membraanelement geformuleerd voor gebruik in de analyse van gewapende grond. De toepassing van dergelijke elementen komt aan de orde in de berekening van een ophoging op slappe grond.